

AD-A173 729

FRACTURE LONGEVITY (FATIGUE) DYNAMICS AND  
AEROELASTICITY OF COMPOSITE STR. (U) MASSACHUSETTS INST  
OF TECH CAMBRIDGE TECHNOLOGY LAB FOR ADVAN.

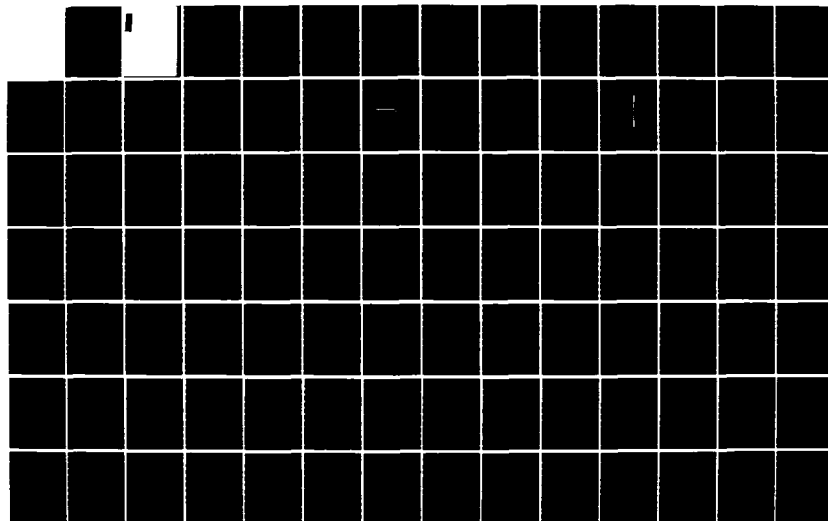
1/2

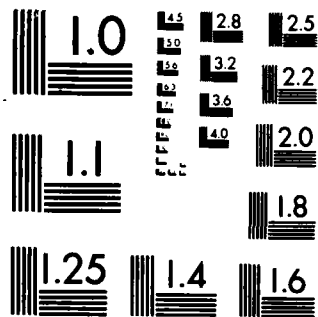
UNCLASSIFIED

P A LAGACE ET AL. 31 DEC 84 TELAC-84-21

F/G 11/4

NL





MICROCOPY RESOLUTION TEST CHART  
NATIONAL BUREAU OF STANDARDS-1963-A

AD-A173 729

## REPORT DOCUMENTATION PAGE

1a. REPORT SECURITY CLASSIFICATION <b>UNCLASSIFIED</b>			1b. RESTRICTIVE MARKINGS <b>ATB 129</b>														
2a. SECURITY CLASSIFICATION AUTHORITY			3. DISTRIBUTION/AVAILABILITY STATEMENT <b>Approved for public release; distribution unlimited.</b>														
2b. DECLASSIFICATION/DOWNGRADING SCHEDULE																	
4. PERFORMING ORGANIZATION REPORT NUMBER(S) <b>TELAC-84-21</b>			5. MONITORING ORGANIZATION REPORT NUMBER(S) <b>AFOSR-TR- 86 - 1008</b>														
6a. NAME OF PERFORMING ORGANIZATION <b>Tech. Lab. For Adv. Comp., Mass Inst. of Tech.</b>		6b. OFFICE SYMBOL (If applicable) <b>DA</b>		7a. NAME OF MONITORING ORGANIZATION <b>AFOSR/NA</b>													
6c. ADDRESS (City, State and ZIP Code) <b>MIT; ROOM 33-309 77 Massachusetts Avenue; Cambridge MA 02139</b>		7b. ADDRESS (City, State and ZIP Code) <b>BOLLING AFB, DC 20332-6448</b>															
8a. NAME OF FUNDING/SPONSORING ORGANIZATION <b>AFOSR</b>		8b. OFFICE SYMBOL (If applicable) <b>DA</b>		9. PROCUREMENT INSTRUMENT IDENTIFICATION NUMBER <b>F49620-83-K-0015</b>													
8c. ADDRESS (City, State and ZIP Code) <b>BOLLING AIR FORCE BASE WASHINGTON, D.C. 20332-6448</b>		10. SOURCE OF FUNDING NOS. <table border="1"><tr><th>PROGRAM ELEMENT NO.</th><th>PROJECT NO.</th><th>TASK NO.</th><th>WORK UNIT NO.</th></tr><tr><td>61102F</td><td>2307</td><td>B1</td><td></td></tr></table>				PROGRAM ELEMENT NO.	PROJECT NO.	TASK NO.	WORK UNIT NO.	61102F	2307	B1					
PROGRAM ELEMENT NO.	PROJECT NO.	TASK NO.	WORK UNIT NO.														
61102F	2307	B1															
11. TITLE (Include Security Classification) <b>FRACTURE, LONGEVITY (FATIGUE) DYNAMICS &amp; AEROELASTICITY OF COMPOSITE STRUCTURES</b>																	
12. PERSONAL AUTHOR(S) <b>Paul A. Lagace, James W. Mar, and John Dugundji</b>																	
13a. TYPE OF REPORT <b>FINAL REPORT</b>		13b. TIME COVERED <b>FROM 1/1/83 TO 3/14/84</b>		14. DATE OF REPORT (Yr., Mo., Day) <b>1984 Dec 31</b>													
				15. PAGE COUNT <b>140</b>													
16. SUPPLEMENTARY NOTATION																	
17. COSATI CODES <table border="1"><tr><th>FIELD</th><th>GROUP</th><th>SUB. GR.</th></tr><tr><td></td><td></td><td></td></tr><tr><td></td><td></td><td></td></tr><tr><td></td><td></td><td></td></tr></table>			FIELD	GROUP	SUB. GR.										18. SUBJECT TERMS (Continue on reverse if necessary and identify by block number) <b>PROGRESS JAN 83 - MAR 84</b>		
FIELD	GROUP	SUB. GR.															
19. ABSTRACT (Continue on reverse if necessary and identify by block number) <p>The results of several investigations into the fracture, longevity (fatigue dynamics, and aeroelasticity of composite materials are reported. The experimental work was conducted using Hercules graphite/epoxy prepreg in two forms: AS1/3501-6 unidirectional tape and A370-5H/3501-6 fabric. The topics discussed include unnotched tensile fracture, nonlinear stress-strain behavior, failure by delamination, sensitivity to notches under tensile loading, compressive failure, damage growth under cyclic load (both tensile and compressive), and the vibration and deflections of built-up graphite/epoxy wings.</p> <p>KEYWORDS: COMPOSITE, FAILURE, VIBRATION</p>																	
20. DISTRIBUTION/AVAILABILITY OF ABSTRACT <b>UNCLASSIFIED/UNLIMITED <input type="checkbox"/> SAME AS RPT. <input type="checkbox"/> OTIC USERS <input type="checkbox"/></b>			21. ABSTRACT SECURITY CLASSIFICATION <b>UNCLASSIFIED</b>														
22a. NAME OF RESPONSIBLE INDIVIDUAL <b>Dr. ANTHONY AMOS</b>		22b. TELEPHONE NUMBER (Include Area Code) <b>(202) 767-4937</b>		22c. OFFICE SYMBOL <b>AFOSR- NA</b>													

86 10 16 035

**FRACTURE, LONGEVITY (FATIGUE), DYNAMICS, AND  
AEROELASTICITY OF COMPOSITE STRUCTURES**

**Paul A. Lagace, James W. Mar, and John Dugundji**

**Technology Laboratory for Advanced Composites  
Massachusetts Institute of Technology  
77 Massachusetts Avenue  
Cambridge, Massachusetts 02139**

**DECEMBER 1984**

**Final Report for Period January 1983 - March 1984**

**Contract No. F49620-83-K-0015**

**DTIC  
ELECTE  
OCT 31 1986  
B**

## FOREWORD

This report describes work done at the Technology Laboratory for Advanced Composites (TELAC) at the Massachusetts Institute of Technology for the Air Force Office of Scientific Research under contract F49620-83-K-0015. Dr. Anthony K. Amos was the contract monitor.

The work reported herein was performed during the period from 1 January 1983 to 14 March 1984. The work represents the efforts of several graduate and undergraduate students under the direction of the faculty in the laboratory and is reported as such.



Approved	
Noted	
Reviewed	
Used	
Just	
<b>PER CALL JR</b>	
Dis	
<b>A-1</b>	

# TABLE OF CONTENTS

<u>Section</u>		<u>Page</u>
1	INTRODUCTION	1
2	FRACTURE	3
2.1	Manufacture and Testing of Standard Tensile Specimens	3
2.2	Fracture of Unnotched Tensile Coupons	10
2.3	Nonlinear Stress-Strain Behavior of Graphite/Epoxy Laminates	20
2.4	Comparison of Tapered and Straight-Edged Graphite/Epoxy Coupons	36
2.5	Effect of Thickness on Failure by Delamination	43
2.6	Fracture of Tensile Coupons with Holes	49
2.7	Fracture of Laminates with Two Sets of Angled Plies	58
2.8	Tensile Properties of Unnotched and Notched Graphite/Epoxy Fabric Composites	66
2.9	Instabilities and Failure of Graphite/Epoxy Tubes in Compressions	80
3	LONGEVITY (FATIGUE)	96
3.1	The Effect of Ply Thickness on Longitudinal Splitting and Delamination in Graphite/Epoxy under Compressive Cyclic Load	96
3.2	Splitting Damage in Multidirectional Laminates under Tension-Tension Cyclic Loading	120
4	DYNAMICS AND AEROELASTICITY	124
4.1	Vibrations and Deflections of Built-Up Graphite/Epoxy Wings	124
4.2	Miscellaneous	132
	REFERENCES	133
APPENDIX A	LIST OF REPORTS GENERATED UNDER CONTRACT	138
APPENDIX B	PERSONNEL	140

# NOMENCLATURE

a	damage length
A	parameter in damage growth equation
B	parameter in damage growth equation
d <sub>o</sub>	characteristic dimension in Whitney-Nuismer formulation
E <sub>L</sub>	longitudinal modulus
E <sub>T</sub>	transverse modulus
F <sub>C</sub> <sup>L</sup>	longitudinal compressive ultimate strength
F <sub>C</sub> <sup>T</sup>	transverse compressive ultimate strength
F <sub>t</sub> <sup>L</sup>	longitudinal tensile ultimate strength
F <sub>t</sub> <sup>T</sup>	transverse tensile ultimate strength
G <sub>LT</sub>	shear modulus
GPa	Giga (10 <sup>9</sup> ) pascal
H <sub>C</sub>	composite fracture parameter in Mar-Lin equation
Hg	mercury
Hz	Hertz
in	inch
K <sub>T</sub>	stress concentration factor
kg	kilograms
ksi	thousand pounds per square inch
m	1. parameter in Mar-Lin equation equal to singularity at bimaterial interface 2. meters
mm	millimeter
MPa	Mega (10 <sup>6</sup> ) pascal
N	1. cycles 2. Newtons
N <sub>o</sub>	cycle for damage initiation
Nm	Newton-meters

# NOMENCLATURE

P	applied load
r	notch half-length
rad	radians
w	1. width 2. displacement
da/dN	damage growth rate
$\epsilon$	strain
$\xi_1$	parameter in Whitney-Nuismer formulation
$\sigma$	stress
$\sigma_f$	fracture stress
$\sigma_o$	unnotched fracture stress
$\sigma_p$	notched fracture stress parameter in modified Whitney-Nuismer formulation
$\sigma_{zz}$	interlaminar normal stress
$\sigma_{xz}, \sigma_{1z}$	interlaminar shear stress
$\theta$	ply (lamination) angle
$\nu_{LT}$	major Poisson's ratio
$\nu_{LT}$	minor Poisson's ratio
$^{\circ}\text{C}$	degrees Celsius
$^{\circ}\text{F}$	degrees Fahrenheit
$^{\circ}$	degree
//	room temperature epoxy bondline

# LIST OF FIGURES

<u>Figure</u>		<u>Page</u>
Figure 1	TELAC manufacturing layup.	5
Figure 2	TELAC cure cycle for AS1/3501-6 graphite/epoxy.	6
Figure 3	Measurement locations for standard tensile specimen.	8
Figure 4	Physical characteristics of the standard TELAC tensile coupon specimen.	9
Figure 5	Experimental and predicted (via Tsai-Wu) unnotched fracture stresses versus lamination angle for the $[\theta]_s$ laminate family.	16
Figure 6	Experimental and predicted (via Tsai-Wu) unnotched fracture stresses versus lamination angle for the $[\pm\theta]_s$ laminate family.	17
Figure 7	Experimental and predicted (via Tsai-Wu) unnotched fracture stresses versus lamination angle for the $[\pm\theta/0]_s$ , $[0/\pm\theta]_s$ , and $[\pm\theta/0/-\theta]_s$ laminate families.	18
Figure 8	Five types of stress-strain behavior observed in graphite/epoxy laminates.	21
Figure 9	Generic nonlinear stress-strain curve illustrating break stress, fracture stress, and intermediate points.	24
Figure 10	Tangent modulus change from initial to final versus lamination angle for $[\pm\theta]_s$ specimens.	26
Figure 11	Typical stress-strain behavior of $[\pm\theta]_s$ laminates for $\theta$ equal to $15^\circ$ , $20^\circ$ , $25^\circ$ , and $30^\circ$ .	27
Figure 12	Break stress versus lamination angle for the $[\pm\theta]_s$ laminates.	28
Figure 13	Typical $[0]_s$ stress-strain behavior for load, unload, reload-to-failure cycle.	30
Figure 14	Typical $[\pm 30]_s$ stress-strain behavior for load, unload, reload-to-failure cycle.	31
Figure 15	Permanent strains after one load-unload cycle versus lamination angle for $[\pm\theta]_s$ laminates.	32
Figure 16	Physical characteristics of the "Boeing" tapered coupon specimen.	38
Figure 17	Typical stress-strain behavior for $[0/\pm 15]_s$ tapered specimen from Reference 1.	40

# LIST OF FIGURES

<u>Figure</u>		<u>Page</u>
Figure 18	Typical stress-strain behavior for $[0/\pm 15]_s$ tapered specimen from current work.	41
Figure 19	Concept of effective ply thickness.	45
Figure 20	Experimental fracture stresses and theoretical correlations for notched six-ply laminates with $\theta=15^\circ$ .	52
Figure 21	Experimental fracture stresses and theoretical correlations for notched six-ply laminates with $\theta=45^\circ$ .	53
Figure 22	Experimental fracture stresses and theoretical correlations for notched six-ply laminates with $\theta=90^\circ$ .	54
Figure 23	Experimentally-determined composite fracture parameter versus lamination angle for the six-ply laminates.	57
Figure 24	Experimental fracture stresses and theoretical correlation for notched $[\pm 15/\pm 30/0]_s$ and $[\pm 30/\pm 15/0]_s$ laminates.	64
Figure 25	Experimental fracture stresses and theoretical correlation for notched $[\pm 15/\pm 45/0]_s$ and $[\pm 45/\pm 15/0]_s$ laminates.	65
Figure 26	Five harness fabric construction.	67
Figure 27	Typical stress-strain behavior of $(0,90)_s$ and $(90,0)_s$ unnotched fabric laminates.	70
Figure 28	Typical stress-strain behavior of $(30,60)_s$ and $(60,30)_s$ unnotched fabric laminates.	71
Figure 29	Typical stress-strain behavior of $(45,-45)_s$ unnotched fabric laminates.	72
Figure 30	Experimental fracture stresses and theoretical correlation for notched $(0,90)_s$ and $(90,0)_s$ fabric laminates.	76
Figure 31	Experimental fracture stresses and theoretical correlation for notched $(30,60)_s$ and $(60,30)_s$ fabric laminates.	77
Figure 32	Experimental fracture stresses and theoretical correlation for notched $(45,-45)_s$ fabric laminates.	78

# LIST OF FIGURES

<u>Figure</u>		<u>Page</u>
Figure 33	Physical characteristics of the compressive specimen and measurement locations for inner and outer diameters, thicknesses, and length.	82
Figure 34	Cross-section of manufacturing layup for graphite/epoxy tubes.	83
Figure 35	Average compressive experimental and predicted modulus versus lamination angle for $[\pm\theta/0]_s$ and $[0/\pm\theta]_s$ tube specimens.	86
Figure 36	Experimental and predicted Poisson's ratio versus lamination angle for $[\pm\theta/0]_s$ and $[0/\pm\theta]_s$ tube specimens.	87
Figure 37	Experimental failure stresses and theoretical correlations (and feasible region) for $[\pm\theta/0]_s$ tube specimens.	88
Figure 38	Experimental failure stresses and theoretical correlations (and feasible region) for $[0/\pm\theta]_s$ tube specimens.	89
Figure 39	Physical characteristics of the sandwich specimen.	101
Figure 40	Definition of longitudinal delamination length.	105
Figure 41	Typical compressive stress-strain behavior of $[\pm 45_n/0_n]_s$ laminate with a 6.35 mm hole.	107
Figure 42	Typical plots of longitudinal delamination length versus logarithm of the number of applied load cycles.	111
Figure 43	Schematic model of the progression of damage via longitudinal delamination.	114
Figure 44	Physical characteristics of the special tensile coupon specimen with precut splits.	116
Figure 45	Experimental fracture stress versus notch size for the $[45_{24}]$ specimens with holes.	122
Figure 46	Characteristics of the wing box specimen.	125
Figure 47	Typical results of static wing deflection tests (for $[30_2]$ wing).	128
Figure 48	Photographs showing soap method to determine natural modes of graphite/epoxy built-up wings: (top) $[30_4]$ wing in mode 2, 2nd bending; (bottom) $[30_4]$ wing in mode 3, 1st torsion.	130

# LIST OF FIGURES

<u>Figure</u>		<u>Page</u>
Figure 49	Experimentally-determined node lines for third mode of $\{\theta_4\}$ wings.	131

# LIST OF TABLES

<u>Table</u>		<u>Page</u>
Table 1	Graphite/epoxy laminates tested in unnotched condition under tension (to date)	12
Table 2	Average tensile unnotched fracture stresses for graphite/epoxy laminates	14
Table 3	Basic properties of AS1/3501-6 unidirectional ply	15
Table 4	Experimental test program for nonlinear stress-strain behavior of $[\pm\theta]_s$ laminates	23
Table 5	Cycles to failure and permanent strains for $[\pm 35]_s$ graphite/epoxy specimens subjected to tension-tension cyclic loading	35
Table 6	Experimental results for straight-edged and tapered graphite/epoxy specimens of layups $[\pm 15/0]_s$ and $[0/\pm 15]_s$	42
Table 7	Testing program to determine effect of thickness on failure via delamination in graphite/epoxy	46
Table 8	Average experimental failure stresses and strains for effective ply thickness tests	48
Table 9	Test program to determine notch sensitivity of graphite/epoxy laminates with two sets of angled plies	60
Table 10	Average experimental fracture stresses for graphite/epoxy laminates with two sets of angled plies	61
Table 11	Test program to determine fracture behavior and notch sensitivity of graphite/epoxy fabric laminates	68
Table 12	Average experimental fracture stresses for notched graphite/epoxy fabric laminates	73
Table 13	Experimentally-determined composite fracture parameters for graphite/epoxy fabric laminates	75
Table 14	Test matrix for six-ply graphite/epoxy tube specimens in compression	85
Table 15	Experimental failure stresses and modes for $[\pm\theta/0]_s$ and $[0/\pm\theta]_s$ tubular specimens under compressive load	91
Table 16	Experimental test program for compression-compression cyclic loading of notched $[\pm 45_n/0_n]_s$ graphite/epoxy specimens	99

# LIST OF TABLES

<u>Table</u>		<u>Page</u>
Table 17	Results of compressive monotonic to failure tests of $[\pm 45_n/0_n]_s$ graphite/epoxy specimens	106
Table 18	Average results of linear regressions for longitudinal delamination growth parameters for $[\pm 45_n/0_n]_s$ graphite/epoxy specimens	112
Table 19	Average results of residual tensile strength tests for $[\pm 45_n/0_n]_s$ graphite/epoxy specimens	119
Table 20	Experimental and analytical natural frequencies for the $[\theta_2]$ and $[\theta_4]$ wing sets	129



## 1. INTRODUCTION

The Technology Laboratory for Advanced Composites (TELAC) of the Department of Aeronautics and Astronautics at M.I.T. has developed facilities in recent years, with significant support from the Air Force Office of Scientific Research (AFOSR), to examine the properties of composite materials and their structures. During the past year and two months covered by this report (January 1, 1983 to March 14, 1984), the students and faculty of TELAC have conducted research in a number of problem areas in a continuing effort to understand the fracture, longevity, dynamics and aeroelasticity of composite structures. Both graduate and undergraduate students have been involved in this work which involves the manufacture and testing of specimens in the facilities of the laboratory as well as the use of analytical tools in reviewing the experimental data and in developing design methodologies.

This work has been supported on a continuing basis by the Air Force Office of Scientific Research. The present report will describe work which has been concluded during the past contract period, work which has been conducted during this period, and work which was initiated during this period and is continuing under the continuation of AFOSR contract F49620-83-K-0015 during the current year. Several of the projects which have been completed are fully reported in student theses or other laboratory reports which are referenced here. A summary of these activities are presented herein. Interested

personnel may refer to the individual reports for a more thorough description. In addition, a list of all reports generated under this contract during the contract year are listed in Appendix A.

## 2. FRACTURE

The work in fracture at TELAC has been directed at finding methods by which the fracture stress of an arbitrary layup may be predicted for various loading conditions. As a step in the process, a great majority of work has looked at the behavior of the Hercules AS1/3501-6 graphite/epoxy material system. In the past, hundreds of specimens, both unnotched and notched, have been tested under static tension to observe fracture modes and stresses. Much of this work has been reported in the previous year's report [1].

This work continued during the past year to fill gaps in the experimental data which has been previously acquired on the Hercules AS1/3501-6 graphite/epoxy system and to explain deviations from predicted behavior. Work which began during the previous year examining the fracture behavior of a woven fabric graphite/epoxy prepreg (Hercules A370-5H/3501-6) was more aggressively pursued this past year. In addition, the work was expanded into the compressive regime. The results are reported herein.

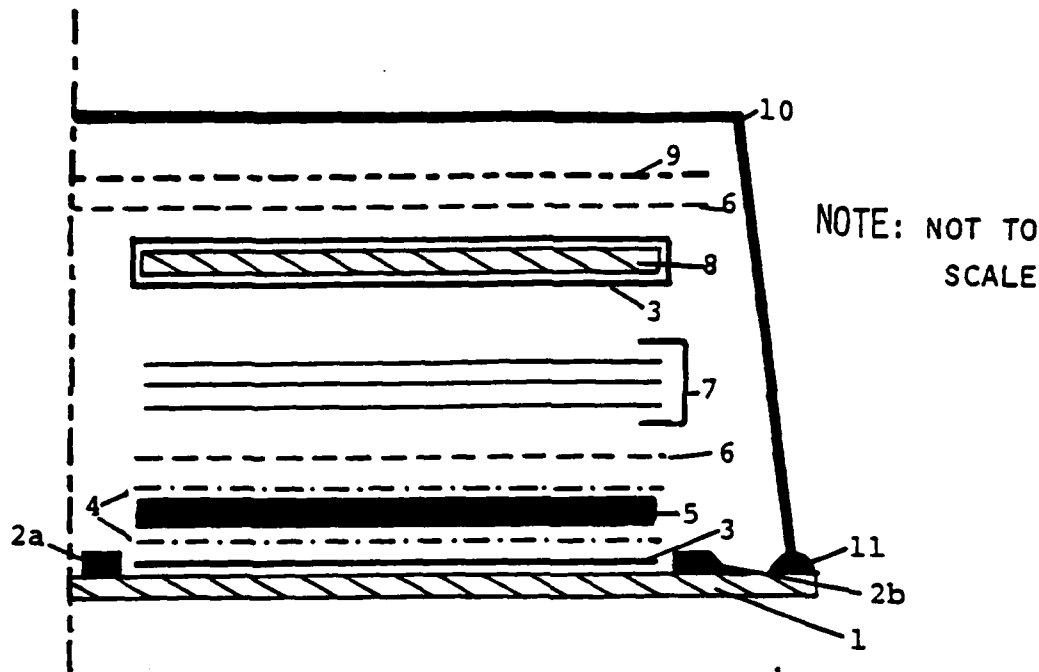
### 2.1 Manufacture and Testing of Standard Tensile Coupons

The specimen used in nearly all the investigations into the tensile fracture behavior at TELAC is a standard specimen developed in the laboratory several years ago. This specimen is very similar to the standard specimen recommended by the

American Society for Testing and Materials [2]. Since this specimen and the manufacture of it is common to most of these investigations, the manufacturing process is described here. Any variations for specific investigations are reported in the appropriate sections.

The prepreg systems were handled in the same manner except that the AS1/3501-6 graphite/epoxy tape was supplied in 300 mm wide rolls while the A370-5H/3501-6 fabric was supplied in one meter wide rolls. Both prepreg systems were stored in a freezer at temperatures below  $-18^{\circ}\text{C}$  before use. The prepreg was allowed to warm up in a sealed bag for one hour before opening to prevent moisture condensation from contaminating the prepreg. The prepreg was cut using Stanley knives and specially prepared teflon-coated templates to assure desired fiber angles in each ply. All cuts were made so that only matrix joints were allowed in a ply such that all fibers were continuous throughout the ply. The plies were laid up with the use of a jig to assure proper lamination angles from ply to ply.

The 300 mm by 350 mm standard plates were prepared for curing on a specially designed caul plate which allows six of these standard plates to be cured in one operation. The prepreg laminates were prepared in the typical manner with peel-ply, teflon release films, and bleeder and breather systems. The manufacturing layup is shown in Figure 1. Cure took place in an autoclave under 0.59 MPA pressure and a full vacuum of 760 mm Hg according to the standard cure cycle for the 3501-6 system with a one hour hold at  $116^{\circ}\text{C}$  and a two hour hold at  $177^{\circ}\text{C}$  under



1. Aluminum Caul. Plate, 3/8" thick MIC 6 aluminum with thin uniform coat of mold release 225 baked on
- 2a. Cork dam (Corprene), 1/8" x 1" with adhesive backing
- b. Aluminum dam, 1/4" x 1", screwed down
3. Guaranteed non-porous teflon, TCGF-EHV .003, premium
4. Peel-ply #3921
5. Prepreg layup (laminate)
6. Porous teflon, TCGF .001-P porous
7. Paper bleeder (1 bleeder/2 plies of prepreg)
8. Aluminum Caul Plate, 1/4" thick MIC 6 aluminum with thin uniform coat of mold release 225 baked on
9. Air breather, #7781 fiberglass with volan finish
10. HS-6262 nylon vacuum bagging, 2 mils thick
11. Vacuum tape

Figure 1 TELAC manufacturing layup.

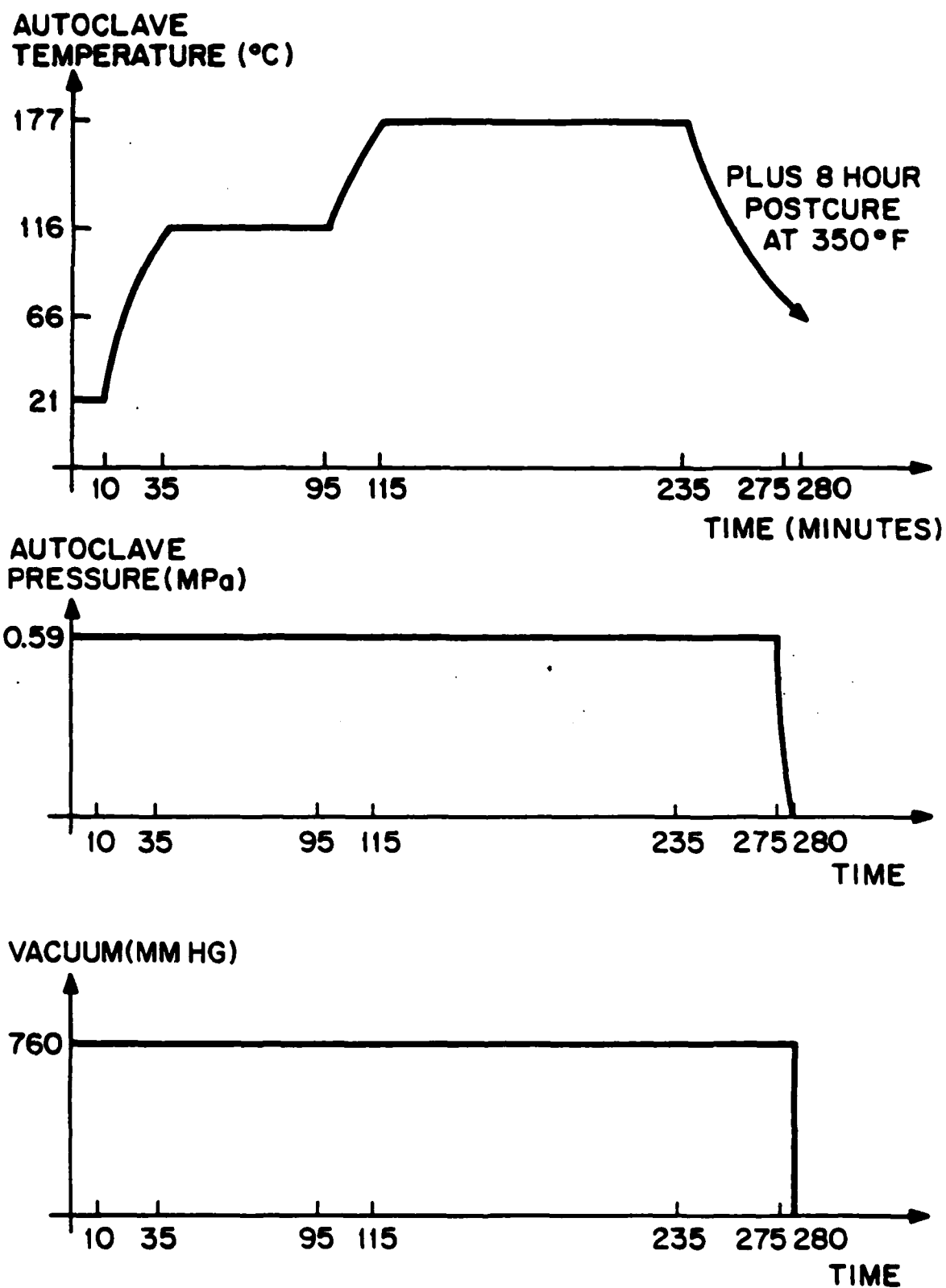


Figure 2 TELAC cure cycle for AS1/3501-6 graphite/epoxy.

these conditions. The cured plates were postcured in an oven at 177°C for eight hours. The complete cure cycle is shown in Figure 2.

The completed laminates were cut into 50 mm wide strips on a milling machine with a specially-designed table using a water-cooled diamond wheel. Thickness measurements were taken at nine locations and width measurements at three locations on each coupon as indicated in Figure 3. Many specimens were notched with holes. The holes were made by drilling with diamond-coated drill and reamer sets using a standard drill press and water for cooling. Use of the reamer bit after carefully drilling with the drill bit consistently resulted in smooth and round holes of a given size with no delaminations.

Glass/epoxy loading tabs of 0°/90° symmetric configurations were bonded onto each end of the graphite/epoxy specimens. The thickness of the tabs was dependent upon the thickness of the graphite/epoxy laminate with a ratio of 1.5 (tab thickness to specimen thickness) approximately maintained. The tabs were made from 3-M SP-1002 glass/epoxy cured following the standard cure cycle of two hours at 149°C at 0.35 MPa under full vacuum (760 mm Hg) in an autoclave. The tabs were cut to the proper dimensions of 50 mm by 75 mm on the milling machine with a diamond blade. One edge of each tab was beveled to a 30° angle on a belt sander. The tabs were bonded onto the graphite/epoxy using film adhesive FM-123-2 supplied by American Cyanamid. The cure cycle was 90 minutes at 107°C and 0.35 MPa.

This entire process resulted in the specimen depicted in

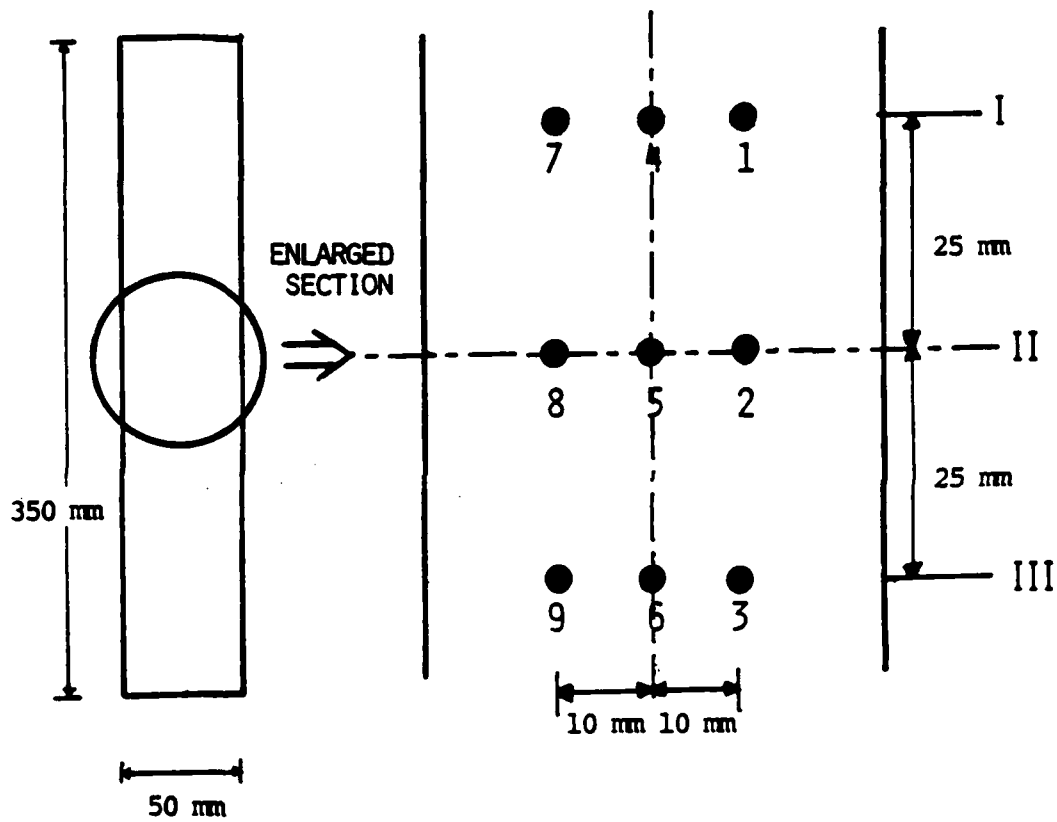


Figure 3 Measurement locations for standard tensile specimen.

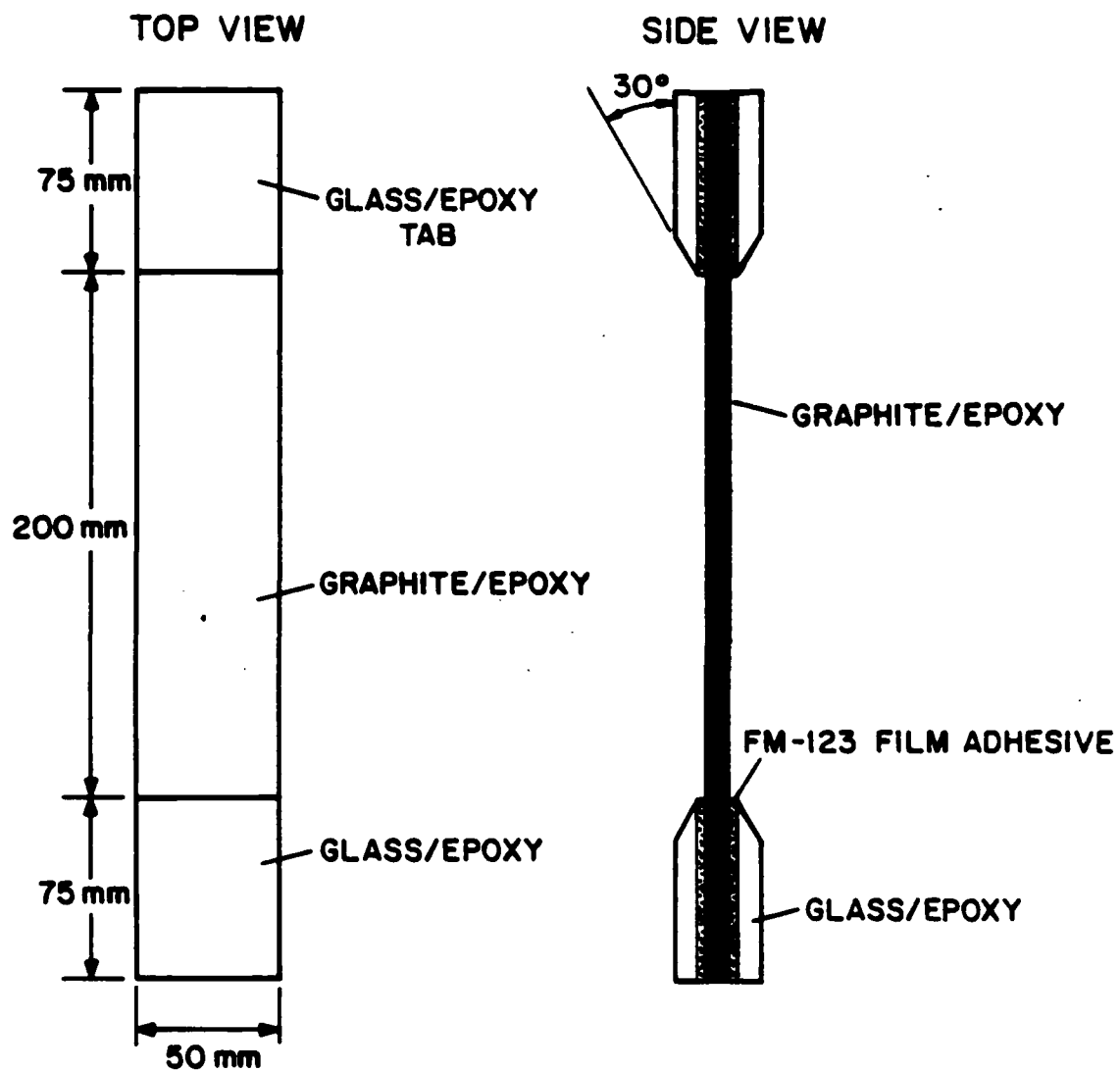


Figure 4 Physical characteristics of the standard TELAC tensile coupon specimen.

Figure 4. This manufacturing process is fully documented in the TELAC Manufacturing Notes [3].

In many cases, strain gages are bonded onto the specimen in the conventional way in order to obtain strain data for a variety of purposes. In general, strain gage type EA-09-125AD-120 manufactured by Micro Measurements was used.

Testing is accomplished on an MTS 810 Material Test System with the aid of hydraulic grips. In a standard test, specimens are loaded at a constant stroke rate of 1 mm/minute which yields an approximate strain rate of 5000 microstrain/minute over the 200 mm test section. Load and strain data are recorded automatically through an automated data acquisition system using a PDP-11/34 computer. Fracture loads are recorded after each test and a photograph is taken of each specimen after fracture. Generally, the specimens are monitored by ear throughout the test for any noises indicative of damage.

It is important to point out that the manufacturer's nominal per ply thickness of 0.134 mm (for the unidirectional prepreg, and 0.35 mm for the fabric) is used in the calculation of stresses rather than the actual measured laminate thickness. This allows the data to be reduced to a common base independent of slight manufacturing variations. In general, the measured thicknesses are very close to the nominal value.

## 2.2 Fracture of Unnotched Tensile Coupons

A considerable amount of work has been conducted at TELAC

examining the fracture modes and stresses of coupons loaded in uniaxial tension. This work has been conducted on laminates consisting of from four to eight plies and is summarized in the report for the last period [1]. This work has looked at the effects which lamination angle and stacking sequence have on the fracture characteristics of composites.

The overriding objective of this work is to establish the methodology by which the fracture stress of an arbitrary laminate can be predicted. It is therefore necessary to understand the phenomena involved. Five different laminate "families" (or stacking sequences) have been used:  $[\theta]_s$ ,  $[\pm\theta]_s$ ,  $[\pm\theta/0]_s$ ,  $[0/\pm\theta]_s$ , and  $[+\theta/0/-\theta]_s$ . A large number of laminates have been tested for various values of  $\theta$  as reported in the last report. The work conducted here was done to "fill in" the gaps so that data was obtained for  $5^\circ$  increments of  $\theta$  in the regions where the fracture behavior of the laminates tend to change with  $\theta$ . This occurs generally for  $\theta$  less than  $60^\circ$ . The laminates tested in the present work are:  $[0]_{12}$ ,  $[5]_8$ ,  $[25]_8$ ,  $[35]_8$ ,  $[\pm 25]_s$ ,  $[\pm 40]_s$ ,  $[\pm 50]_s$ ,  $[\pm 55]_s$ ,  $[\pm 40/0]_s$ ,  $[0/\pm 20]_s$ ,  $[0/\pm 25]_s$ ,  $[0/\pm 35]_s$ ,  $[0/\pm 40]_s$ ,  $[+5/0/-5]_s$ ,  $[+10/0/-10]_s$ ,  $[+20/0/-20]_s$ ,  $[+25/0/-25]_s$ ,  $[+35/0/-35]_s$ , and  $[+40/0/-40]_s$ . A summary of all the laminates of AS1/3501-6 which have been tested in the unnotched condition to date is given in Table 1 with the laminates tested during the past year denoted by an asterisk.

The results of these laminates followed the same basic trends as found for the laminates of similar stacking sequence and value of  $\theta$  for the previous work. The specifics of

Table 1 Graphite/epoxy laminates tested in unnotched condition under tension (to date)

Laminate Family	$[\theta_8]$	$[\pm\theta]_s$	$[\pm\theta/0]_s$	$[0/\pm\theta]_s$	$[\pm\theta/0/-\theta]_s$
	$[5_8]^*$	$[\pm 5]_s$	$[\pm 5/0]_s$	$[0/\pm 5]_s$	$[+5/0/-5]_s^*$
	$[10_8]$	$[\pm 10]_s$	$[\pm 10/0]_s$	$[0/\pm 10]_s$	$[+10/0/-10]_s^*$
	$[15_8]$	$[\pm 15]_s$	$[\pm 15/0]_s$	$[0/\pm 15]_s$	$[+15/0/-15]_s$
	$[20_8]$	$[\pm 20]_s$	$[\pm 20/0]_s$	$[0/\pm 20]_s^*$	$[+20/0/-20]_s^*$
	$[25_8]^*$	$[\pm 25]_s^*$	$[\pm 25/0]_s$	$[0/\pm 25]_s^*$	$[+25/0/-25]_s^*$
	$[30_8]$	$[\pm 30]_s$	$[\pm 30/0]_s$	$[0/\pm 30]_s$	$[+30/0/-30]_s$
	$[35_8]^*$	$[\pm 35]_s$	$[\pm 35/0]_s$	$[0/\pm 35]_s^*$	$[+35/0/-35]_s^*$
	$[40_8]$	$[\pm 40]_s^*$	$[\pm 40/0]_s^*$	$[0/\pm 40]_s^*$	$[+40/0/-40]_s^*$
	$[45_8]$	$[\pm 45]_s$	$[\pm 45/0]_s$	$[0/\pm 45]_s$	$[+45/0/-45]_s$
	$[60_8]$	$[\pm 60]_s$	$[\pm 60/0]_s$	$[0/\pm 60]_s$	$[+60/0/-60]_s$
	$[75_8]$	$[\pm 75]_s$	$[\pm 75/0]_s$	$[0/\pm 75]_s$	$[+75/0/-75]_s$
	$[90_8]$	$[90_4]$	$[90_2/0]_s$	$[0/90_2]_s$	$[90/0/90]_s$
		Plus			
		$[\pm 50]_s^*$			
		$[\pm 55]_s^*$			

(5 specimens of each laminate)

\*indicates laminates tested under current work

stress-strain behavior are thus not reported here but can be found in Reference 4. Let it suffice to say that the measured longitudinal moduli were predicted using Classical Laminated Plate Theory and the basic properties of the unidirectional ply given in Table 3.

The trends in fracture mode and fracture stresses were also considered with that reported last year. The complete table of fracture stresses for unnotched specimens of these five laminate families is given in Table 2. Again, the new values are denoted by an asterisk. Plots of these experimental fracture stresses versus lamination angle  $\theta$  are presented in Figure 5 for the  $[\theta_g]$  laminate family; in Figure 6 for the  $[\pm\theta]_s$  laminate family; and in Figure 7 for the three six-ply laminate families:  $[\pm\theta/0]_s$ ,  $[0/\pm\theta]_s$ , and  $[+\theta/0/-\theta]_s$ . In addition, the stress quadratic interaction criterion proposed by Tsai and Wu [5] is used in an attempt to correlate the data. The stresses predicted using this method with the basic values of the AS1/3501-6 ply shown in Table 3 are also plotted in these three figures. These stresses represent first-ply-failure.

As discussed in Reference 1, this criterion predicts the fracture stress extremely well for the unidirectional off-axis specimens, i.e.  $[\theta_g]$ . However, when the laminates are now angled plies,  $[\pm\theta]_s$ , the criterion predicts a much higher fracture stress than actually observed for values of  $\theta$  less than  $30^\circ$ . For values of  $\theta$  greater than  $30^\circ$ , the experimental points again fall on the predicted curve. This is a similar phenomenon to that which can be seen in Figure 7 for the three symmetric

Table 2 Average tensile unnotched fracture stresses for graphite/epoxy laminates

(All Values in MPa)

Lamination Angle = $\theta$	Laminate			
	$[\theta_g]$	$[\theta]_s$	$[\theta/0]_s$	$[0/\theta]_s$
5°	968 (9.6%)	1205 (4.3%)	1197 (9.8%)	1405 (5.0%)
10°	462 (2.5%)	1012 (7.1%)	1052 (4.5%)	1200 (3.5%)
15°	267 (15.2%)	889 (6.9%)	998 (7.3%)	1083 (6.1%)
20°	213 (19.2%)	723 (7.4%)	1064 (1.1%)	1080 (3.0%)
25°	167 (17.2%)	608 (6.1%)	1062 (3.9%)	1001 (5.7%)
30°	136 (13.8%)	527 (1.1%)	855 (5.1%)	945 (6.2%)
35°	125 (8.2%)	421 (2.5%)	835 (5.3%)	826 (2.2%)
40°	115 (11.7%)	284 (14.8%)	709 (9.4%)	760 (1.0%)
45°	96.5 (7.7%)	148 (9.3%)	732 (7.0%)	787 (3.2%)
60°	69.4 (5.7%)	74.6 (2.9%)	698 (3.9%)	814 (4.3%)
75°	54.3 (6.8%)	38.0 (8.4%)	672 (4.1%)	733 (4.8%)
90°	49.4 (18.0%)	53.9 (4.6%)	679 (8.9%)	732 (5.5%)
50°		104 (2.1%)	Mean (Coefficient of Variation)	
55°		91.0 (3.9%)		

\*indicates data obtained under current work

Table 3 Basic properties of AS1/3501-6 unidirectional ply

Elastic Constants		Ultimate Stresses	
$E_L$	130 GPa	$\sigma_{11}^t$	1661 MPa
$E_T$	10.5 GPa	$\sigma_{11}^c$	1698 MPa
$\nu_{LT}$	.28	$\sigma_{22}^t$	53.9 MPa
$G_{LT}$	6.0 GPa	$\sigma_{22}^c$	221 MPa
		$\sigma_{12}$	105 MPa

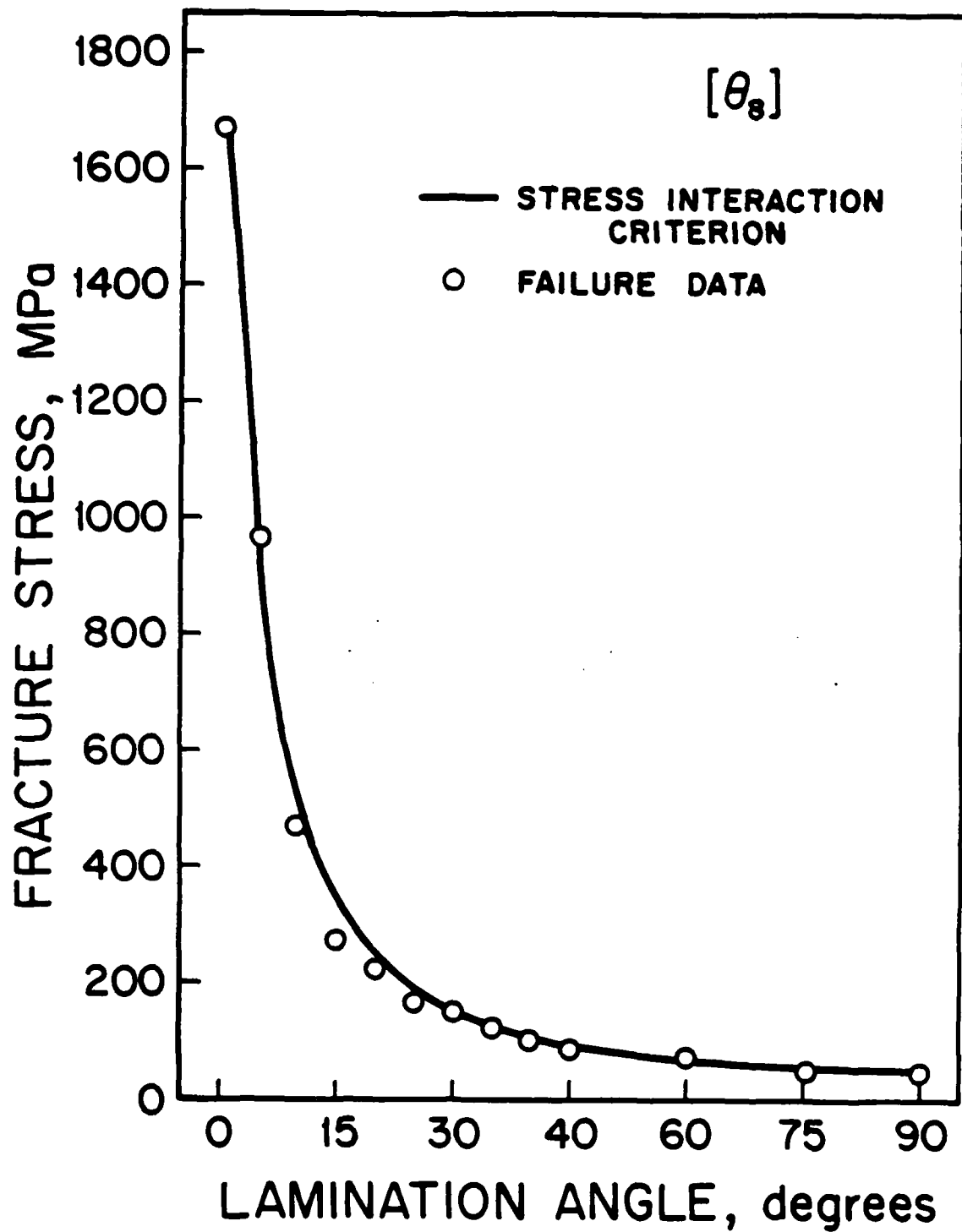


Figure 5 Experimental and predicted (via Tsai-Wu) unnotched fracture stresses versus lamination angle for the  $[\theta_8]$  laminate family.

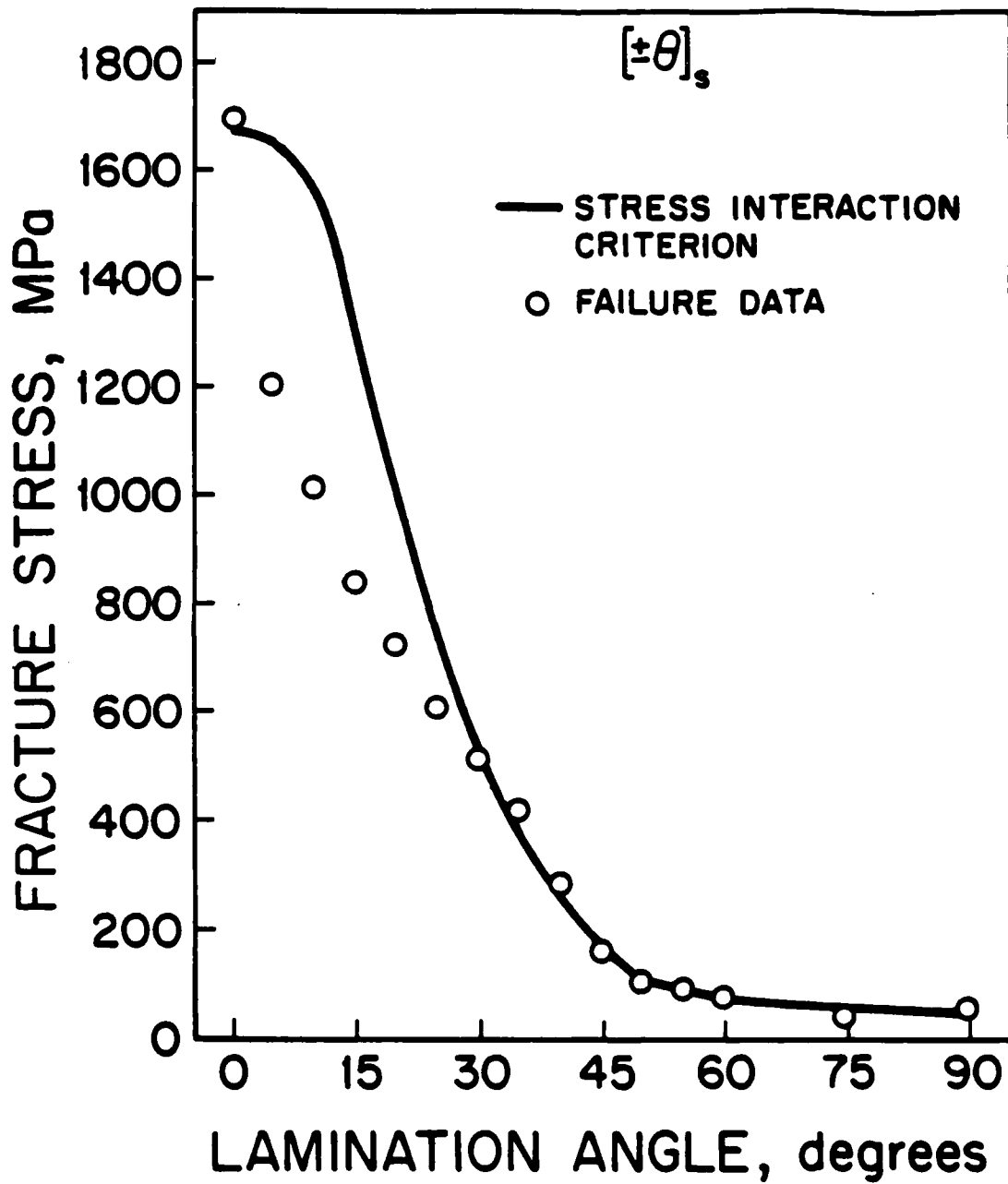


Figure 6

Experimental and predicted (via Tsai-Wu) unnotched fracture stresses versus lamination angle for the  $[\pm\theta]_s$  laminate family.

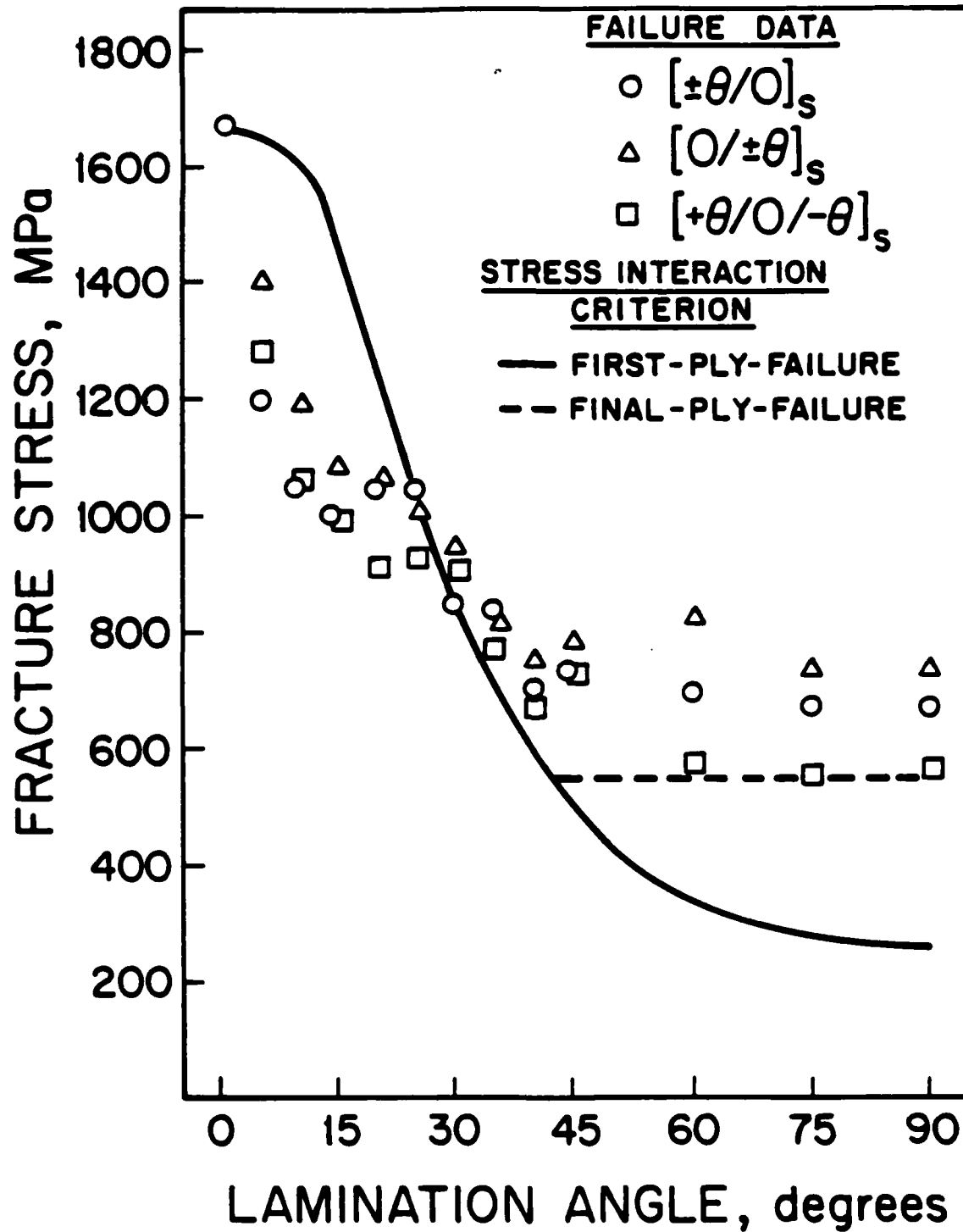


Figure 7

Experimental and predicted (via Tsai-Wu) unnotched fracture stresses versus lamination angle for the  $[\pm\theta/O]_s$ ,  $[O/\pm\theta]_s$ , and  $[+\theta/O/-\theta]_s$  laminate families.

stacking sequences of the six-ply laminates. For values of the lamination angle  $\theta$  less than  $30^\circ$ , the experimental fracture stresses fall well below the value predicted by the stress interaction criterion.

In the last report, it was postulated that this was the result of failure being prompted by delamination rather than by an in-plane mechanism. In fact, the failure modes of these specimens indicate that delamination does occur, especially in the  $[\pm\theta/0]_s$  and  $[+\theta/0/-\theta]_s$  stacking configurations. This phenomenon is being further investigated for these particular laminates by looking at the effects of ply and laminate thickness on the fracture stress and mechanism. This work is reported in section 2.5.

For the cases where  $\theta$  is greater than  $45^\circ$  for the three six-ply stacking arrangements, the final fracture stress is higher than the predicted first-ply-failure stress. This is due to the fact that the laminates possess significant post-first-ply-failure strength. A minimum estimate of the ultimate strength of these laminates can be obtained by "removing" the failed plies in the analysis, these are the plies at  $+\theta$  and  $-\theta$  (assuming symmetric failure), and recalculating the strength based on the remaining intact plies, in this case the two  $0^\circ$  plies. This is done and indicated by the straight dashed line in Figure 7. The experimental fracture stresses lie on or above this point. There is still a stacking sequence dependence since there continue to be three-dimensional effects both from three-dimensional load transfer around damage in "failed" plies

as well as delamination issues. The stress-strain curves obtained in these experiments verify this explanation since the stress-strain curve becomes erratic after an initial linear portion. The end of this initial linear portion approximately coincides with the predicted first-ply-failure stress. The erratic stress-strain behavior after this point is due to progressive failure in the laminate.

This work, that is filling in the unnotched fracture data, is discussed in depth by Chisholm and Chin in Reference 4.

### 2.3 Nonlinear Stress-Strain Behavior of Graphite/Epoxy Laminates

Composite laminates exhibit nonlinear stress-strain behavior when loaded under certain conditions. Previous investigations at TELAC have shown that these nonlinearities do occur in graphite/epoxy laminates under uniaxial tensile load (e.g.[6]). The basic stress-strain behavior of composite laminates can be separated into 5 major types as shown in Figure 8 [6]. The previous work at TELAC, as reported in last year's report [1], concentrated on the first three of these types. The latter two stress-strain behavior types, kneepoint and discontinuity point, deal with progressive failure of the laminate via transverse cracking. However, the three stress-strain types of stiffening, linear, and softening, deal with the basic material behavior (pre-damage). Experiments were done on  $[\pm\theta]_s$  graphite/epoxy laminates to investigate these

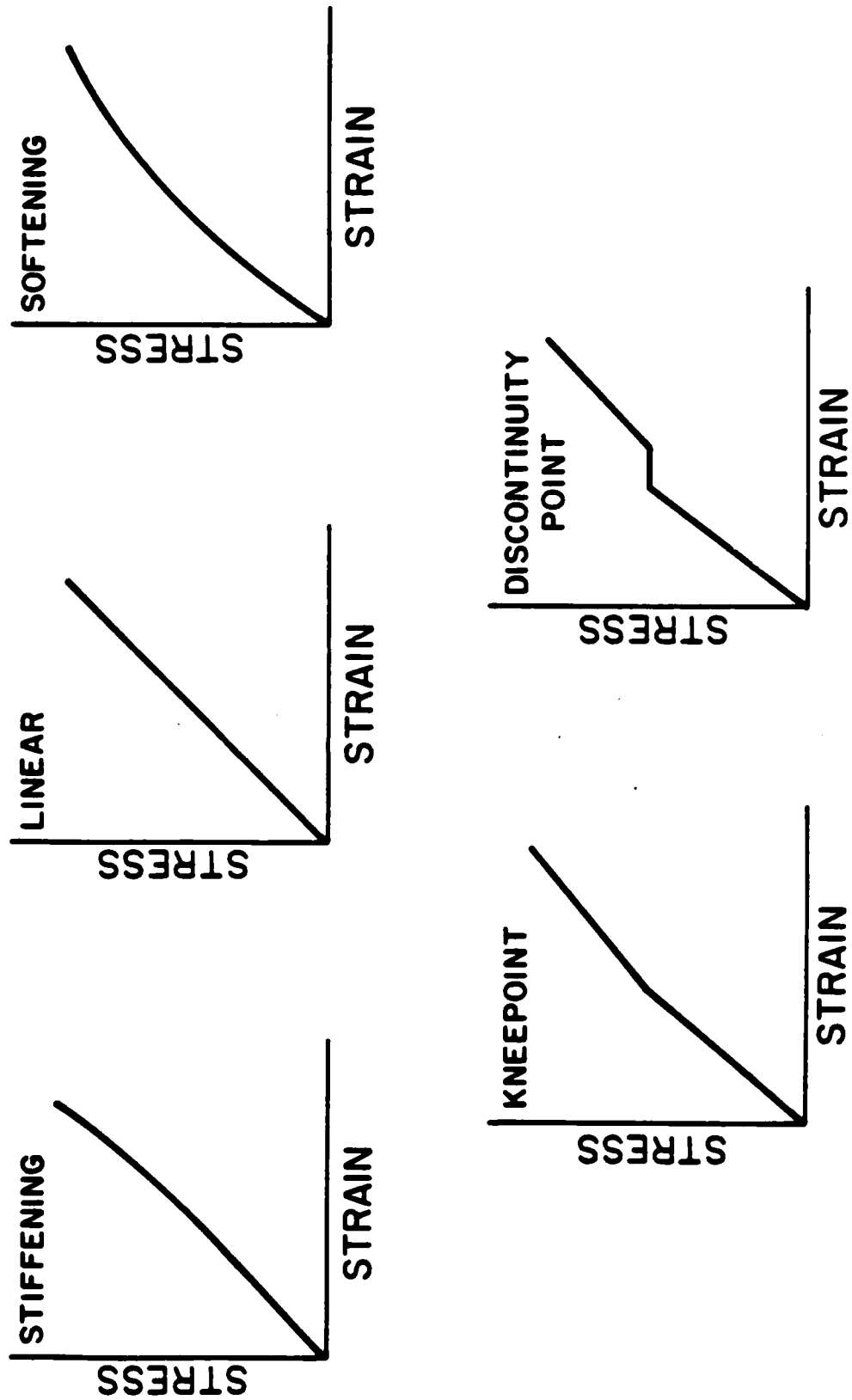


Figure 8 Five types of stress-strain behavior observed in graphite/epoxy laminates.

effects, since this configuration exhibits the greatest amount of nonlinear stress-strain behavior. The work undertaken sought to provide a basic understanding of this nonlinear behavior as well as to look at the consequences of unloading and reloading composites with such stress-strain curves.

Work accomplished during the past year completed the experimental portion of this work by filling in "voids" in the experimental matrix. The entire experimental matrix is shown in Table 4. The experiments done during the past year were on the  $[0]_2$ ,  $[\pm 25]_s$ ,  $[\pm 40]_s$ ,  $[\pm 50]_s$ , and  $[\pm 55]_s$  laminates. The eight different types of tests conducted throughout the program are divided into three major sections as shown in Table 4. The first is a monotonic to failure test. The second involves loading the specimen to some point in the nonlinear region, as defined in Figure 9, unloading the specimen, and then loading it monotonically to failure. The third test involves cyclically loading the specimen to some point in the nonlinear region for 100 cycles and then conducting a monotonic to failure test. The code used in Table 4 is:

A=load to failure

B=load to quarter point, unload, load to failure

C=load to third point, unload, load to failure

D=load to half point, unload, load to failure

E=load to two-thirds point, unload, load to failure

F=load to three-quarters point, unload, load to failure

G=100 load-unload cycles to third point, load to failure

Table 4 Experimental test program for nonlinear stress-strain behavior of  $[\pm\theta]_s$  laminates

Test Type										
Initial Maximum Load Point =	Monotonic A	Hysteresis						Cyclic		
		B	C	D	E	F	G	H		
$\theta$	Failure	1/4	1/3	1/2	2/3	3/4	1/3	2/3		
$0^{\circ b}$	5 <sup>a</sup>	-	-	5	-	-	-	-	-	-
$5^{\circ}$	3	-	3	-	3	-	3	3	3	3
$10^{\circ}$	3	-	3	-	3	-	3	3	3	3
$15^{\circ}$	3	-	3	-	3	-	3	3	3	3
$20^{\circ}$	3	-	3	-	3	-	3	3	3	3
$25^{\circ}$	5	-	-	5	-	-	-	-	-	-
$30^{\circ}$	3	5	-	5	-	5	-	-	-	-
$35^{\circ}$	3	5	-	5	-	5	-	-	-	-
$40^{\circ}$	5	-	-	5	-	-	-	-	-	-
$45^{\circ}$	5	5	-	5	-	5	-	-	-	-
$50^{\circ}$	5	-	-	5	-	-	-	-	-	-
$55^{\circ}$	5	-	-	5	-	-	-	-	-	-
$60^{\circ}$	5	-	-	-	-	-	-	-	-	-
$75^{\circ}$	5	-	-	-	-	-	-	-	-	-
$90^{\circ}$	5	-	-	-	-	-	-	-	-	-

<sup>a</sup> Number indicates number of specimens tested.

<sup>b</sup>  $0^\circ$  specimens were  $[0_{12}]$ , not  $[0_4]$

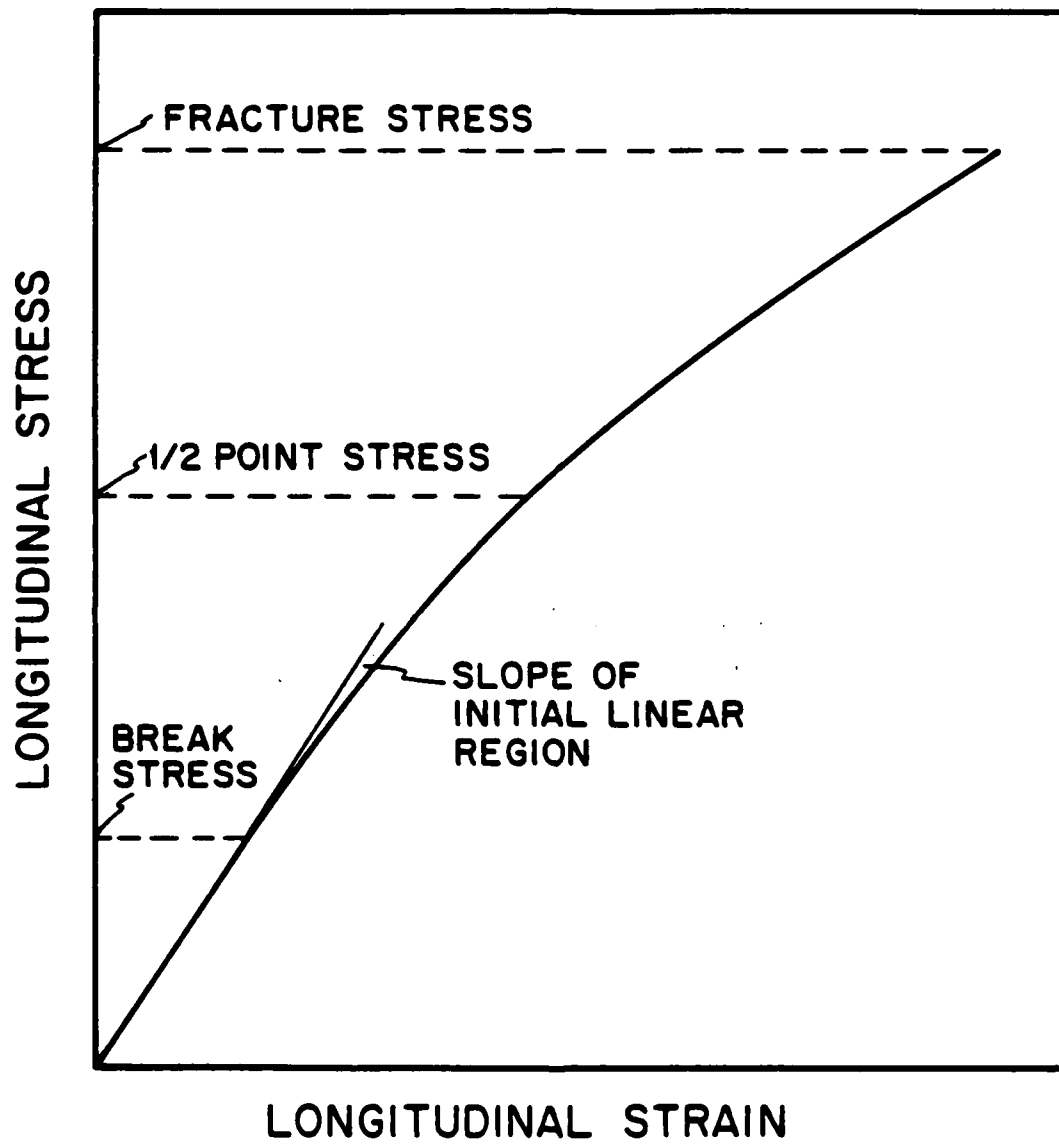


Figure 9

Generic nonlinear stress-strain curve illustrating break stress, fracture stress, and intermediate points.

H=100 load-unload cycles to two-thirds point, load to failure

The laminates tested during this year of effort showed similar trends to the previous laminates which were tested. Of most immediate interest is the classification of the stress-strain behavior of a specific laminate. This is determined by comparing the tangent modulus at failure to the initial tangent modulus. The tangent modulus change from beginning to failure is shown for all the laminates in Figure 10. It can be seen that the  $[\pm\theta]_S$  laminates with  $\theta$  less than  $20^\circ$  exhibit a stiffening, while for  $\theta$  greater than  $20^\circ$ , these same laminates exhibit a significant softening. For the  $[\pm 20]_S$  laminate, these two effects cancel out and the stress-strain behavior is linear-to-failure. This transition is illustrated in Figure 11 where the stress-strain curves for the  $[\pm 15]_S$ ,  $[\pm 20]_S$ ,  $[\pm 25]_S$ , and  $[\pm 30]_S$  laminates are shown. An important point on these curves is the "break stress" which is defined as the point where the stress-strain behavior deviates from linearity. This point was determined using a program called LIN6 [7] which determines linear regions of a data set. A composite plot of these break stresses is shown in Figure 12. Generally, the break stress decreases with increasing lamination angle. Note that there are no break stresses for  $\theta$  greater than  $60^\circ$ . This is due to the fact that the specimen fails at such a low strength that the stress-strain nonlinearity does not occur.

These two groups of laminates also show very different behavior in a hysteresis tests. For the laminates which stiffen

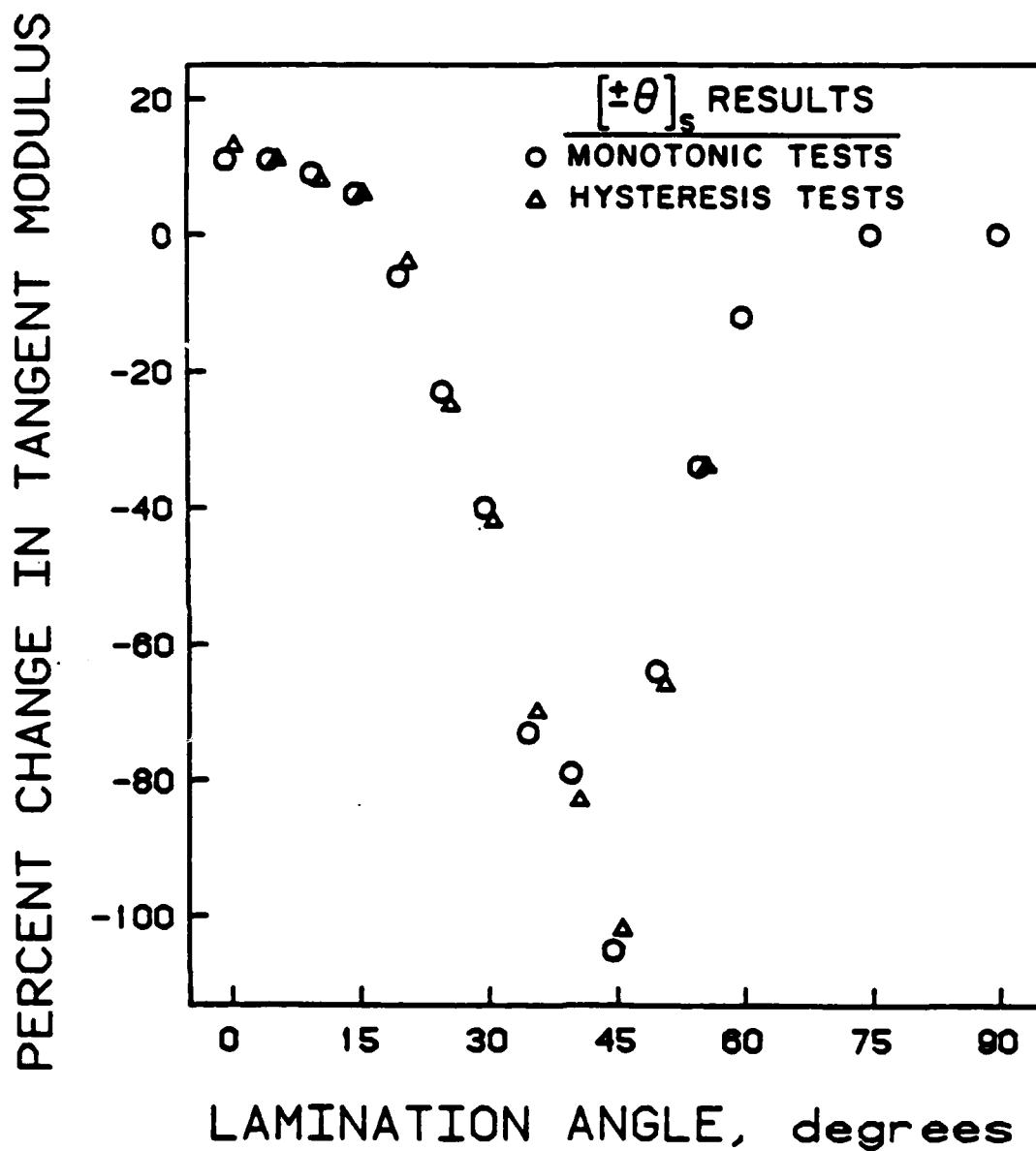


Figure 10 Tangent modulus change from initial to final versus lamination angle for  $[\pm\theta]_s$  specimens.

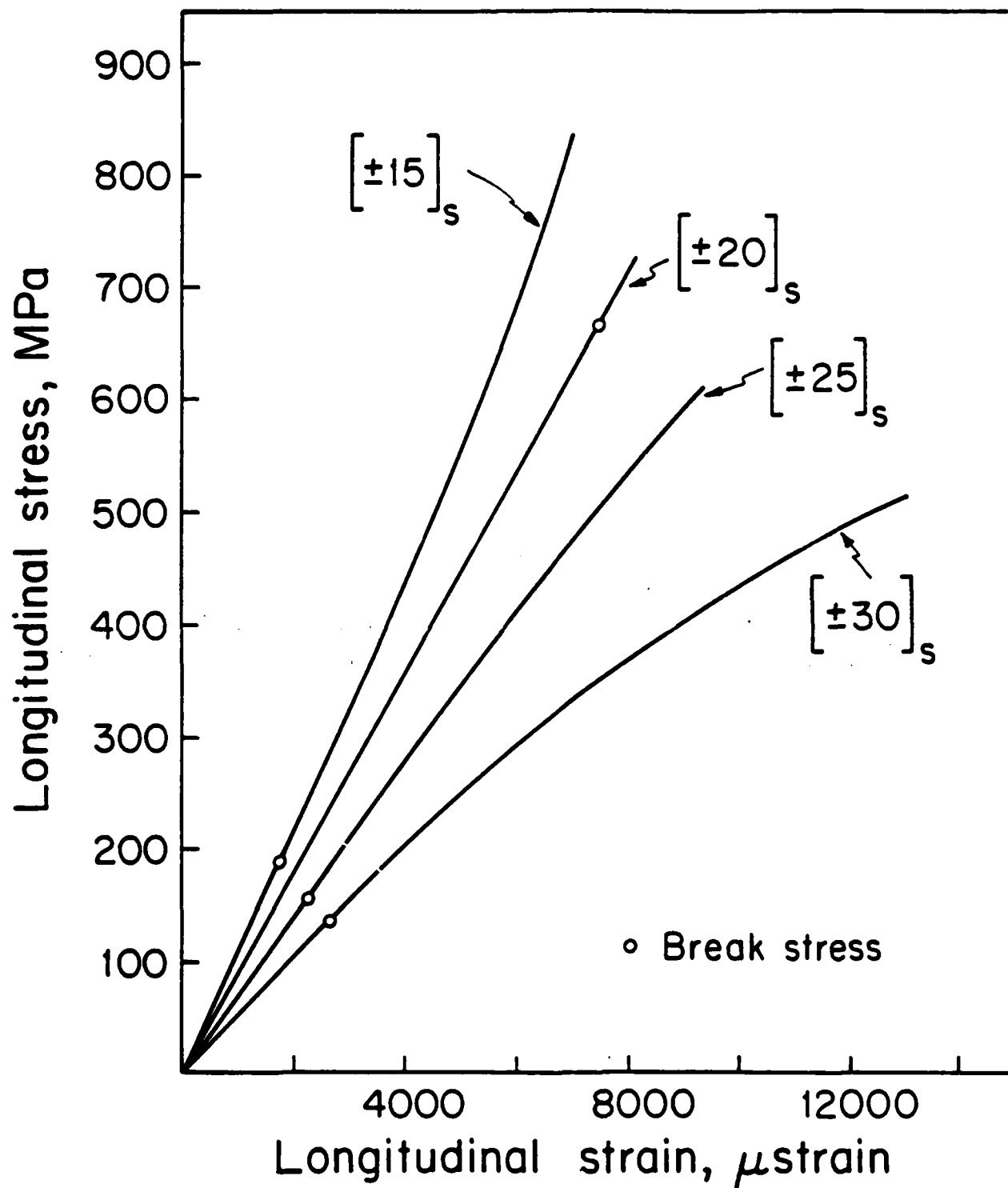


Figure 11 Typical stress-strain behavior of  $[\pm\theta]_s$  laminates for  $\theta$  equal to  $15^\circ$ ,  $20^\circ$ ,  $25^\circ$ , and  $30^\circ$ .

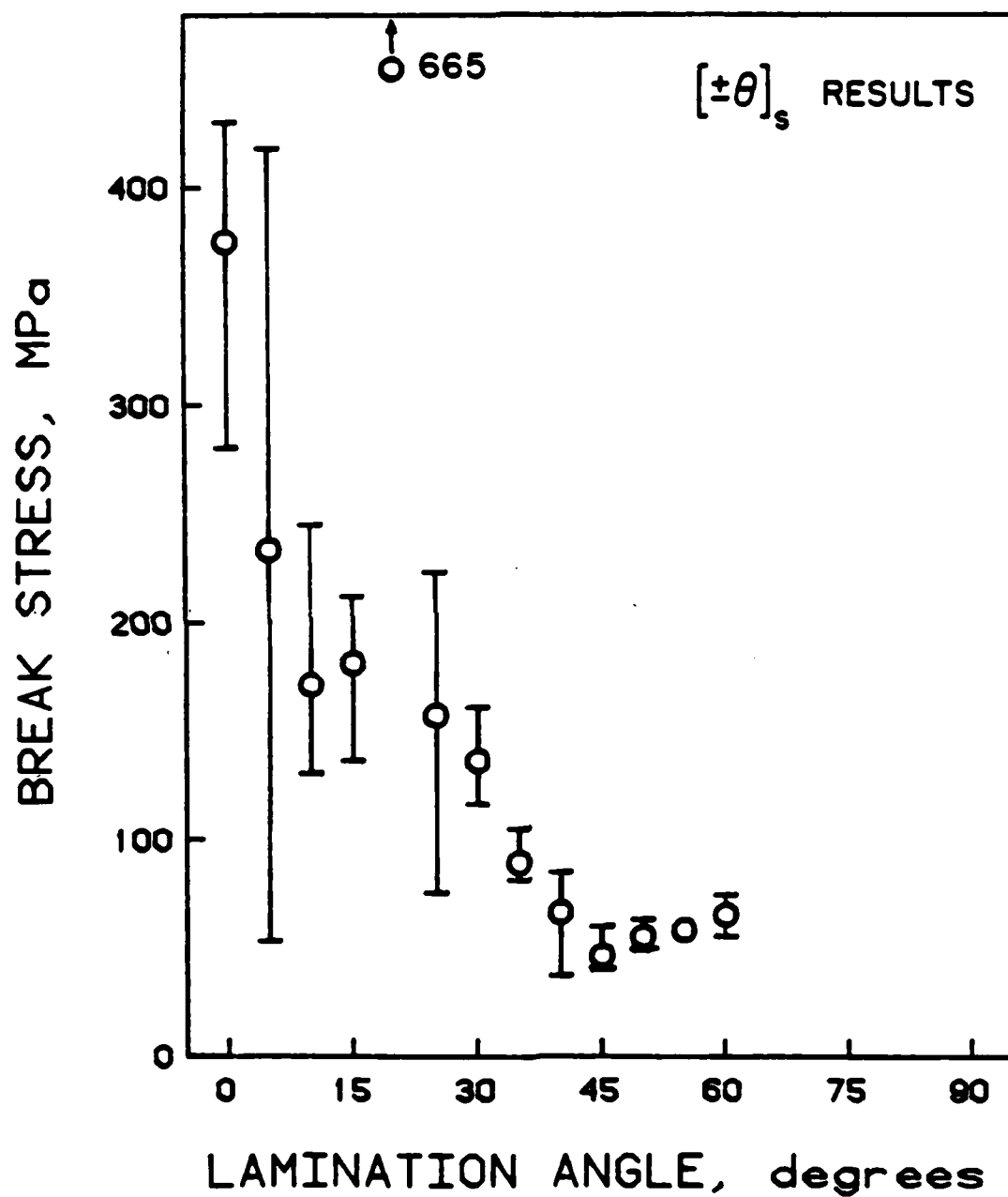


Figure 12 Break stress versus lamination angle for the  $[\pm\theta]_s$  laminates.

( $\theta < 20^\circ$ ), the unload path follows the original load path. Upon reloading, the stress-strain curve follows the same path to failure as for a specimen loaded monotonically to failure. This can be seen for the  $[0]_{12}$  laminate in Figure 13. For the laminates which soften ( $\theta > 20^\circ$ ), the unload stress-strain curve does not follow the original stress-strain curve but shows a decided hysteresis effect as shown for the  $[\pm 30]_s$  laminate in Figure 14. Furthermore, the measured strain does not return to zero upon unloading to zero, but a "permanent strain" remains. These permanent strains are plotted versus lamination angle in Figure 15. As would be expected, the amount of permanent strain increases the further the initial loading traversed into the nonlinear region. The amount of permanent strain also peaked approximately with the laminate which showed the greatest amount of softening.

It is important to point out that upon reloading to failure the laminates that soften, the stress-strain curve has the same initial modulus as for the specimens loaded monotonically to failure, and the stress-strain curve eventually rejoins the original stress-strain curve at the point to which the specimen was originally loaded (See Figure 14). No reduction in the ultimate failure stress was noted.

There appear to be two main contributors to the nonlinear stress-strain behavior in these laminates. The stiffening is provided by slight stiffening of the fibers in longitudinal tension. The softening is due to shear in the unidirectional ply and the nonlinearity associated with this type of loading.

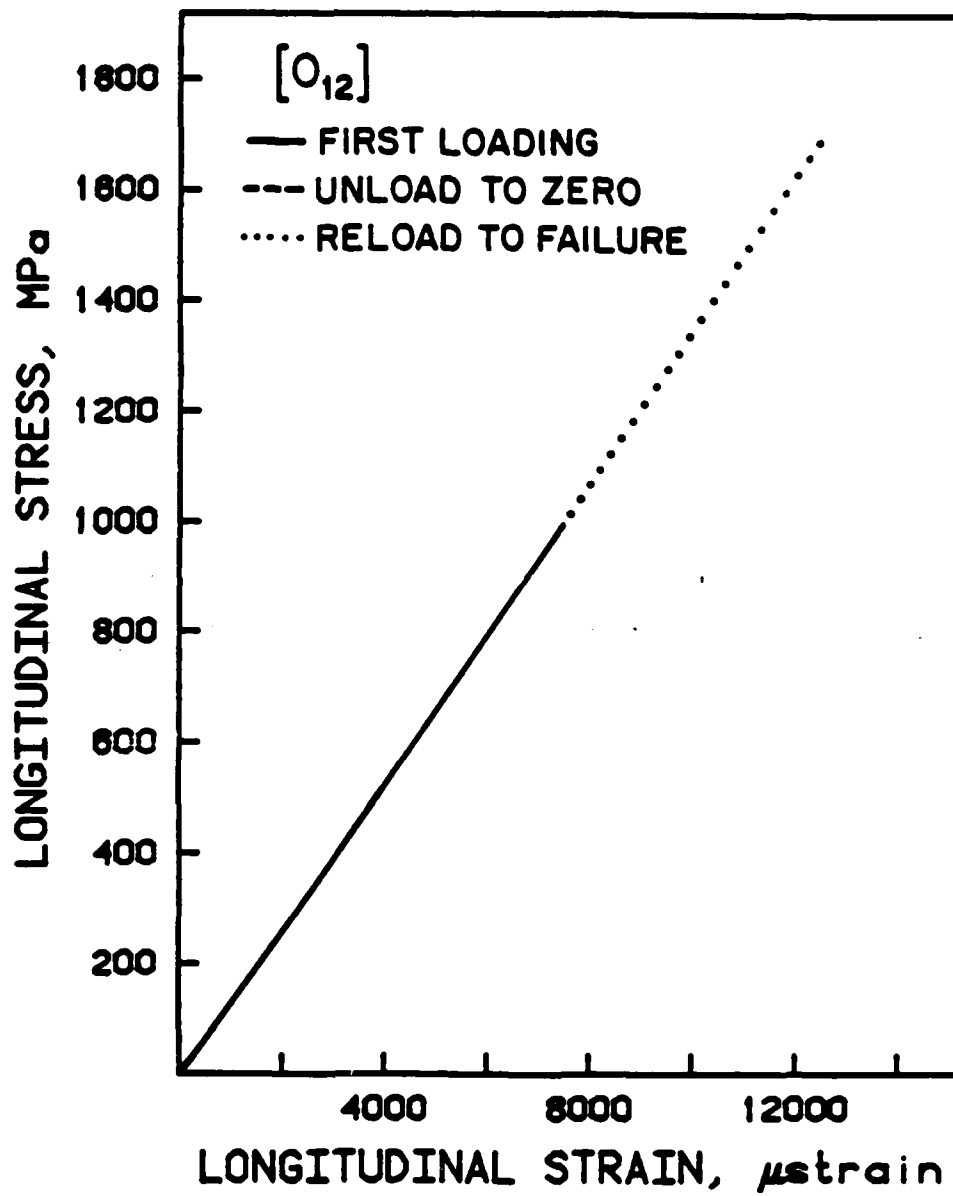


Figure 13 Typical  $[0_{12}]$  stress-strain behavior for load, unload, reload-to-failure cycle.

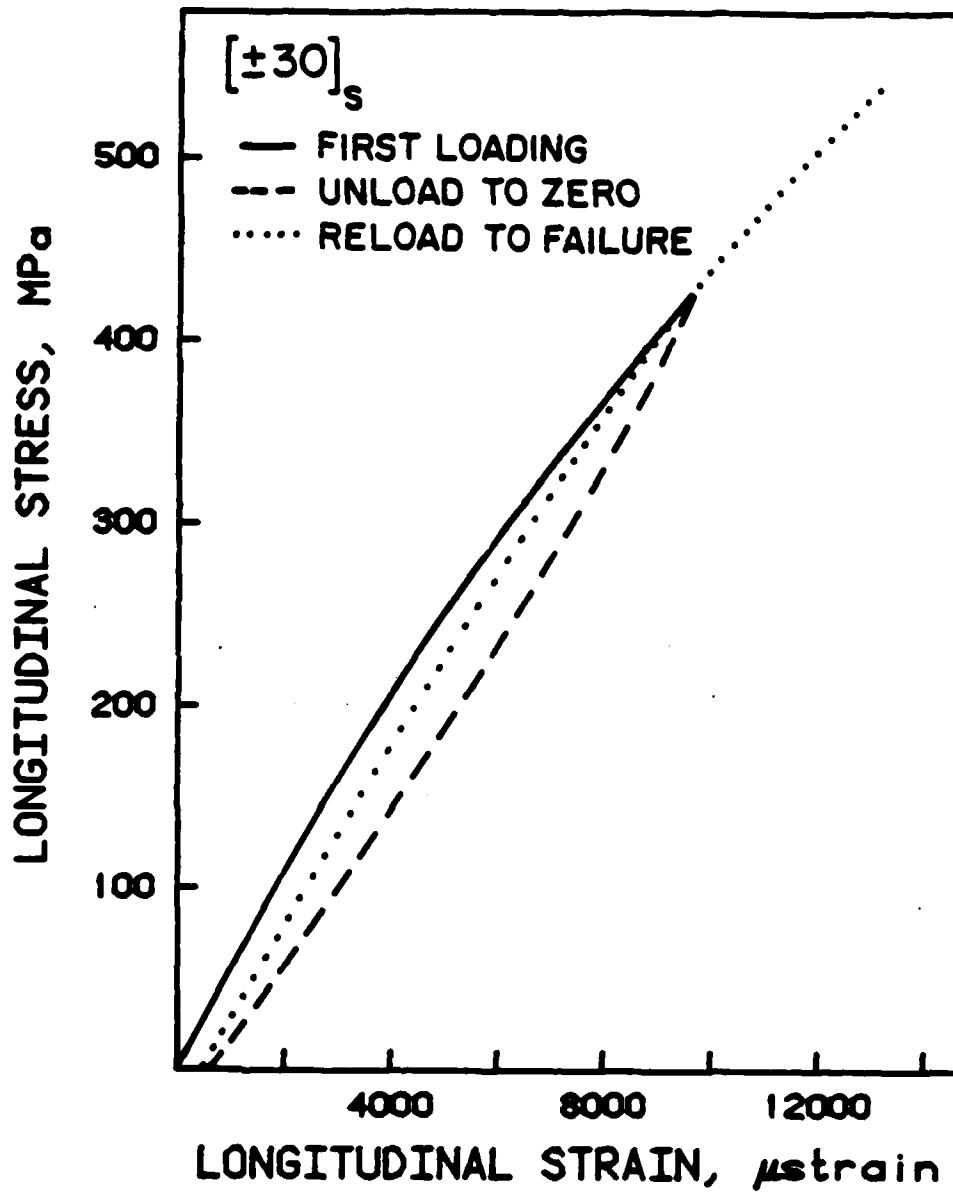


Figure 14 Typical  $[\pm 30]_s$  stress-strain behavior for load, unload, reload-to-failure cycle.

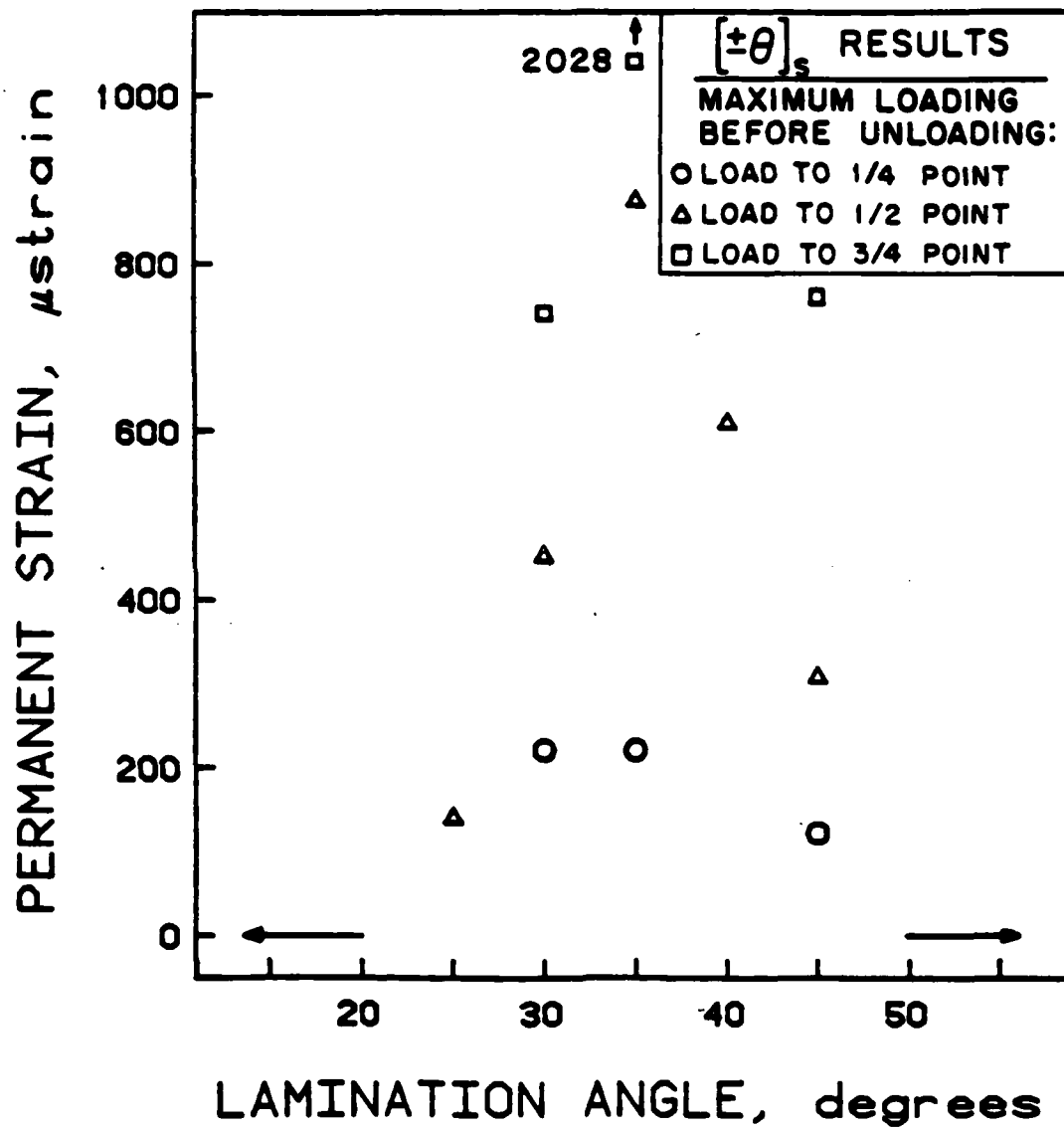


Figure 15 Permanent strains after one load-unload cycle versus lamination angle for  $[\pm\theta]_s$  laminates.

These effects and a more thorough discussion of all the results are provided by Lagace in Reference 8. The work done on the  $[\pm\theta]_s$  laminates with  $\theta$  equal to  $0^\circ$ ,  $25^\circ$ ,  $40^\circ$ ,  $50^\circ$ , and  $55^\circ$ , during this past year is detailed by Chin and Chisholm in Reference 9.

The laminates which soften show permanent strain after one load-unload cycle, but do not exhibit any degradation in ultimate strength. However, it is likely that after many such load-unload cycles, permanent strain would accumulate and the ultimate strength of the laminate may be affected.

To investigate this possibility, ten  $[\pm 35]_s$  graphite/epoxy standard tensile specimens were manufactured and tested under cyclic load. This layup was chosen since it exhibits a large nonlinear stress-strain region and significant permanent strain under hysteresis loading (see Figure 15). Cyclic tensile tests were run with a stress ratio of 0.1 and a maximum stress of 255 MPa. This stress level is halfway into the nonlinear region (see Figure 9) and represents 60% of the ultimate stress. All cyclic tests were run in load control at a rate of 3 Hz. Cyclic loading was stopped from time to time to perform a quasi-static test in order to obtain a stress-strain curve up to 255 MPa after a certain number of load cycles.

The problem encountered in the experimentation involved the strain gages used. These experiments required a strain gage which could both measure very high strains ( $>2\%$ ) and also withstand cyclic loading. Generally, "fatigue gages" (Micro

Measurements gage ED-04-125AD-350 was used) have a strain limit near 1%, while high elongation gages (Micro Measurements gage EP-08-125EQ-120 was used) are not made to withstand cyclic loading. Thus, there was some inconsistency in the strain data obtained. After several tests, a method was devised where the high elongation gages produced reasonable data. Some of this data is shown in Table 5.

The results clearly show that there is a significant reduction in strength due to this cyclic loading into the nonlinear region. The results are summarized in Table 5 which shows the number of cycles to failure for each of the nine  $[\pm 35]_s$  specimens tested. Except for specimen 7, the number of cycles to failure is relatively consistent around 10,000. Additionally, permanent strain measured by the EP gage at three intervals are given. These results show that significant permanent strain does accumulate during cyclic loading.

The magnitude of the permanent strain indicates that there probably is some type of damage beyond the pure stress-strain nonlinearity. It has been suggested by some researchers that transverse cracking in off-axis plies is the source of some nonlinearity in stress-strain behavior. Work will be performed to monitor the amount of transverse cracking which occurs in these types of specimens in order to determine how much of the stress-strain nonlinearity (in this case softening) is due to material nonlinearity and how much is due to transverse cracking. In addition, this work will be extended to  $[\pm \theta]_s$  laminate with holes. The strain at the hole is amplified due to

Table 5 Cycles to failure and permanent strains for  
[+35]s graphite/epoxy specimens subjected to  
tension-tension cyclic loading

SPECIMEN #	PERMANENT STRAIN [microstrain] AFTER ...			NUMBER OF CYCLES TO FAILURE
	2500 CYCLES	5000 CYCLES	7500 CYCLES	
1	a	a	a	7,985
2	a	a	a	9,166
3	a	a	a	8,597
4	a	a	a	8,735
5	a	a	a	8,026
6	22,000	29,700	35,850	8,250
7	17,175	22,450	25,575	26,420
8	21,750	27,450	30,950	11,300
9	18,675	25,300	28,750	13,600
AVERAGE	19,900	26,225	30,281	11,342
C.V.	(12%)	(12%)	(14%)	(52%)

<sup>a</sup>Gage failure

the stress concentration. Thus, the nonlinearity will be magnified in these cases and this phenomenon will be investigated.

#### 2.4 Comparison of Tapered and Straight-Edged Graphite/Epoxy Coupons

The fracture strengths of specimens with lamination angles of less than  $30^\circ$  fall below the predicted values using accepted failure criteria as shown by the data from Lagace [10]. This data was obtained using the straight-edged coupons shown in Figure 4. It has been suggested that the "premature" failure is a result of the end constraints imposed by the hydraulic gripping of the coupon at the tabs.

An investigation was previously undertaken, as reported in last year's work [1], to compare the straight-edged specimen to a tapered coupon, which has been recently suggested [11] to alleviate any possible load introduction problems at the tab in the straight-edged coupons specimens. The previous results showed that the tapered coupons had slightly lower fracture stresses than the straight-edged as fracture often initiated at the "corner" of the taper. However, these original results were obtained on specimens which had an abnormal resin content (lower than normal). It was thus desirable to repeat these tests using specimens with a normal resin content.

The work accomplished this past year again compared the straight-edged coupon with a tapered coupon designed by Boeing.

This tapered specimen is illustrated in Figure 16. The two six-ply laminates used in the previous work were again chosen for this investigation:  $[\pm 15/0]_S$  and  $[0/\pm 15]_S$ . All specimens were manufactured from Hercules AS1/3501-6 graphite/epoxy. Three laminates of each laminate type were manufactured. Each laminate yielded two straight-edged and four tapered coupons. The tapering of the "Boeing" coupons was done on a milling machine using a diamond grit routing bit. Extreme care was taken in routing the entire test section. Glass/epoxy loading tabs akin to the ones used on the straight-edged specimen were bonded onto the gripping area of each tapered specimen. The tests were all conducted in the standard manner with hydraulic grips.

The stress-strain behavior of the specimens were identical for the two specimen types. The behavior was essentially linear with a slight stiffening (3% to 8% increase in tangent modulus) partway through the test. This stiffening has been seen in previous investigations of the same laminate types [6]. The initial modulus and Poisson's ratio of all specimens were within experimental scatter of Classical Laminated Plate Theory values of 116 GPa and 0.673, respectively, for both laminate types. The average values for each laminate and specimen type are listed in Table 6.

The  $[0/\pm 15]_S$  specimens did not show any sign of the small "plateau" which was visible for the  $[0/\pm 15]_S$  specimens in the previous investigation [1]. Since the  $[0/\pm 15]_S$  laminates appeared shiny in that investigation, this plateau appears to

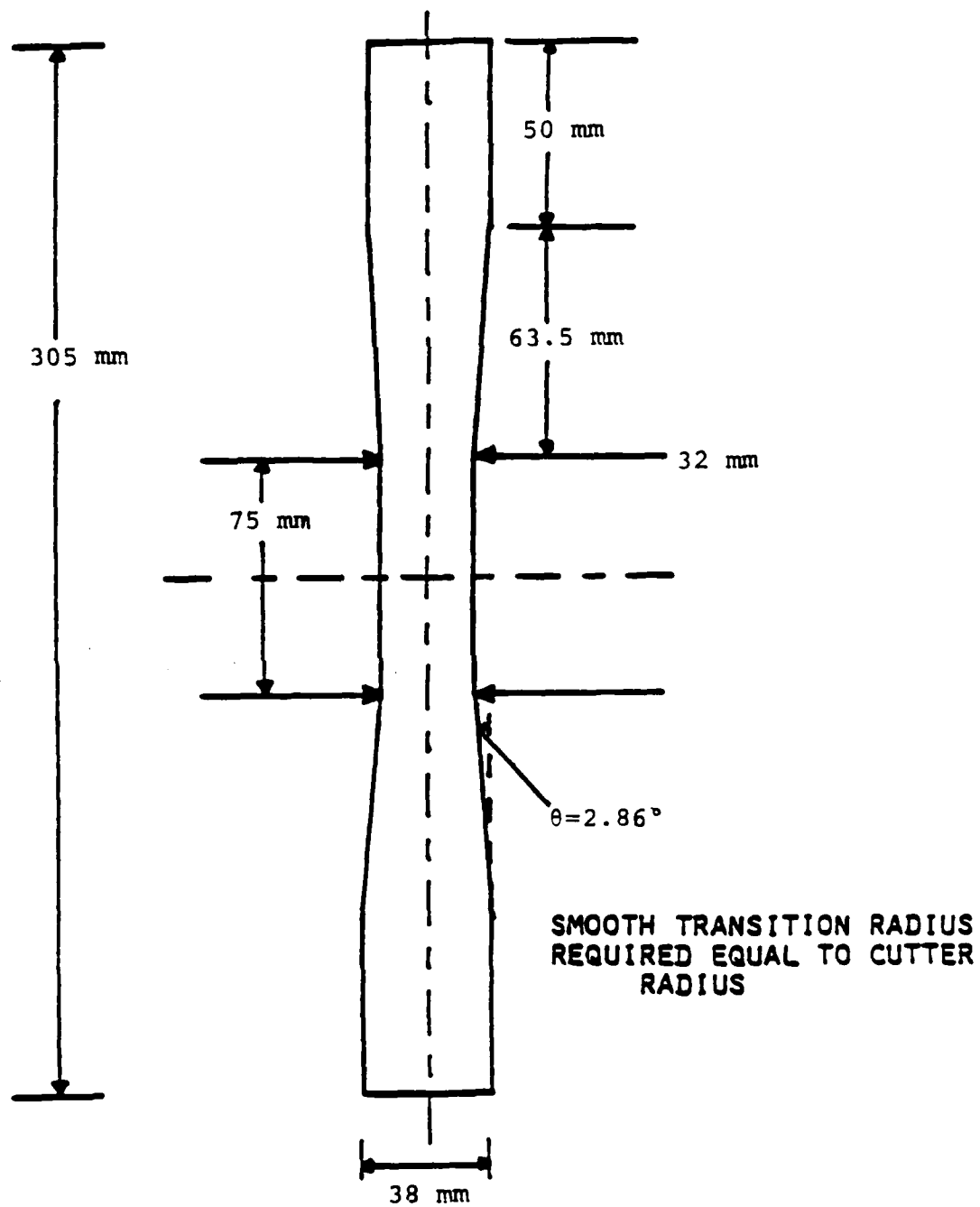


Figure 16

Physical characteristics of the "Boeing"  
tapered coupon specimen.

have been a result of the resin abnormality. The difference in the stress-strain behavior of  $[0/\pm 15]_S$  specimens in the two investigations can be seen in Figures 17 and 18.

The data in Table 6 shows that there is a distinct difference in strength of the specimens of each laminate type between the two types of specimens. The tapered  $[\pm 15/0]_S$  specimens failed at a 7% lower stress than the  $[\pm 15/0]_S$  straight-edged specimens. The tapered  $[0/\pm 15]_S$  specimens failed at a 10% lower stress than the straight-edged ones. These reductions in strength are larger than the coefficients of variation of 3% to 5% and are, thus, significant. These differences are almost identical to the differences found in the previous year's investigation [1].

The fracture mode of each tapered specimen included significant damage at the region where the tapering section meets the test section, i.e. the "corner" of the taper. This was also observed in the previous investigation [1]. This indicates that a stress concentration at the corner of the taper may be responsible for this slightly "premature" failure.

This work shows that a tapered coupon is not an improvement or even a satisfactory substitute for a straight-edged coupon. Although the tapered coupon gives a satisfactory representation of the elastic properties of a laminate, there is a reduction in strength associated with the specimen most likely resulting from a stress concentration at the corner of the taper.

This work is described in more detail by Brewer and Weems in Reference 12.

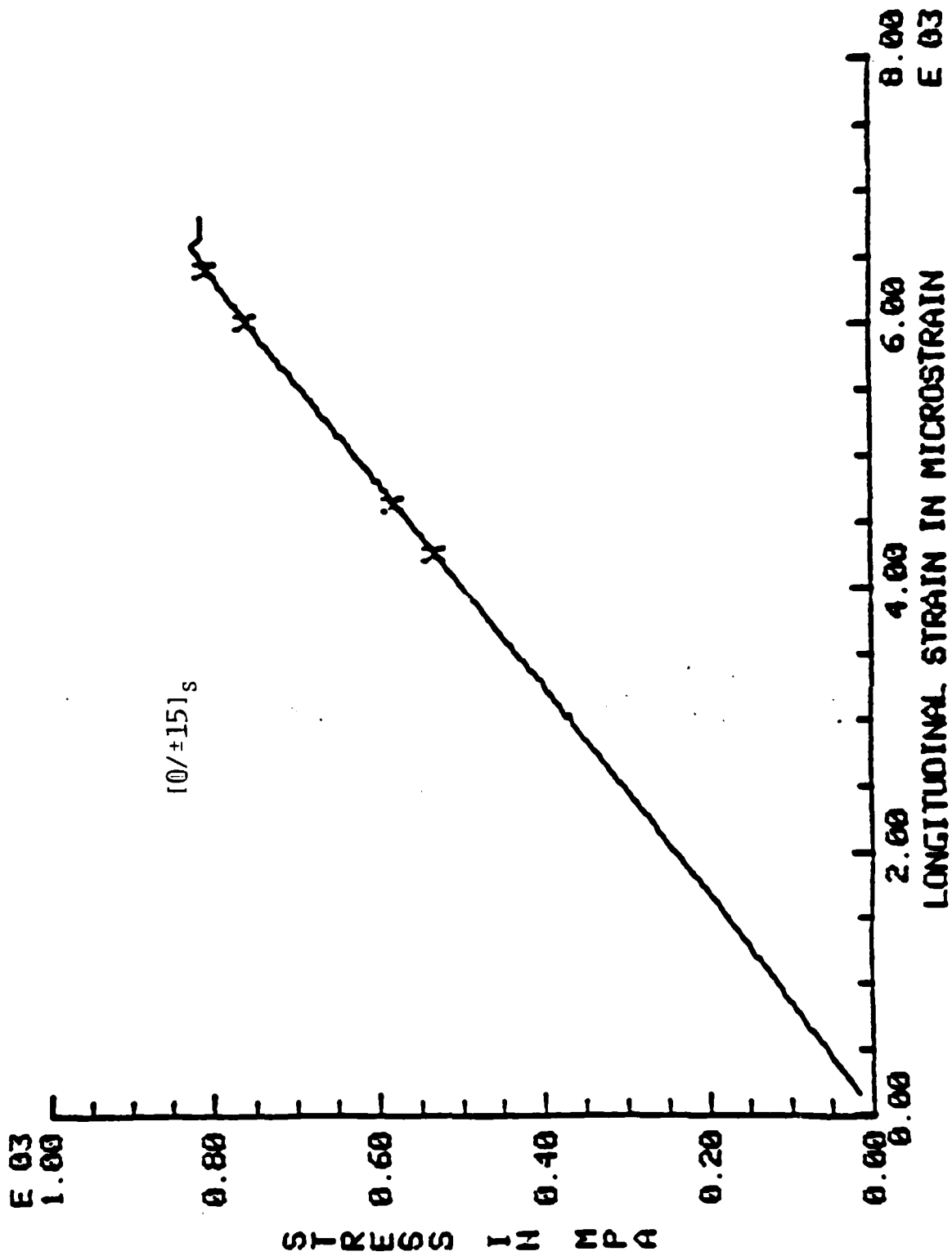


Figure 17 Typical stress-strain behavior for  $[0/\pm 15]_s$  tapered specimen from Reference 1.

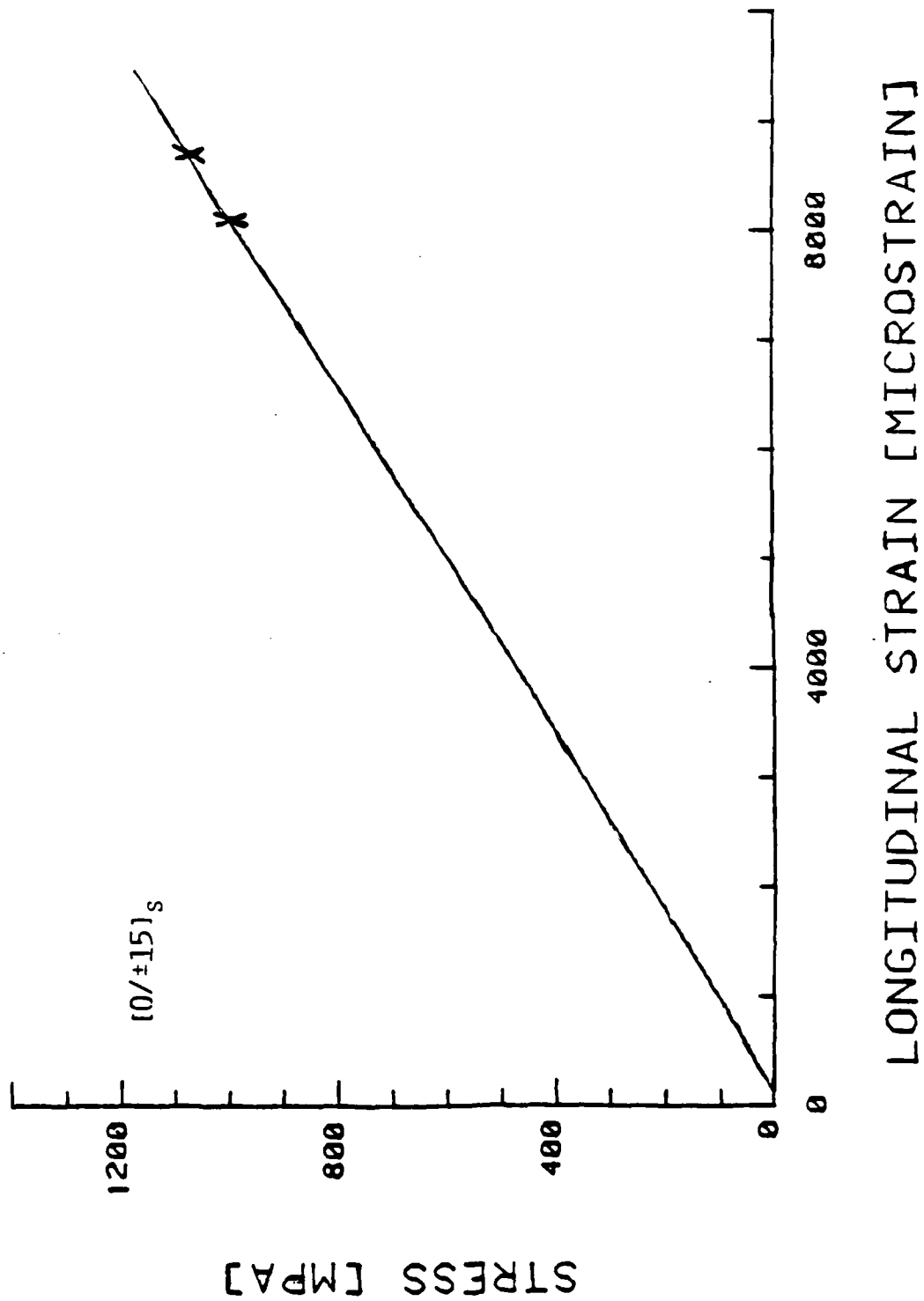


Figure 18 Typical stress-strain behavior for [0/±15]<sub>s</sub> tapered specimen from current work.

Table 6 Experimental results for straight-edged and tapered graphite/epoxy specimens of layouts  $(\pm 15/0)_s$  and  $(0/\pm 15)_s$

Laminate	$(\pm 15/0)_s$		$(0/\pm 15)_s$	
	Coupon Type	Standard	Tapered	Standard
Longitudinal Modulus [GPa]		114 (2.0%) <sup>a</sup>	117 (3.6%)	116 (0.9%)
Poisson's Ratio		0.631 (10.6%)	0.683 (10.8%)	0.689 (18.7%)
Fracture Stress [MPa]		116 (4.4%)	1053 (3.1%)	1277 (3.5%)
Fracture Strain [microstrain]		9058 (3.2%)	8803 (2.5%)	10530 (3.5%)
				9551 (5.3%)

<sup>a</sup> Numbers in parentheses are coefficients of variation.

This leaves unresolved the question of what is responsible for the loss in strength of laminates with lamination angles of less than  $30^\circ$ . The most likely explanation is that these laminates suffer from out-of-plane delamination failure as discussed in section 2.2. This possibility was investigated further and the results are outlined in section 2.5.

### 2.5 Effect of Thickness on Failure by Delamination

Most general failure theories for advanced composite laminates, such as that by Tsai and Wu [5], deal only with in-plane fracture of component plies and are based on the plane stress components predicted by Classical Laminated Plate Theory. As Classical Laminated Plate Theory predicts no effect of ply thickness or stacking sequence on in-plane stresses, there is no related effect on strength predicted from in-plane failure theories.

A great deal of data exists in the literature suggesting that many laminate types are sensitive to stacking sequence and ply thickness effects. Most of these results have been attributable to "out-of-plane" or delamination failure. Delamination is known to be caused by the significant out-of-plane interlaminar stresses that arise in a boundary region near the free edge as a result of the traction-free boundary conditions.

In this investigation, four basic laminate types were studied:  $[\pm 15]_s$ ,  $[\pm 15/0]_s$ ,  $[0/\pm 15]_s$ , and  $[\pm 45/0]_s$ . The

"effective ply thickness" was varied by stacking plies of the same angular orientation together as illustrated in Figure 19. The laminates investigated were:  $[\pm 15_n]_s$  ( $n = 1$  to 5),  $[\pm 15_n/0_n]_s$  ( $n = 1$  to 5),  $[0_n/\pm 15_n]_s$  ( $n = 1$  to 4), and  $[\pm 45_n/0_n]_s$  ( $n = 2$  to 4). The effect of ply thickness was contrasted with the effect of laminate thickness by stacking basic  $[0/\pm 15]_s$  laminates "back-to-back" to form  $[[0/\pm 15]_s]_n$  ( $n = 1$  to 3) laminates. One laminate of each laminate type and effective ply thickness was manufactured and made into five specimens. The testing program is summarized in Table 7.

Each specimen was loaded to tensile failure under stroke control with a nominal strain rate of approximately 5000 microstrain/minute in the test section. The moduli of all specimens were within experimental scatter of the values predicted by Classical Laminated Plate Theory, indicating that Classical Laminated Plate Theory is a valid tool for predicting the in-plane behavior of laminates regardless of ply or laminate thickness.

The failure modes for each laminate type showed increased delamination area with increasing effective ply thickness. However, the failure modes for all  $[[0/\pm 15]_s]_n$  specimens were identical, indicating that ply and not laminate thickness is the controlling parameter. It is important to note that in all cases, each "group" of plies (i.e. each "effective ply") acted as a single unit. This is experimental verification of the "effective ply thickness" concept.

The failure stresses and strains for each laminate type

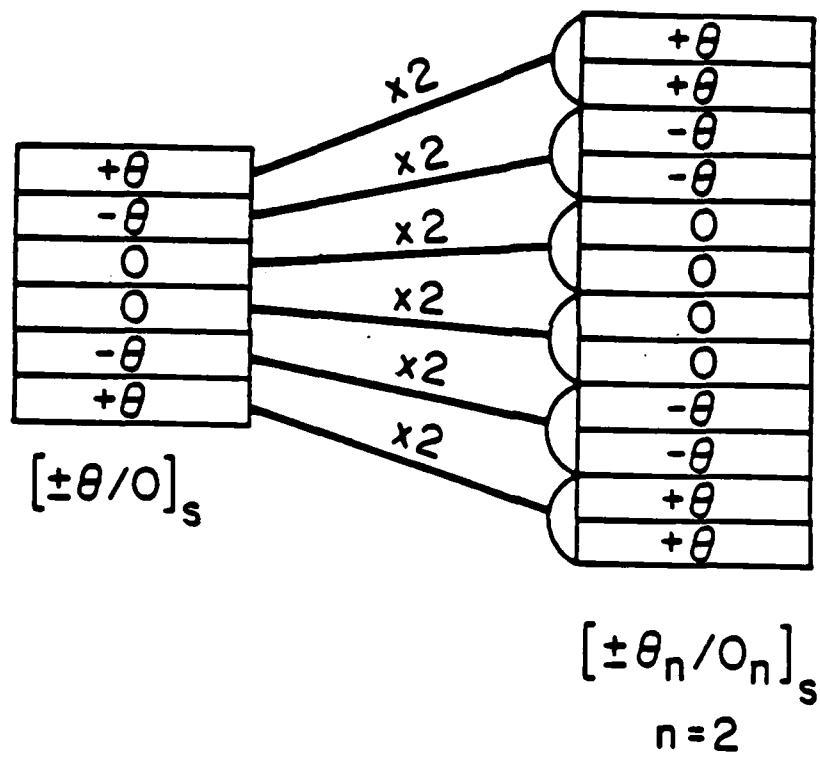


Figure 19 Concept of effective ply thickness.

Table 7      Testing program to determine effect of thickness  
on failure via delamination in graphite/epoxy

Laminate	Number of Specimens
$[\pm 15]_s$	5
$[\pm 15_2]_s$	5
$[\pm 15_3]_s$	5
$[\pm 15_4]_s$	5
$[\pm 15_5]_s$	5
$[\pm 15/0]_s$	5
$[\pm 15_2/0_2]_s$	5
$[\pm 15_3/0_3]_s$	5
$[\pm 15_4/0_4]_s$	5
$[\pm 15_5/0_5]_s$	5
$[0/\pm 15]_s$	5
$[0_2/\pm 15_2]_s$	5
$[0_3/\pm 15_3]_s$	4 <sup>a</sup>
$[0_4/\pm 15_4]_s$	5
$[(0/\pm 15)_s]_2$	5
$[(0/\pm 15)_s]_3$	5
$[\pm 45_2/0_2]_s$	5
$[\pm 45_3/0_3]_s$	5
$[\pm 45_4/0_4]_s$	5

<sup>a</sup>An error in milling caused the loss of  
one specimen

showed a distinct downward trend with increasing effective ply thickness. Once again, however, the  $[[0/\pm15]_s]_n$  specimens showed no difference with the value of  $n$  as the stresses and strains of this laminate were within experimental scatter of one another. The failure stresses and strains of each laminate are summarized in Table 8.

The explanation of the downward trend lies in the character of the interlaminar stresses themselves. The interlaminar stresses for each laminate were calculated using the recently developed Force Balance Method of Lagace and Kassapoglou [13]. It was found that the interlaminar stress distribution for each laminate type is directly proportional to the applied stress and is a function of distance from the free edge normalized by effective ply thickness. The ply thickness effect is significant. As ply thickness increases, the region of relatively high stress extends farther into the interior of the specimen. It becomes more difficult for the specimen to redistribute the high stress and thus specimens with thicker plies will be prone to delamination failure at a lower applied stress.

A rather significant result of this investigation is that the delamination failure and associated ply thickness effect were also observed for the  $[\pm15_n]_s$  and  $[0_n/\pm15_n]_s$  specimens. The calculated interlaminar normal stress ( $\sigma_{zz}$ ) is identically zero throughout the  $[\pm15_n]_s$  specimens and is compressive at the free edge of the  $[0_n/\pm15_n]_s$  specimens. Compressive interlaminar normal stresses are not believed to contribute to delamination

Table 8      Average experimental failure stresses and strains for effective ply thickness tests

Laminate	Failure Stress [MPa]	Coefficient Of Variation	Failure Strain [Micros]	Coefficient Of Variation
[±15]	884	2.3%	7912	3.3%
[±15 <sub>2</sub> ] <sub>s</sub>	657	2.7%	5922	3.6%
[±15 <sub>3</sub> ] <sub>s</sub>	529	6.6%	4896	6.1%
[±15 <sub>4</sub> ] <sub>s</sub>	472	7.3%	4412	2.3%
[±15 <sub>5</sub> ] <sub>s</sub>	451	5.1%	4048	5.7%
[±15/0] <sub>s</sub>	1018	4.8%	8594	5.5%
[±15 <sub>2</sub> /0 <sub>2</sub> ] <sub>s</sub>	763	1.2%	6505	2.4%
[±15 <sub>3</sub> /0 <sub>3</sub> ] <sub>s</sub>	652	6.6%	5703	5.6%
[±15 <sub>4</sub> /0 <sub>4</sub> ] <sub>s</sub>	604	4.6%	5213	3.6%
[±15 <sub>5</sub> /0 <sub>5</sub> ] <sub>s</sub>	624	3.7%	5564	1.9%
[0/±15] <sub>s</sub>	1197	2.5%	10002	2.2%
[0 <sub>2</sub> /±15 <sub>2</sub> ] <sub>s</sub>	863	6.3%	7474	10.6%
[0 <sub>3</sub> /±15 <sub>3</sub> ] <sub>s</sub>	815	4.4%	6985	2.2%
[0 <sub>4</sub> /±15 <sub>4</sub> ] <sub>s</sub>	717	6.1%	6410	2.9%
[[0/±15] <sub>s</sub> ] <sub>2</sub>	1157	6.7%	9640	3.4%
[[0/±15] <sub>s</sub> ] <sub>3</sub>	1177	3.8%	9906	3.2%
[±45 <sub>2</sub> /0 <sub>2</sub> ] <sub>s</sub>	696	9.9%	12340	4.9%
[±45 <sub>3</sub> /0 <sub>3</sub> ] <sub>s</sub>	595	11.1%	10720	3.3%
[±45 <sub>4</sub> /0 <sub>4</sub> ] <sub>s</sub>	549	10.8%	9775	11.5%

failure. This indicates that the interlaminar shear stress ( $\sigma_{1z}$ ) can be at least as important as the interlaminar normal stress in causing delamination failure.

A more in-depth treatment of the results is given by Brewer in Reference 14.

This work has shown that ply thickness has a distinct effect on the delamination failure strength of composites. These effects were shown to be ply thickness and not merely laminate thickness effects. This work has also pointed out that interlaminar shear stress is at least as important as interlaminar normal stress. However, only final failure was measured in these tests. Delamination likely initiates prior to final failure. It is important to determine exactly when delamination initiates. This work is being pursued to determine the point of delamination initiation in the laminates investigated herein. The calculated interlaminar stresses can then be used in formulating a criterion for delamination initiation.

## 2.6 Fracture of Tensile Coupons with Holes

A considerable amount of work has been done in past years on the fracture of graphite/epoxy coupons with holes. This work was summarized in the last annual report [1]. During the past year, this data has been reconsidered and compared with various theoretical correlations.

The data was correlated using the equation proposed by Mar

and Lin [15,16]:

$$\sigma_f = H_c (2r)^{-m} \quad (2.1)$$

where  $2r$  is the notch length and  $\sigma_f$  is the fracture stress. Mar and Lin proposed that  $m$  is the value of the stress singularity at the tip of a discontinuity lying at a fiber/matrix interface. The value of such a singularity was determined by Fenner [17] and is dependent upon the Poisson's ratios and shear moduli of the matrix and filament. The value of  $m$ , taken from the results generated by Fenner, for AS1/3501-6 graphite/epoxy is 0.28.

Originally, the data was correlated by performing a linear regression on the notched fracture stress versus hole diameter on a log-log basis. This yielded experimental values of  $m$  and  $H_c$ , which Mar and Lin called the "composite fracture toughness". In the latest evaluation, the theoretical value of  $m$  was assumed (in this case 0.28) and a value for  $H_c$  for each hole size was determined from the experimental failure stress. An average value of this parameter can be determined for the specific laminate. This parameter is referred to as the "composite fracture parameter" since it is used herein as a parameter to fit the experimental data.

A second correlation was used to correlate the data. This is the point stress criterion proposed by Whitney and Nuismer [18,19]. They proposed that failure would occur when the stress at some characteristic distance  $d_0$  ahead of a notch reached the unnotched failure stress  $\sigma_0$ . Using an approximation for the

stress ahead of a hole, they derived the following equation for the notched fracture stress:

$$\frac{\sigma_f}{\sigma_0} = 2 / \left\{ 2 + \xi_1^2 + 3\xi_1^4 - (K_T^\infty - 3)(5\xi_1^6 - 7\xi_1^8) \right\} \quad (2.2)$$

where

$$\xi_1 = r / (r + d_0) \quad (2.3)$$

Their work suggested that the characteristic length is constant for a specific material. They found  $d_0$  to be 1.02 mm for typical graphite/epoxy systems. The form of this equation suggests that the notched fracture of various stacking sequences, with the same value of  $K_T$ , should be ranked according to their unnotched failure stress. The experimental failure data showed that this is not so. To generalize the Whitney-Nuismer correlation, rather than using the unnotched fracture stress, a "notched fracture stress parameter",  $\sigma_p$ , is proposed. In much the same way that  $H_c$  was determined for the Mar-Lin relation,  $\sigma_p$  can be determined using a value for  $d_0$  of 1.02 mm and the experimental fracture stress. An average value for this notched fracture stress parameter can then be found for each laminate.

These average fracture parameters were used in the respective equations to generate predicted notched fracture curves. Examples of these are shown in Figures 20-22 for  $[\pm\theta/0]_s$ ,  $[0/\pm\theta]_s$ , and  $[+\theta/0/-\theta]_s$  laminates with  $\theta$  equal to  $15^\circ$ ,

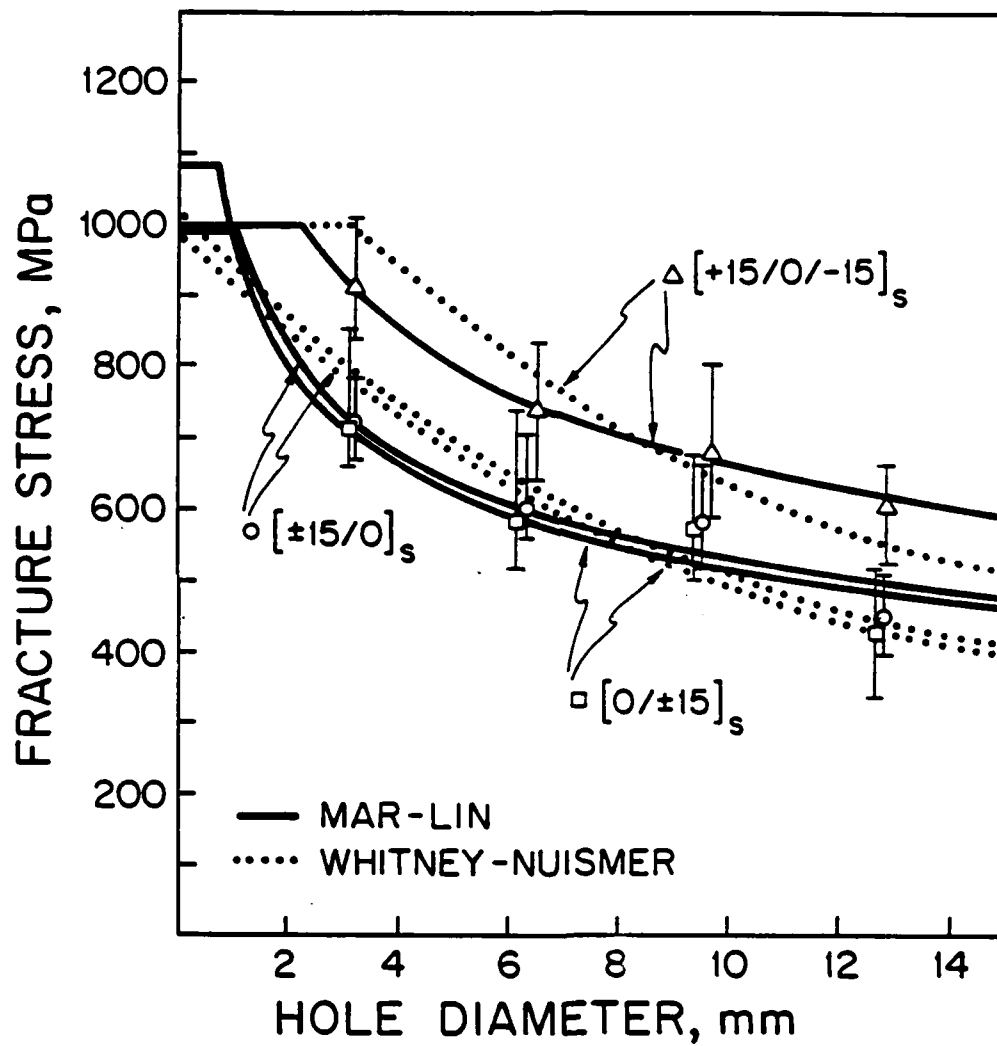


Figure 20

Experimental fracture stresses and theoretical correlations for notched six-ply laminates with  $\theta=15^\circ$ .

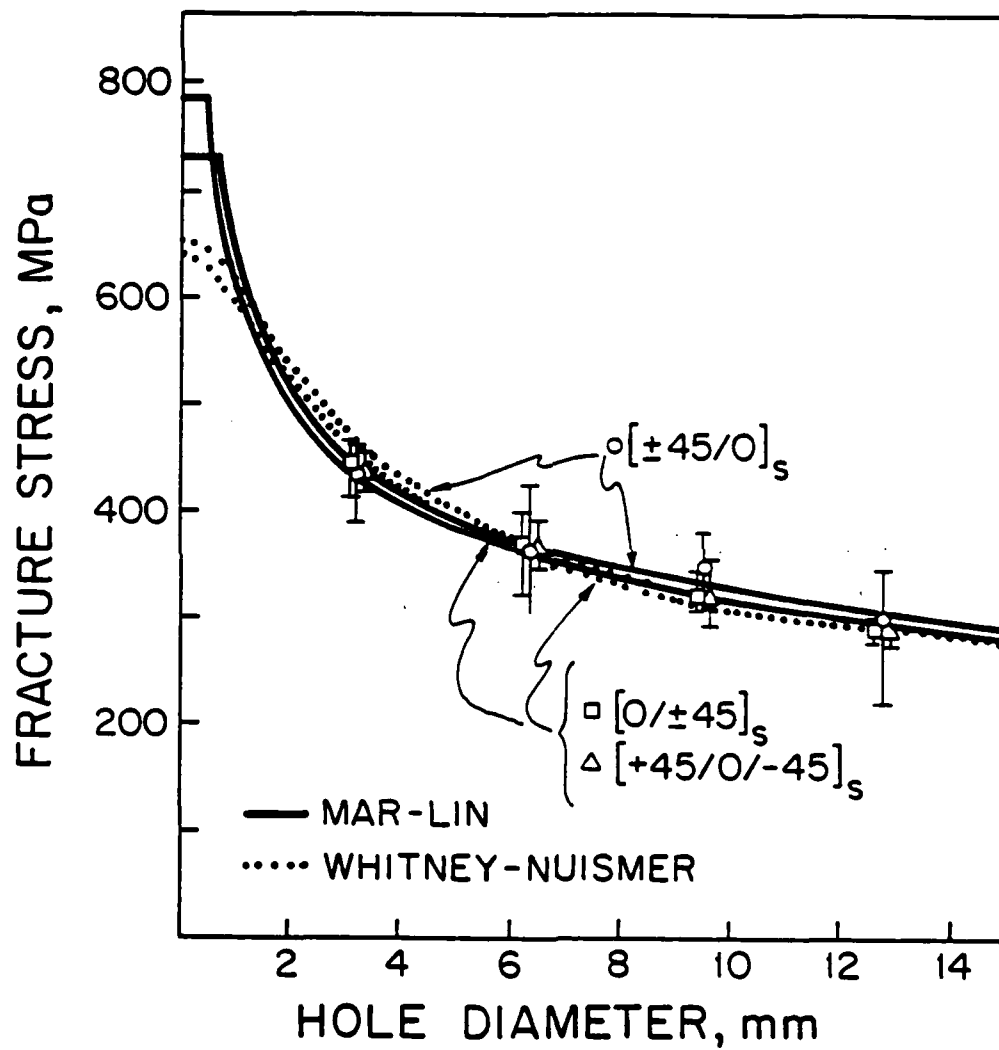


Figure 21 Experimental fracture stresses and theoretical correlations for notched six-ply laminates with  $\theta=45^\circ$ .

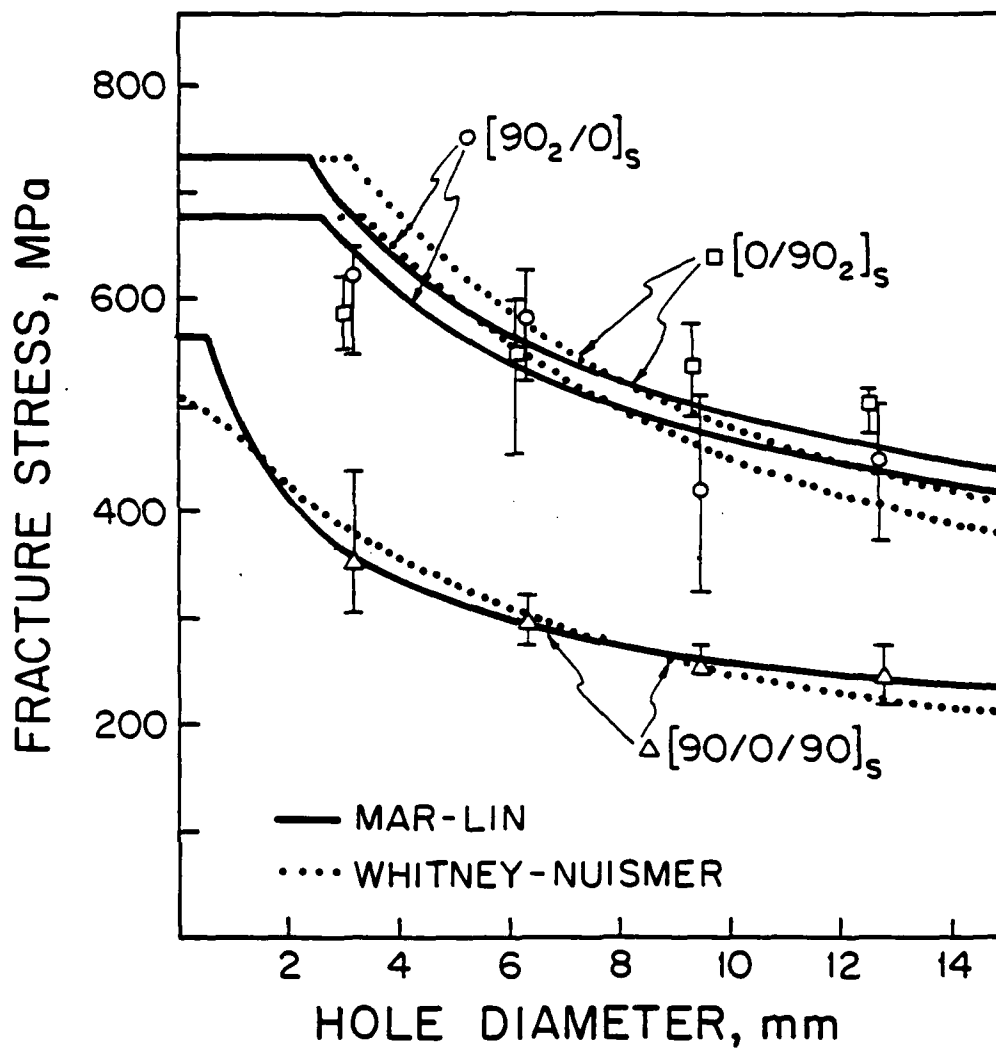


Figure 22

Experimental fracture stresses and theoretical correlations for notched six-ply laminates with  $\theta=90^\circ$ .

45°, and 90° respectively. The horizontal lines in these figures represent the fact that the notched strength cannot exceed the unnotched strength (see section 2.2 for these values).

The two correlations provide relatively similar results. This is especially true for the three six-ply laminates with  $\theta$  equal to 45° as shown in Figure 21. However, the Mar-Lin correlation generally provides a better fit to the data than the Whitney-Nuismer correlation as implemented herein. Generally, the point stress criterion is too "steep" at small hole diameters (approximately 2 to 6 mm) in that the fracture stress predictions overestimate the experimental results. Here, the Mar-Lin correlation provides a better estimate. This difference is accentuated as the hole diameter approaches zero. In all cases, the Mar-Lin correlation line intersects the measured unnotched fracture stress at a point corresponding to, approximately, a 1 to 2 mm diameter hole. This implies that there is a notch size below which the composite is insensitive to the presence of the notch. This is an attractive quality of the correlation and can be attributed to the form of the equation. The point stress criterion, as applied here, does not even reach the unnotched fracture stress for some laminates as illustrated in Figure 20, and thus underestimates the fracture stress for holes of diameters less than 1 to 2 mm.

Overall, the Mar-Lin equation provides slightly better correlation of the data than the modified point stress criterion. The coefficients of variation for  $H_c$  are low. A

composite plot of the composite fracture parameter versus lamination angle for the three symmetric stacking arrangements of the six-ply laminates is shown in Figure 23. These experimental results show that there is an important stacking sequence effect on the strength of notched composites. This dependence is not the same as the dependence of the unnotched tensile strength on the stacking sequence.

Consideration of the results leads to two possible explanations for the observed dependence of notched fracture stress on stacking sequence, both of which deal with out-of-plane effects. The first is the existence of interlaminar stresses which may cause out-of-plane failure (i.e. delamination) to occur in some laminates. The data shown in Figure 22 illustrates this fact. The  $[0/90_2]_s$  laminate failed via delamination for smaller hole sizes. Experimental evidence was shown via photographs in last year's report [1]. Thus, an in-plane correlation cannot be expected to provide a proper correlation. This emphasizes the need for work to predict failure via delamination.

All of the differences in notched fracture stresses cannot be attributed to delamination, however, since these differences existed in cases where delamination did not occur. The explanation offered deals with the "in-situ" strength of individual plies [20]. The strength of any ply changes as the lamination angles of the neighboring plies change. This is due to the differing elastic constraints applied by plies at various angles. By changing the stacking sequence, the "in-situ"

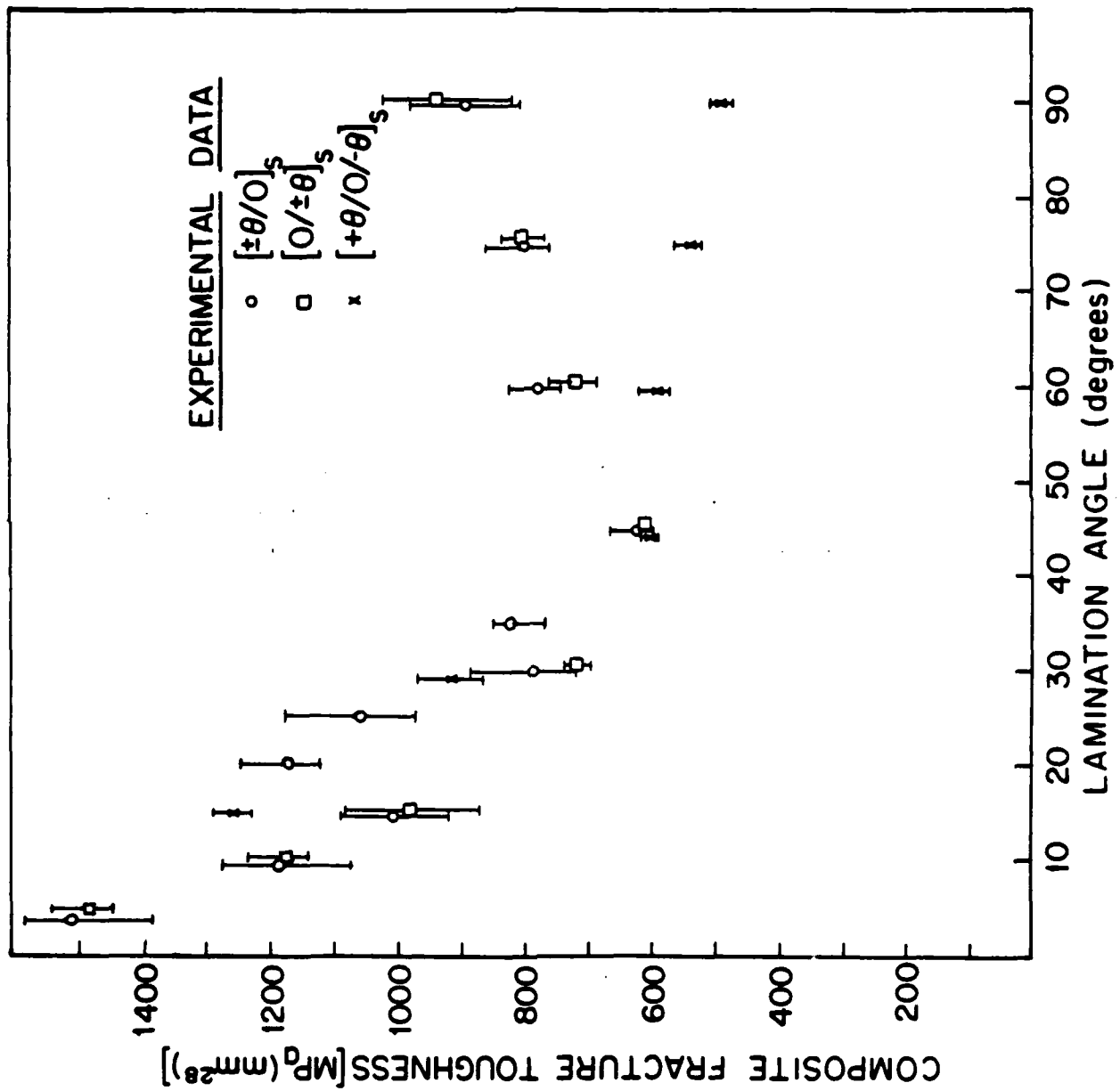


Figure 23

Experimentally-determined composite fracture parameter versus lamination angle for the six-ply laminates.

strength of the individual plies may be changed resulting in a change of the overall laminate notched strength. This can further interact with delamination to cause the important differences observed in the composite fracture parameters.

These analyses are more fully discussed and presented by Lagace in Reference 21. This work is currently being extended to thicker laminates. One case involves effects of ply thickness. Ply thickness is effectively increased (see section 2.5) by having several plies of a specific lamination angle adjacent to each other. This work is currently underway and nearing the testing stage. The second direction involves laminates which have an additional pair of angled plies where the lamination angle of these plies are not equal to the lamination angle of the other pair. This work is reported on in the next section.

### 2.7 Fracture of Laminates with Two Sets of Angled Plies

As reported on in the last section, a methodology exists by which to correlate the notched tensile fracture of graphite/epoxy. However, the experimental correlation of this methodology is restricted to relatively thin laminates. An experimental program was undertaken, and is described here along with the results, to extend this data base to thicker laminates and to examine the applicability of the Mar-Lin equation. Specifically, thicker laminates which had two sets of angled plies at different lamination angles were investigated, i.e.

$[\pm\theta/\pm\alpha/0]_s$ , in order to see how mixing more plies at different angles would influence the fracture behavior.

A total of four laminates were investigated:  $[\pm15/\pm30/0]_s$ ,  $[\pm30/\pm15/0]_s$ ,  $[\pm15/\pm45/0]_s$ , and  $[\pm45/\pm15/0]_s$ , and each were made of AS1/3501-6 graphite/epoxy. For each laminate, three specimens each were made for four hole diameters: 3.175 mm, 6.35 mm, 9.525 mm, and 12.7 mm, along with three unnotched specimen. This testing program is summarized in Table 9. All specimens were instrumented with longitudinal strain gages to obtain values of modulus. The tests were conducted in the standard manner described in section 2.1.

All of the specimens showed essentially linear-to-failure stress-strain behavior. The measured longitudinal moduli (and Poisson's ratios which were also measured for the unnotched coupons) were consistent and agreed with the values calculated from Classical Laminated Plate Theory with the use of the basic ply values listed in Table 3.

The average experimental fracture stresses, and the respective coefficients of variation, are reported in Table 10. There was a decided variation in the unnotched fracture stress with the stacking sequence as well as with changing one lamination angle from  $30^\circ$  to  $45^\circ$ . The change due to the stacking sequence can again be attributed to delamination as was discussed in section 2.2. All the unnotched specimens showed some signs of delamination, however, the  $[\pm15/\pm30/0]_s$  and  $[\pm15/\pm45/0]_s$  unnotched specimens showed the greatest amount of delamination. These two laminates also possess significantly

Table 9 Test program to determine notch sensitivity of graphite/epoxy laminates with two sets of angled plies

Hole Size [mm]	Laminate			
	$[\pm 15/\pm 30/0]_S$	$[\pm 30/\pm 15/0]_S$	$[\pm 15/\pm 45/0]_S$	$[\pm 45/\pm 15/0]_S$
0	3 <sup>a</sup>	3	3	3
3.175	3	3	3	3
6.35	3	3	3	3
9.525	3	3	3	3
12.7	3	3	3	3

<sup>a</sup>Number indicates number of specimens tested.

Table 10      Average experimental fracture stresses for  
graphite/epoxy laminates with two sets of angled  
plies

Hole Size [mm]	Laminate			
	$[\pm 15/\pm 30/0]_S$	$[\pm 30/\pm 15/0]_S$	$[\pm 15/\pm 45/0]_S$	$[\pm 45/\pm 15/0]_S$
0	815 <sup>a</sup> (2.0%) <sup>b</sup>	986 (7.6%)	679 (2.1%)	942 (0.8%)
3.175	716 (1.3%)	760 (12.5%)	650 (2.4%)	772 (12.5%)
6.35	674 (3.5%)	646 (4.0%)	620 (4.8%)	602 (6.7%)
9.525	614 (2.9%)	636 (4.0%)	559 (1.8%)	561 (4.8%)
12.7	515 (4.2%)	476 (4.0%)	488 (4.3%)	498 (4.3%)

<sup>a</sup>Units of stress are MPa.

<sup>b</sup>Numbers in parentheses are coefficients of variation.

lower unnotched fracture stresses than their counterparts with a simple change of stacking sequence:  $[\pm 30/\pm 15/0]_s$  and  $[\pm 45/\pm 15/0]_s$  respectively.

This trend does not appear for the notched fracture stresses, however. Within each of the two groups ( $[\pm 15/\pm 30/0]_s$  and  $[\pm 30/\pm 15/0]_s$  being one group and  $[\pm 15/\pm 45/0]_s$  and  $[\pm 45/\pm 15/0]_s$  being the other group), the average fracture stresses for a given notch size are relatively the same. In all these cases, very little delamination was observed in the postmortem failure modes.

This fact is even better illustrated when the data is correlated using the Mar-Lin equation (see equation 2.1). Once again, since the material is AS1/3501-6 graphite/epoxy, a value of  $m$  of 0.28 was used in the equation, and the composite fracture parameter was determined for each hole size for each laminate using the average measured fracture stress. When these results are averaged for each laminate, it is found that  $H_c$  is  $1090 \text{ MPa(mm)}^{0.28}$  for the  $[\pm 15/\pm 30/0]_s$  laminate and  $1075 \text{ MPa(mm)}^{0.28}$  for the  $[\pm 30/\pm 15/0]_s$  laminate. The associated coefficients of variation are 8.1% and 8.2%, respectively. For the  $[\pm 15/\pm 45/0]_s$  laminate, the average value of  $H_c$  is  $1028 \text{ MPa(mm)}^{0.28}$  while it is  $1036 \text{ MPa(mm)}^{0.28}$  for the  $[\pm 45/\pm 15/0]_s$  laminate. The coefficients of variation are 2.9% and 2.6%.

These average values, and associated coefficients of variation, show two very important results. First, and foremost, the Mar-Lin equation applies to even thicker laminates including those with several different lamination angles. This

is better illustrated in Figures 24 and 25 where, for each laminate group, the experimental fracture stresses are plotted versus the hole diameter along with the Mar-Lin correlation using the averaged value of the composite fracture parameter for the laminate group. The correlating lines fit the data quite well in both cases. The second result, which these figures help to emphasize, is that there is no significant difference in the fracture stress due to the change in stacking sequence within each laminate group. It can further be seen, by considering this data, that the difference in fracture stress for the corresponding notch sizes between the two groups of laminates is relatively small. This is probably due to the fact that the  $0^\circ$  and  $\pm 15^\circ$  plies are the controlling parts in the laminate fracture. Referring back to Figure 23 in section 2.6, the value of the composite fracture parameter for the  $[\pm 15/0]_s$  and  $[0/\pm 15]_s$  laminates is in the range of  $1000 \text{ MPa}(\text{mm})^{0.28}$  while that of the other six-ply stacking arrangement,  $[+15/0/-15]_s$ , is slightly higher at approximately  $1250 \text{ MPa}(\text{mm})^{0.28}$ . These values are in the range of the values of the composite fracture parameter observed here and indicate that indeed the  $0^\circ$  and  $\pm 15^\circ$  plies control the failure.

A thorough discussion of this work is presented by Archard and Park in Reference 22.

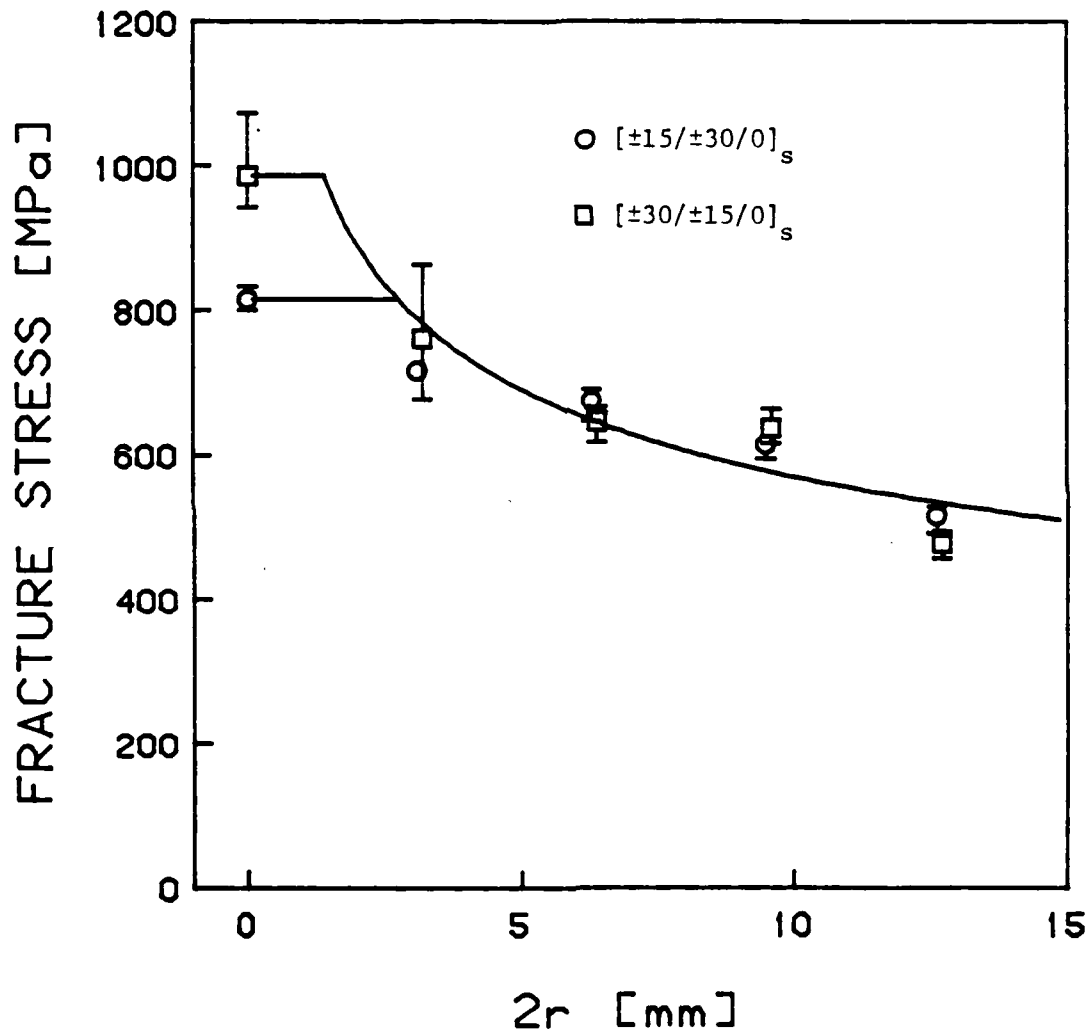


Figure 24 Experimental fracture stresses and theoretical correlation for notched  $[\pm 15/\pm 30/0]_s$  and  $[\pm 30/\pm 15/0]_s$  laminates.

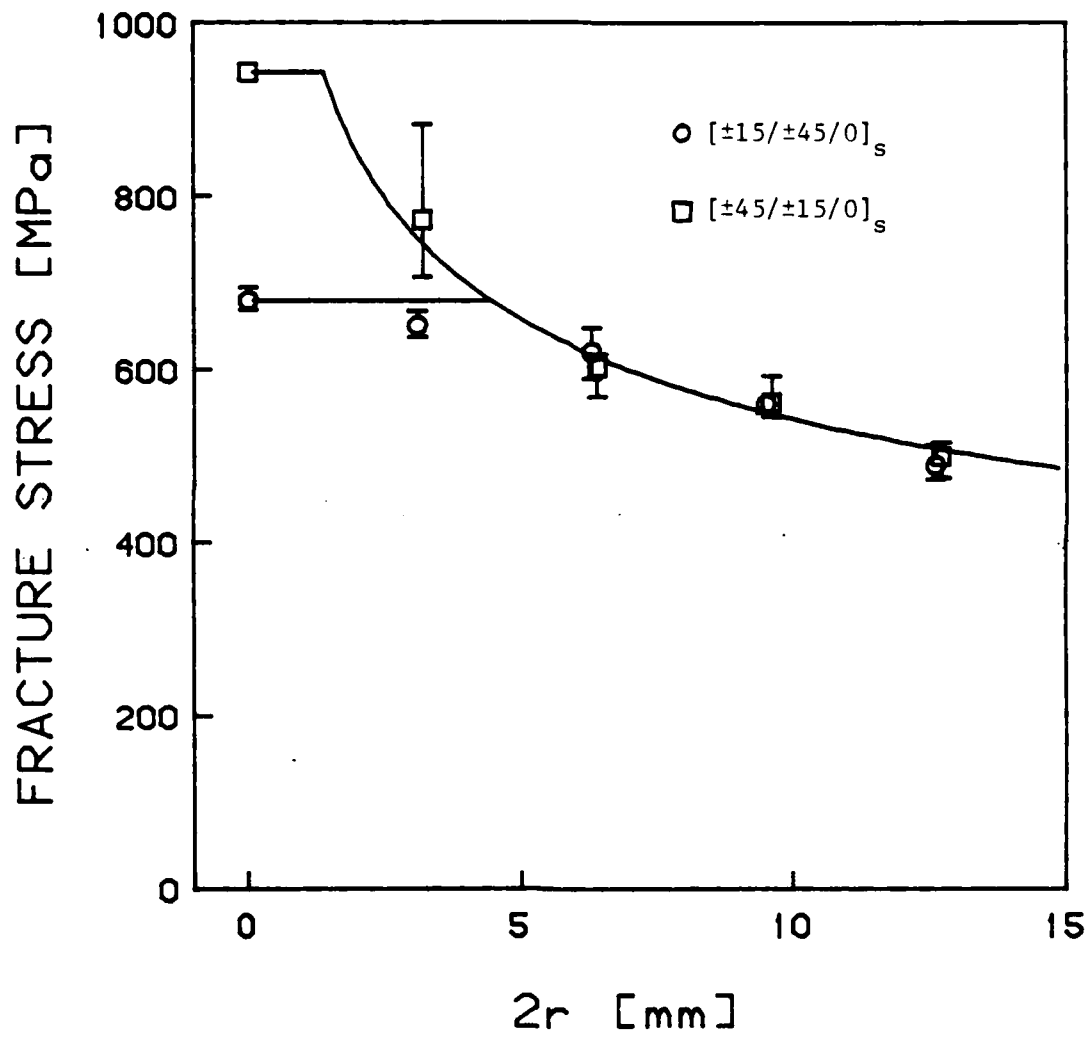


Figure 25 Experimental fracture stresses and theoretical correlation for notched  $[\pm 15/\pm 45/0]_s$  and  $[\pm 45/\pm 15/0]_s$  laminates.

## 2.8 Tensile Properties of Unnotched and Notched Fabric Composites

Fabric composites are seeing increased usage in the aerospace industry. Much of the previous work at TELAC has been performed on laminates manufactured from unidirectional composites. Some work has been conducted on fabric composites as reported for 1982 [1]. It was desirable to expand the experience with fabric composites. Thus, an experiment was undertaken to study the failure of unnotched and notched fabric composite laminates. Hercules A370-5H/3501-6 prepreg was again used as the material.

Five four-ply laminate types were investigated:  $(0,90)_s$ ,  $(90,0)_s$ ,  $(30,60)_s$ ,  $(60,30)_s$ , and  $(+45,-45)_s$ . The angular orientations are the counterclockwise rotations of the warp fibers with respect to the longitudinal axis with the warp and fill directions defined in Figure 26. Five laminates of each laminate type were manufactured and five specimens were cut from each laminate. A hole of a different diameter was drilled in the center of the test section of each of the five specimens: 0 mm (unnotched), 3.175 mm (0.125 in nominal), 6.35 mm (0.25 in nominal), 9.525 mm (0.375 in nominal), and 12.8 mm (0.5 in nominal). The complete test matrix is given in Table 11. The unnotched specimens had strain gages to monitor longitudinal and transverse strain. The notched specimens had one far-field strain gage to monitor longitudinal strain.

All of the specimens had essentially linear stress-strain

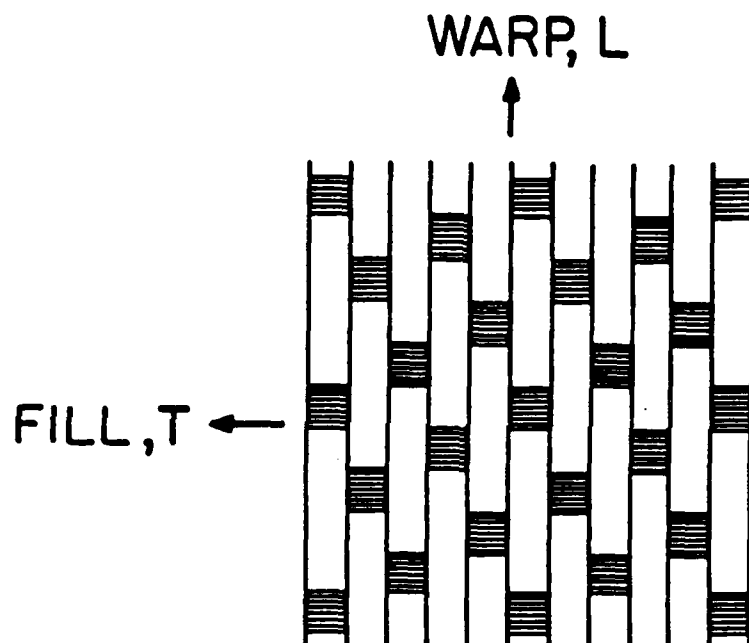


Figure 26 Five harness fabric construction.

**Table 11**      **Test program to determine fracture behavior and notch sensitivity of graphite/epoxy fabric laminates**

Hole Size [mm]	Laminate				
	$(0,90)_S$	$(30,60)_S$	$(+45,-45)_S$	$(60,30)_S$	$(90,0)_S$
Unnotched	5 <sup>a</sup>	5	5	4 <sup>b</sup>	5
3.175	5	5	5	4 <sup>b</sup>	5
6.35	5	5	5	4 <sup>b</sup>	5
9.525	5	5	5	4 <sup>b</sup>	5
12.7	5	5	5	4 <sup>b</sup>	5

<sup>a</sup>Number indicates number of specimen tested.

<sup>b</sup>One plate was irregular and not included in the data base thereby reducing the useful specimens to four of each type.

behavior in the initial loading region. The  $(+45,-45)_s$ , and, to a lesser extent, the  $(30,60)_s$  and  $(60,30)_s$  laminates showed nonlinear behavior later in the tests. The  $(0,90)_s$  and  $(90,0)_s$  specimens showed some nonlinearities after the onset of internal damage. Typical stress-strain plots are shown in Figures 27 through 29. The average longitudinal moduli and Poisson's ratios of the initial linear region of each laminate type were tabulated and agree well with the values predicted by Classical Laminated Plate Theory using the elastic properties of the basic fabric ply as determined by Chang and deLuis [23].

The final failures of the specimens can be separated into two groups: those which failed at the hole and those which failed away from the hole. The specimens which failed away from the hole include all of the  $(30,60)_s$  and  $(60,30)_s$  specimens with 3.175 mm holes, one of the five  $(30,60)_s$  specimens with a 6.35 mm hole and three of the five  $(+45,-45)_s$  specimens with 3.175 mm holes. These 14 specimens failed at similar stress levels to the unnotched specimens of the same laminate types and with similar failure modes. It can be seen, therefore, that the notch-dominated failure is in competition with unnotched failure for small notch sizes. The  $(30,60)_s$ ,  $(60,30)_s$ , and  $(+45,-45)_s$  laminates seem to be insensitive to notches of up to 3 mm in size.

The average failure stresses for each laminate type and hole size are tabulated in Table 12. The failures which occurred away from the hole were considered to be unnotched failures and were omitted from the notched failure data base.

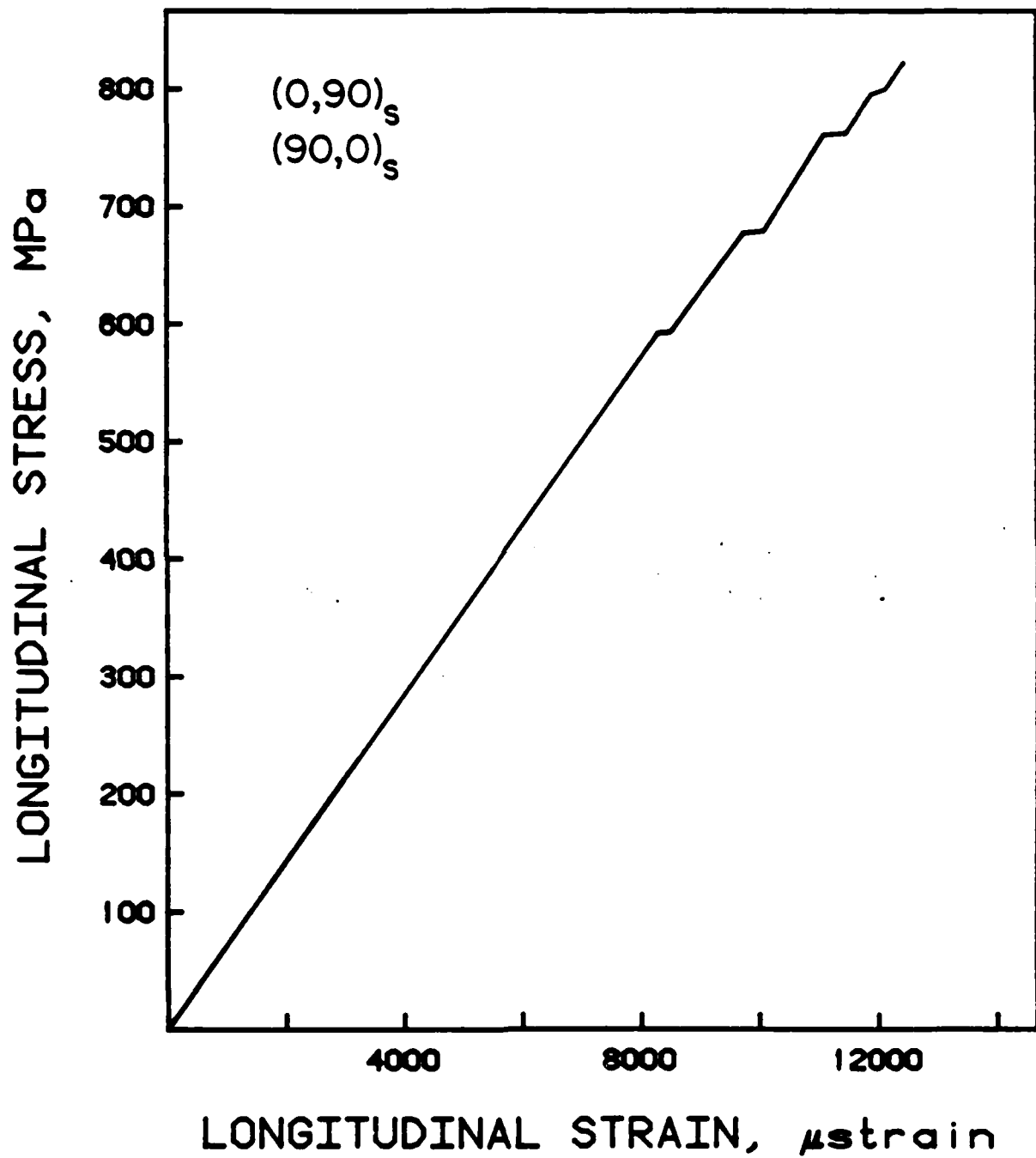


Figure 27 Typical stress-strain behavior of  $(0,90)_s$  and  $(90,0)_s$  unnotched fabric laminates.

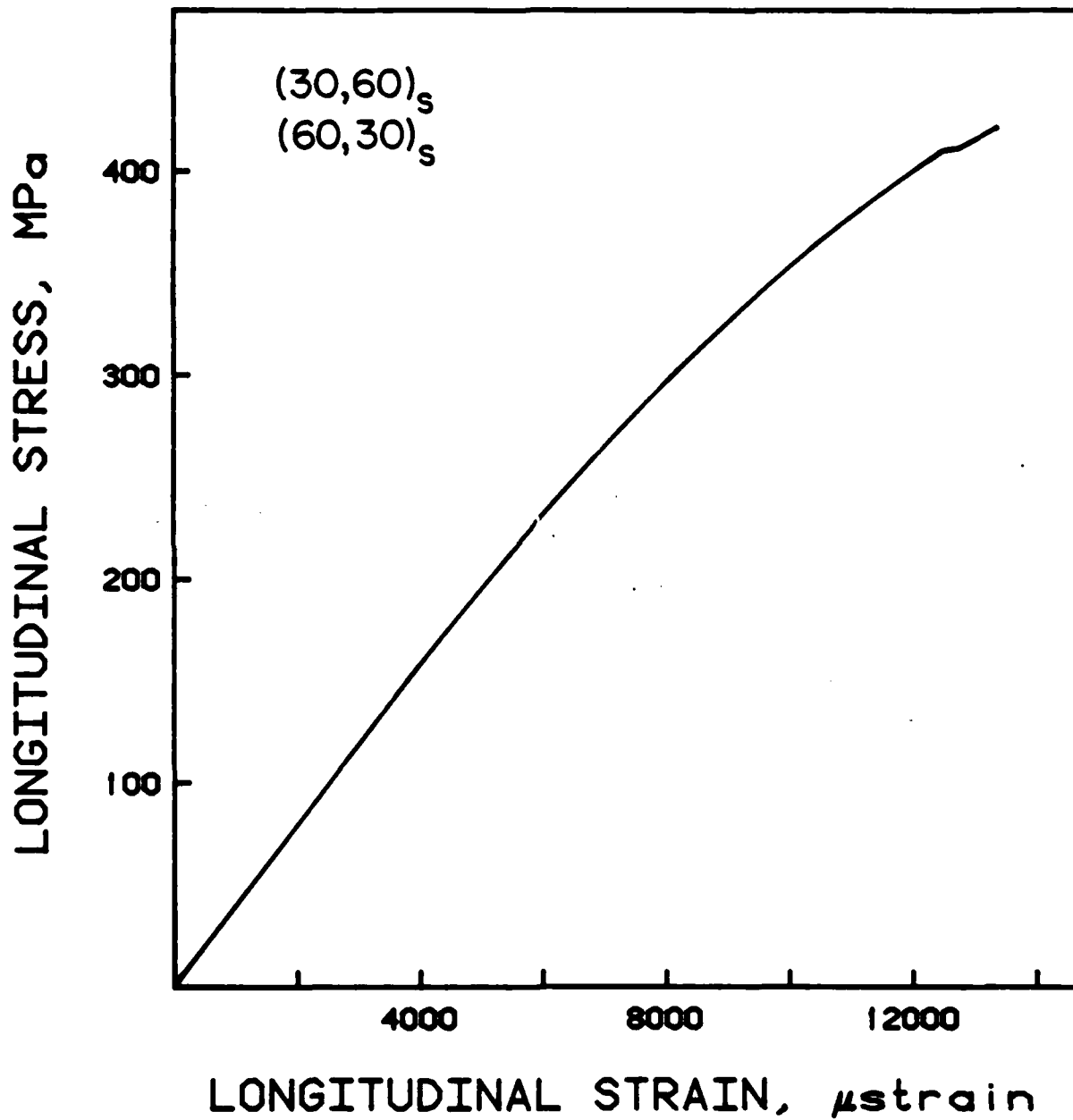


Figure 28 Typical stress-strain behavior of (30,60)<sub>s</sub> and (60,30)<sub>s</sub> unnotched fabric laminates.

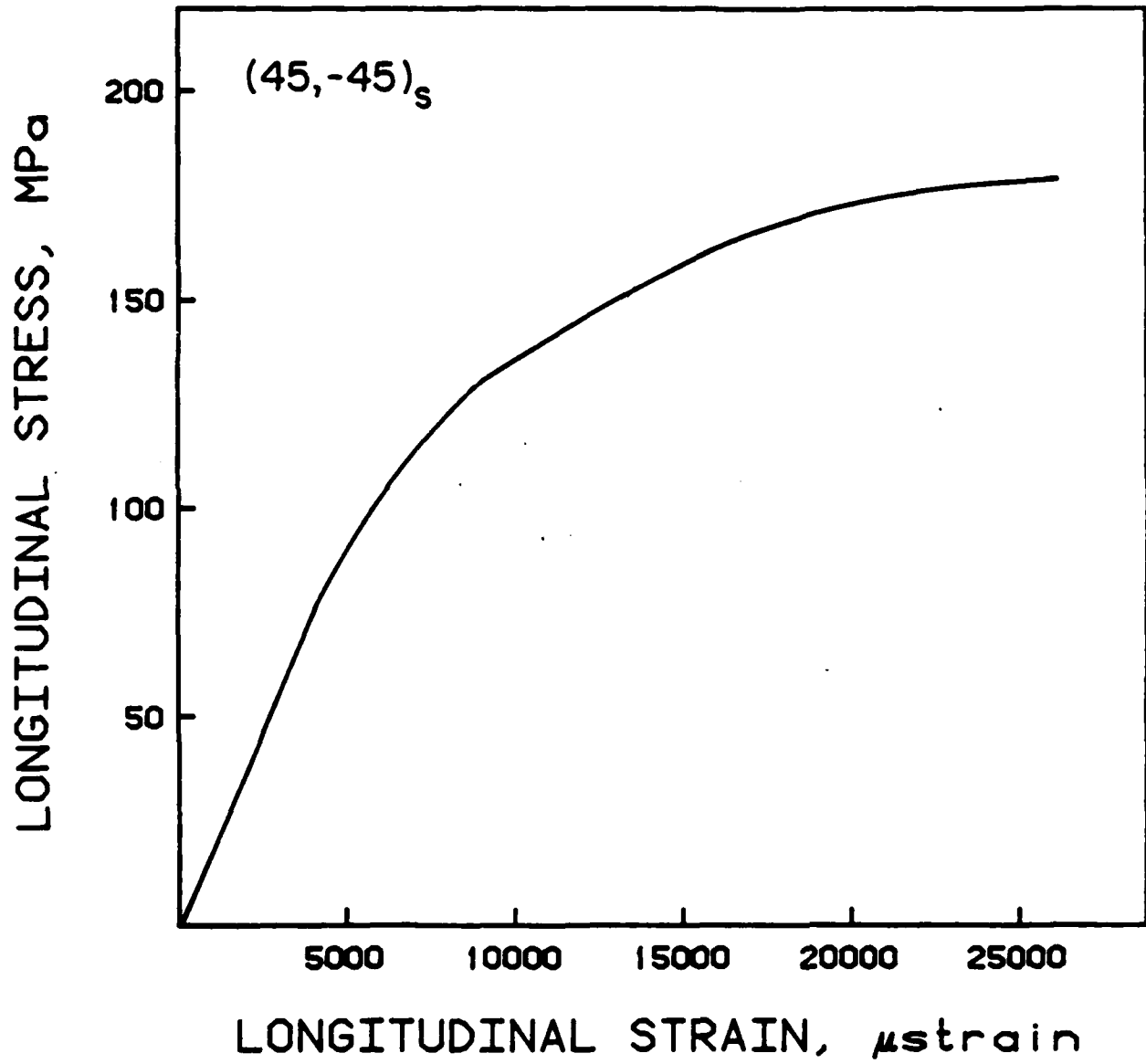


Figure 29 Typical stress-strain behavior of  $(45,-45)_s$  unnotched fabric laminates.

Table 12      Average experimental fracture stresses for  
notched graphite/epoxy fabric laminates

Hole Size [mm]	Laminate				
	(0,90) <sub>s</sub>	(30,60) <sub>s</sub>	(+45,-45) <sub>s</sub>	(60,30) <sub>s</sub>	(90,0) <sub>s</sub>
Unnotched	828 <sup>a</sup> (2.4%) <sup>b</sup>	402 (2.7%)	177 (4.7%)	435 (2.9%)	829 (8.4%)
3.175	684 (3.5%)	405 (3.6%)	194 (3.4%)	437 (1.8%)	686 (4.2%)
6.35	586 (4.2%)	383 (3.0%)	180 (3.4%)	392 (6.3%)	600 (6.2%)
9.525	540 (6.8%)	336 (2.1%)	160 (4.4%)	340 (2.2%)	524 (5.9%)
12.7	499 (7.6%)	290 (1.7%)	132 (6.3%)	293 (3.4%)	497 (6.0%)

<sup>a</sup>Units of stress are MPa.

<sup>b</sup>Numbers in parentheses are coefficients of variation.

The failure stresses of the notched specimens were correlated using the Mar-Lin relation [15,16] of equation 2.1 as explained in section 2.6. Although the form of the material has changed from the unidirectional ply case, the value of  $m$  will not change since it is based on the value of the stress singularity at a crack lying in the matrix at a matrix/fiber interface. Thus, the value depends only on the Poisson's ratios and shear moduli of the matrix and fiber [17] and not on whether they are in unidirectional tape or woven fabric. Thus, the value of 0.28 was again used for  $m$ .

The method for correlating the data described in section 2.6 is again used here. Given that the value of  $m$  is 0.28, values of the composite fracture parameter,  $H_c$ , are calculated for each laminate for each hole size based on the average experimental fracture stress for that hole size. These values, the average  $H_c$  for each laminate type, and the associated coefficients of variation are tabulated in Table 13.

It should be noted that the Mar-Lin relation predicts that failure strength approaches infinity as the notch size approaches zero. It can be seen that the realistic range of applicability of the Mar-Lin relation is that range where the predicted failure stress is less than the unnotched failure stress. Therefore, there must exist some notch size,  $2r^*$ , where the predicted notched failure stress is equal to the unnotched failure stress. It can then be seen that specimens are insensitive to notches smaller than  $2r^*$ . This is illustrated in Figures 30 through 32 by the horizontal line which intersects

Table 13 Experimentally-determined composite fracture parameters for graphite/epoxy fabric laminates

Hole Size [mm]	Laminate				
	(0,90) <sub>s</sub>	(30,60) <sub>s</sub>	(45,-45) <sub>s</sub>	(60,30) <sub>s</sub>	(90,0) <sub>s</sub>
3.175	945 <sup>a</sup>	b	b	b	948
6.35	983	645	302	628	1007
9.525	1015	632	301	612	985
12.7	1017	591	269	575	972
Average	990 (3.4%) <sup>c</sup>	623 (4.5%)	291 (15.4%)	605 (4.5%)	978 (12.5%)

<sup>a</sup>Units of composite fracture parameter are MPa(mm)<sup>0.28</sup>.

<sup>b</sup>Indicates that failure did not occur at the hole.

<sup>c</sup>Numbers in parentheses are coefficients of variation.

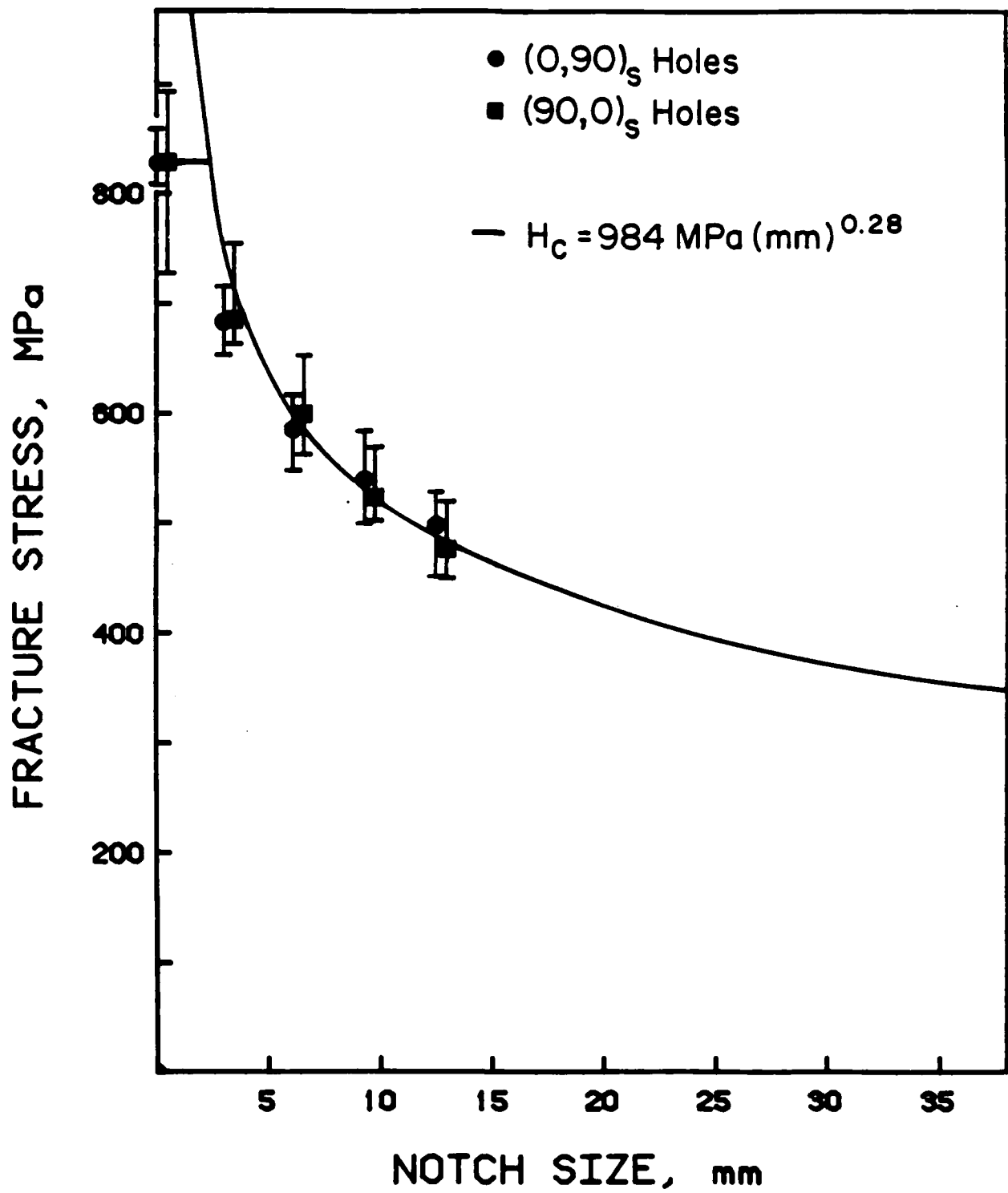


Figure 30

Experimental fracture stresses and theoretical correlation for notched (0,90)<sub>s</sub> and (90,0)<sub>s</sub> fabric laminates.

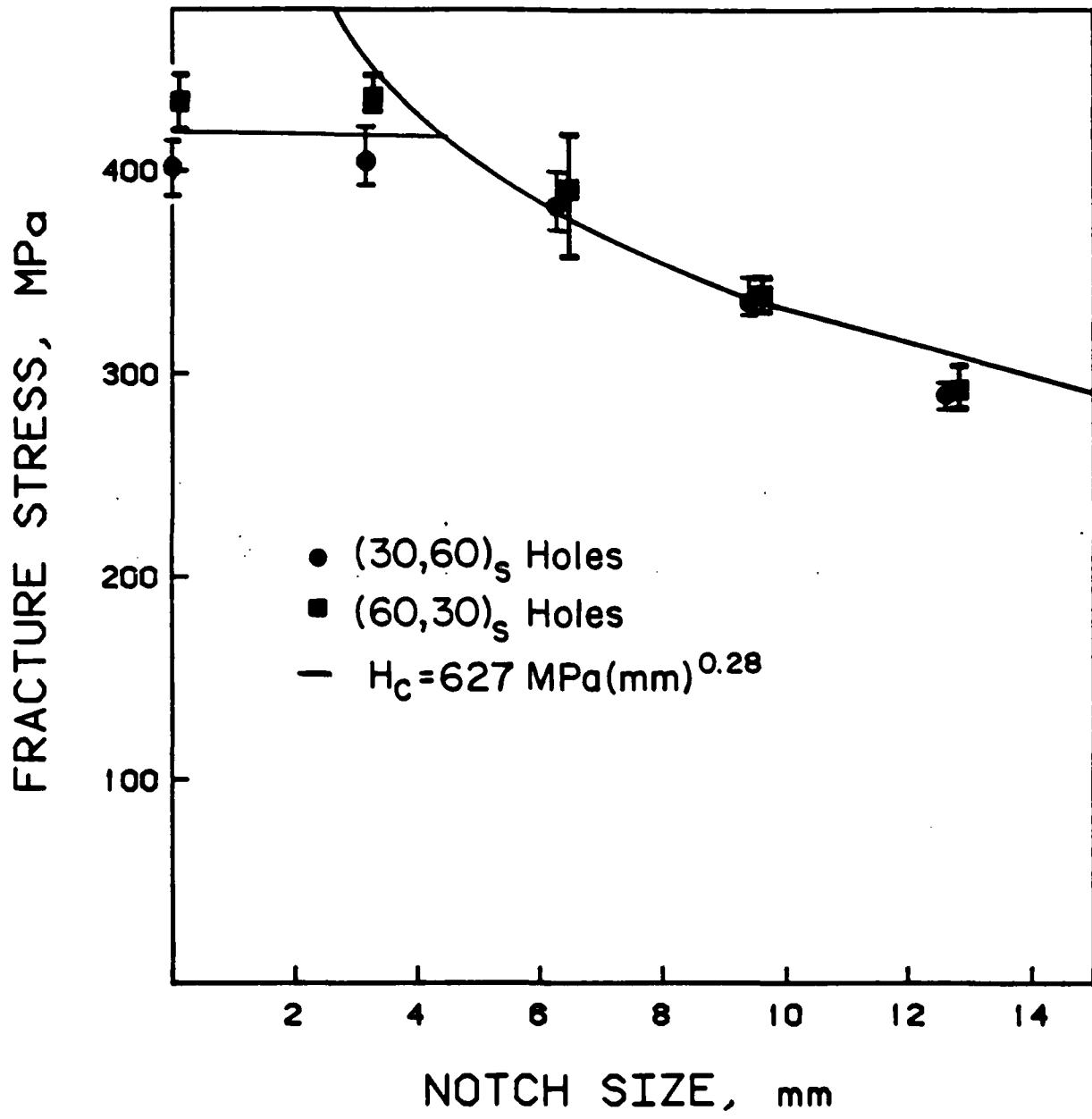


Figure 31

Experimental fracture stresses and theoretical correlation for notched (30,60)<sub>s</sub> and (60,30)<sub>s</sub> fabric laminates.

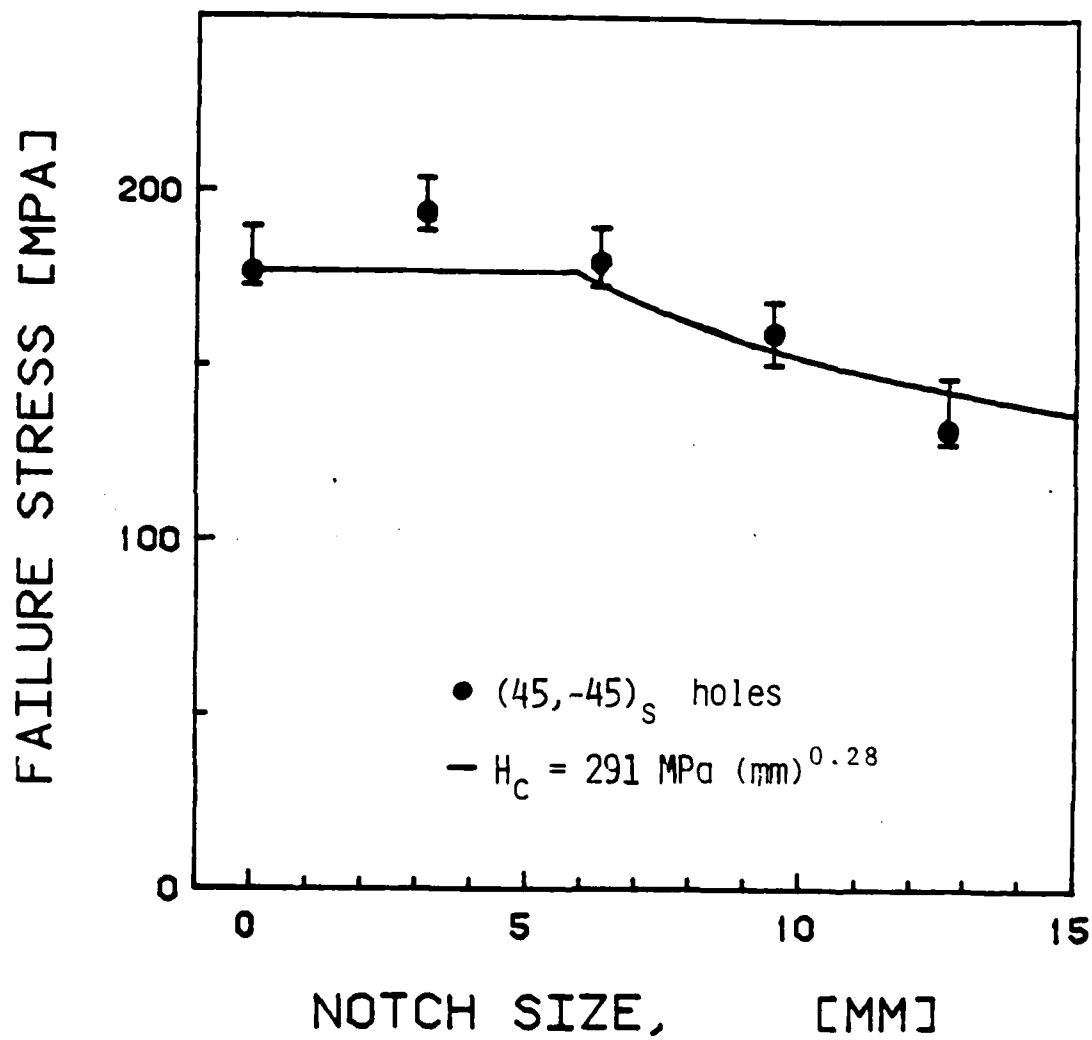


Figure 32 Experimental fracture stresses and theoretical correlation for notched (45,-45)<sub>s</sub> fabric laminates.

the Mar-Lin correlation. These plots are of the experimental fracture data along with the Mar-Lin correlation as previously described. Note that in these plots the value of  $H_c$  has been pooled for the two laminates with similar angular orientations, but different stacking sequences. The results clearly show that for four-ply laminates, reversal of the stacking sequence did not affect either the unnotched or notched failure stresses. This is a result of the cross-ply nature of a fabric ply and shows that there is little difference in behavior between the warp and fill directions.

This work has shown several important points about fabric composite laminates. First, Classical Laminated Plate Theory is a valid tool for describing the elastic properties of fabric composites. Second, the Mar-Lin relation is a useful method for correlating failure stresses of notched fabric composite laminates. Both the Mar-Lin relation and actual data show that the size of flaws to which fabric composite laminates are insensitive is rather large (on the order of a few millimeters). Finally, it can be seen that there is not an overwhelming difference between the warp and fill directions of the fabric, even though the fill fibers are woven around the warp fibers. It is evident that if one considers the warp and fill directions to be equivalent, then a  $(0,90)_s$  laminate is equivalent to a  $(90,0)_s$  laminate and a  $(30,60)_s$  laminate is equivalent to a  $(60,30)_s$  laminate. The difference in the data between those pairs of laminates is, in fact, small enough to be dismissed as experimental scatter.

This work is thoroughly discussed by Chang, Archard, and Brewer in Reference 24.

This work has shown that fracture correlations used for laminates of unidirectional tape can also be used for those made from woven fabric prepreg. Further work is being pursued to examine the similarities and differences in fracture behavior between laminates manufactured from fabric and similar sequences manufactured from unidirectional tape.

#### 2.9 Instabilities and Failure of Graphite/Epoxy Tubes in Compression

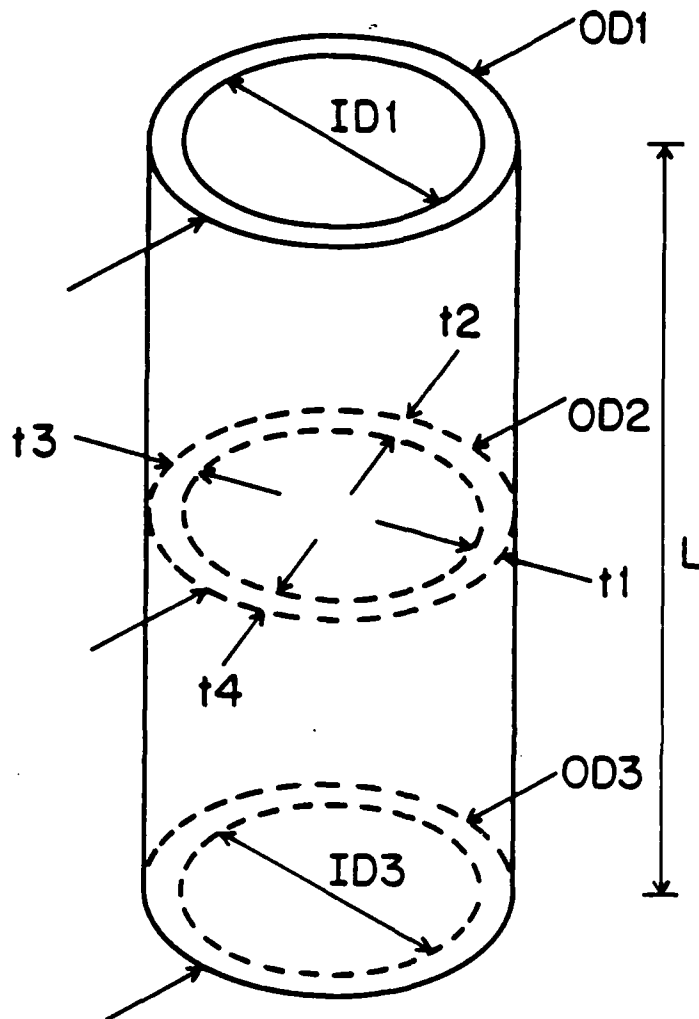
All of the work reported thus far has dealt with the tensile regime. It is just as important, if not more, to look at the behavior, and specifically failure, of composites under compressive loads. Part of the work reported last year [1] looked at the development of a specimen to test relatively thin composite laminates under compression. This involved the use of a supporting jig. The investigation found that the jig developed allowed good measurements of the stress-strain behavior, but could not prevent local buckling later in the test. This prevents the measurement of a fracture load.

A sandwich specimen has been developed and used for cyclic testing of thin laminates (see section 3.1). However, these specimens are relatively expensive to manufacture. It is therefore desirable to develop a means by which to test thin composite laminates under compression.

Thus, an investigation was undertaken to examine the compressive failure behavior of thin graphite/epoxy laminates. In order to increase the resistance of the specimen to global buckling, tube specimens were chosen. This specimen and its geometry are shown in Figure 33. However, the geometry chosen introduced local shell buckling. Upon consideration of preliminary results, it was decided that this was indeed a valid failure mode. Often, the compressive failure of composites is due to local or global instabilities. The buckling may occur on several levels, fiber buckling, sublaminar buckling and delamination, global shell or column buckling, and can lead to fracture of the laminate. Thus the work was pursued with this in mind.

Two different stacking sequences were chosen for this investigation:  $[\pm\theta/0]_s$  and  $[0/\pm\theta]_s$ . All the specimens were manufactured from Hercules AS1/3501-6 graphite/epoxy. The preimpregnated tape was layed up on a rubber mandril with the necessary cure materials as shown in Figure 34. The tubes were then cured on the same mandril using the standard TELAC cure cycle. Special care was taken to produce tubes without any wrinkles due to manufacturing. A piece of perforated brass sheet was used in order to prevent this [25].

The choice of testing program was dynamic, with angles chosen after preliminary results in regions of interest. Unidirectional specimens were used to study the affect of the length to radius ratio. These specimens had varying ratios ranging from two to twelve. The testing program is given in



### NOMINAL TUBE DIMENSIONS:

INNER DIAMETER (I.D.) = 37.7 mm

OUTER DIAMETER (O.D.) = 38.5 mm

THICKNESS (t) = 0.804 mm

LENGTH (L) = 95.3 mm

Figure 33

Physical characteristics of the compressive specimen and measurement locations for inner and outer diameters, thicknesses, and length.

AD-A173 729

FRACTURE LONGEVITY (FATIGUE) DYNAMICS AND  
AEROELASTICITY OF COMPOSITE STR. (U) MASSACHUSETTS INST  
OF TECH CAMBRIDGE TECHNOLOGY LAB FOR ADVAN.

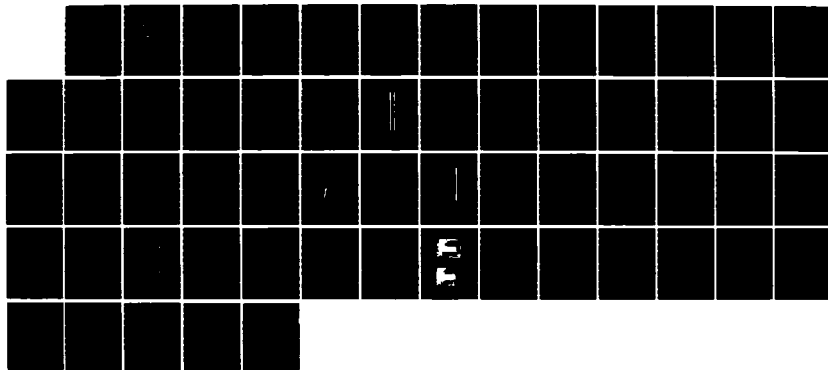
2/2

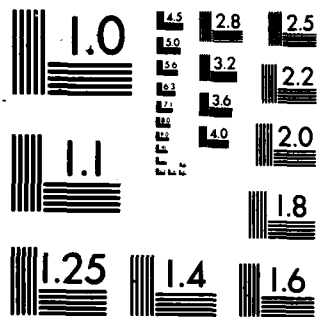
UNCLASSIFIED

P A LAGACE ET AL. 31 DEC 84 TELAC-84-21

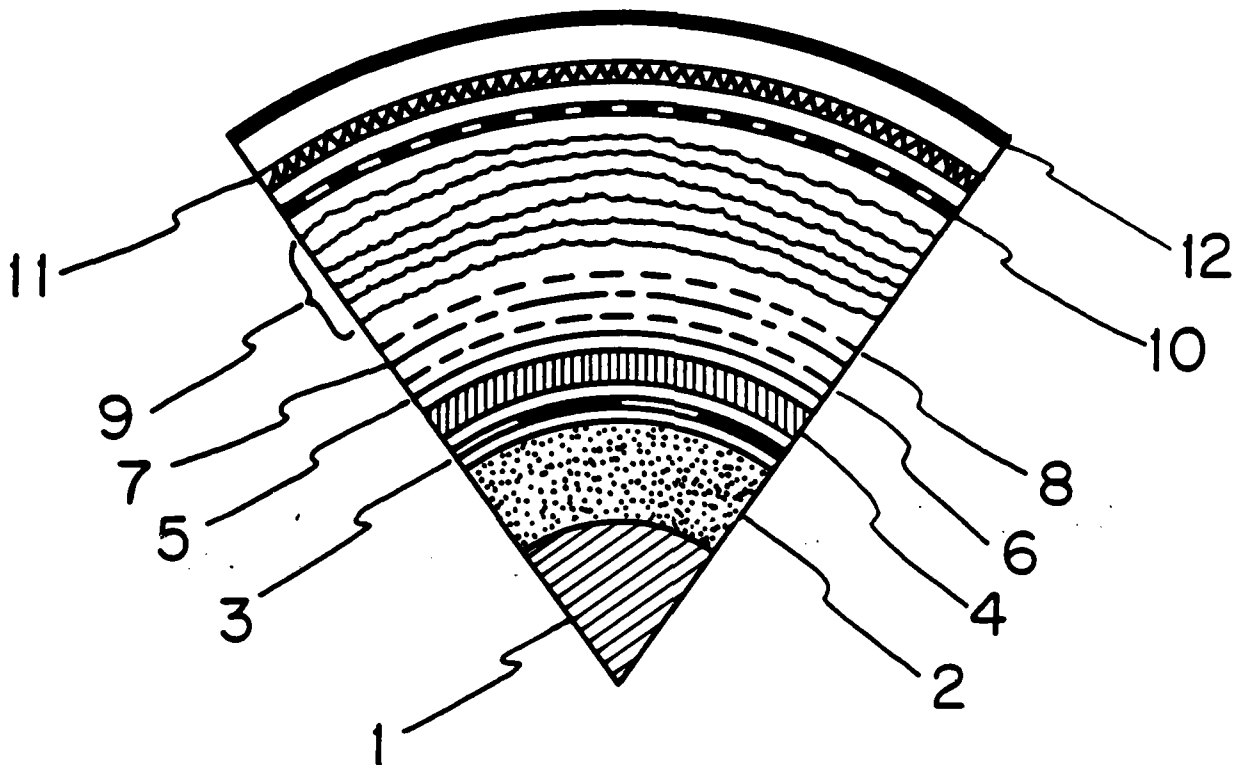
F/G 11/4

NL





MICROCOPY RESOLUTION TEST CHART  
NATIONAL BUREAU OF STANDARDS-1963-A



KEY:

- |                             |                            |
|-----------------------------|----------------------------|
| 1 - aluminum core           | 7 - perforated brass sheet |
| 2 - rubber mandril          | 8 - porous teflon          |
| 3 - non-porous teflon       | 9 - paper bleeder          |
| 4 - graphite/epoxy laminate | 10 - non-porous teflon     |
| 5 - porous teflon           | 11 - air breather          |
|                             | 12 - vacuum bag            |

**Figure 34** Cross-section of manufacturing layup for graphite/epoxy tubes.

Table 14.

All tests were done on an MTS 810 testing machine with the aid of self-aligning platens. Tests were conducted at a constant stroke rate of approximately 0.75 mm per minute to yield a constant stroke rate of 8000 microstrain/minute. Strain data was taken automatically with the use of a PDP-11/34 computer from both longitudinal and transverse gages mounted on each specimen.

The stress-strain behavior of the tubes correlated well with that predicted via Classical Laminated Plate Theory (CLPT). The moduli of the tubes are plotted in Figure 35, and the Poisson's ratios in Figure 36. Scatter was large in some cases indicating poor load introduction, but, in general, the specimen proved to be valid for stress-strain data and produced repeatable results.

Two in-plane fracture and two shell buckling predictions were used to correlate the failure data. The in-plane fracture predictions applied the maximum stress criterion and the stress interaction criterion [5]. Shell buckling predictions were made via an equilibrium approach [26] and via an energy consideration [27]. In general, the in-plane predictions are similar as well as the shell buckling predictions. The stress interaction criterion and the equilibrium method are used in this report for illustrative purposes.

Initially, poor correlation was seen between the data and these predictions as can be seen in Figures 37 and 38. In order to explain this apparent discrepancy, it is necessary to look at

**Table 14**      **Test matrix for six-ply graphite/epoxy tube specimens in compression**

$\theta$	Laminates		
	$[\theta_6]$	$[\pm\theta/0]_s$	$[0/\pm\theta]_s$
$0^\circ$	22 <sup>a</sup>	-	-
$10^\circ$	-	4	4
$20^\circ$	-	4	4
$30^\circ$	-	4	4
$35^\circ$	-	2	2
$40^\circ$	-	2	2
$45^\circ$	-	5	4
$60^\circ$	-	2	2
$90^\circ$	2	2	2

<sup>a</sup> Number indicates number of specimens tested.

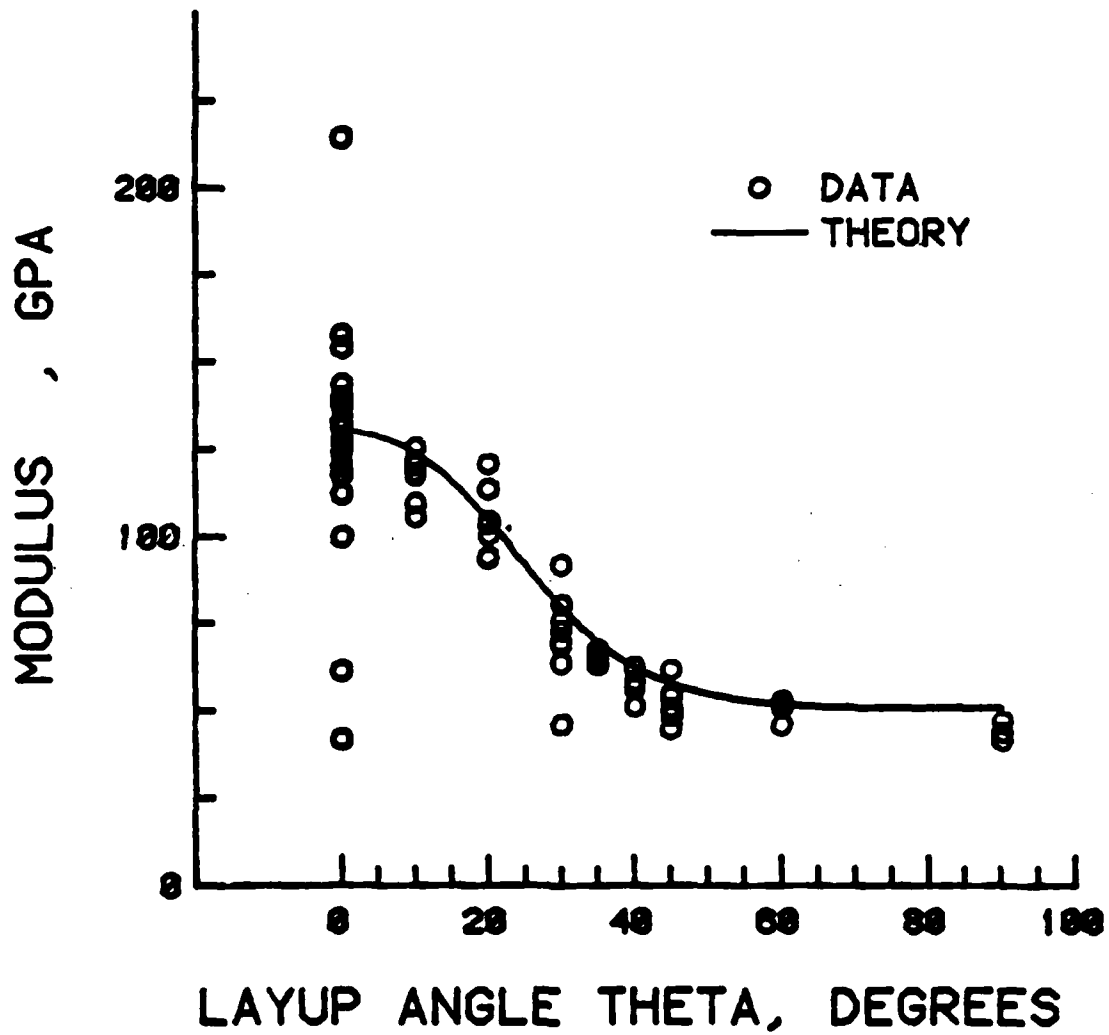


Figure 35 Average compressive experimental and predicted modulus versus lamination angle for  $[\pm\theta/0]_s$  and  $[0/\pm\theta]_s$  tube specimens.

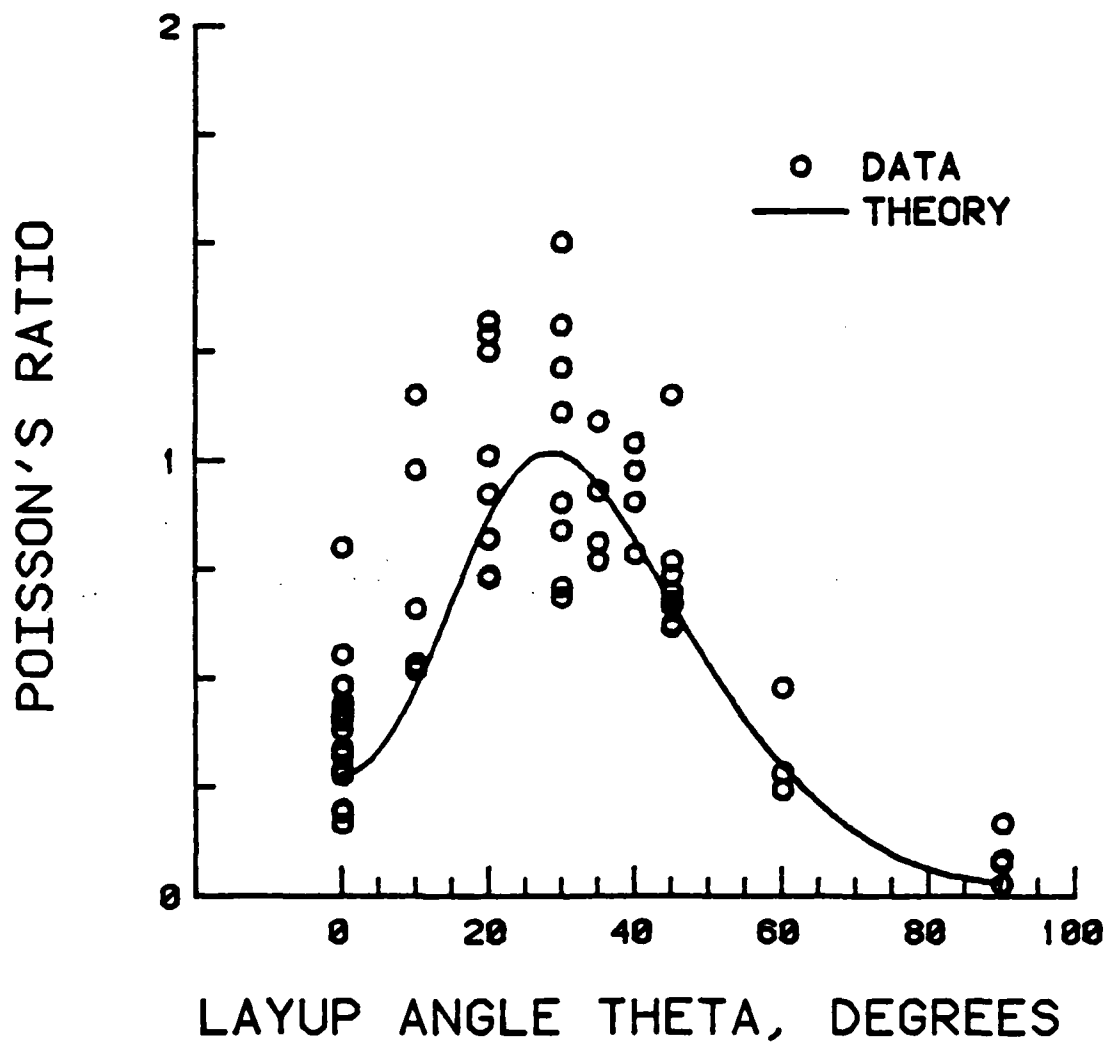


Figure 36

Experimental and predicted Poisson's ratio versus lamination angle for  $[\pm\theta/0]_s$  and  $[0/\pm\theta]_s$  tube specimens.

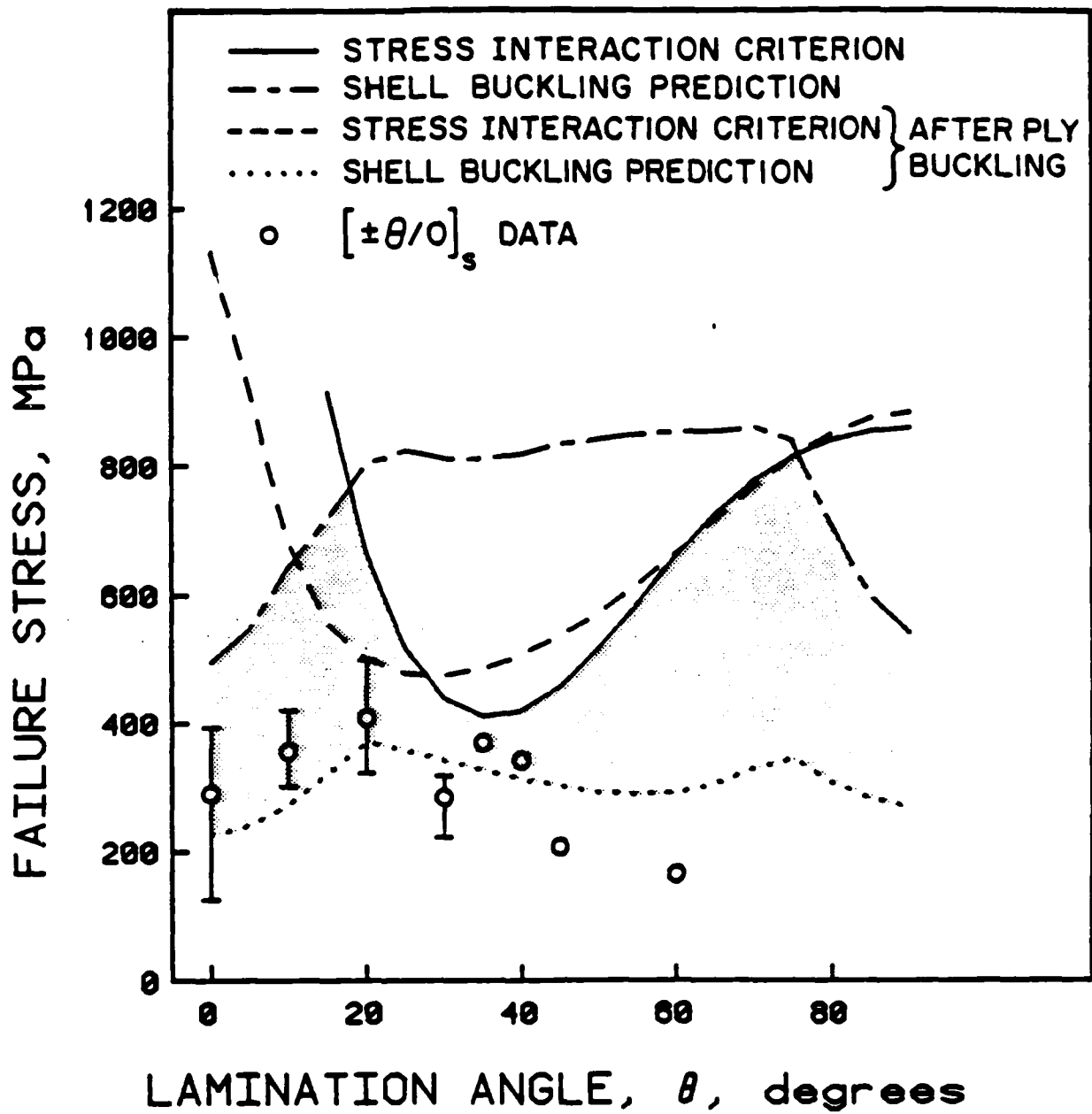


Figure 37

Experimental failure stresses and theoretical correlations (and feasible region) for  $[\pm\theta/0]_s$  tube specimens.

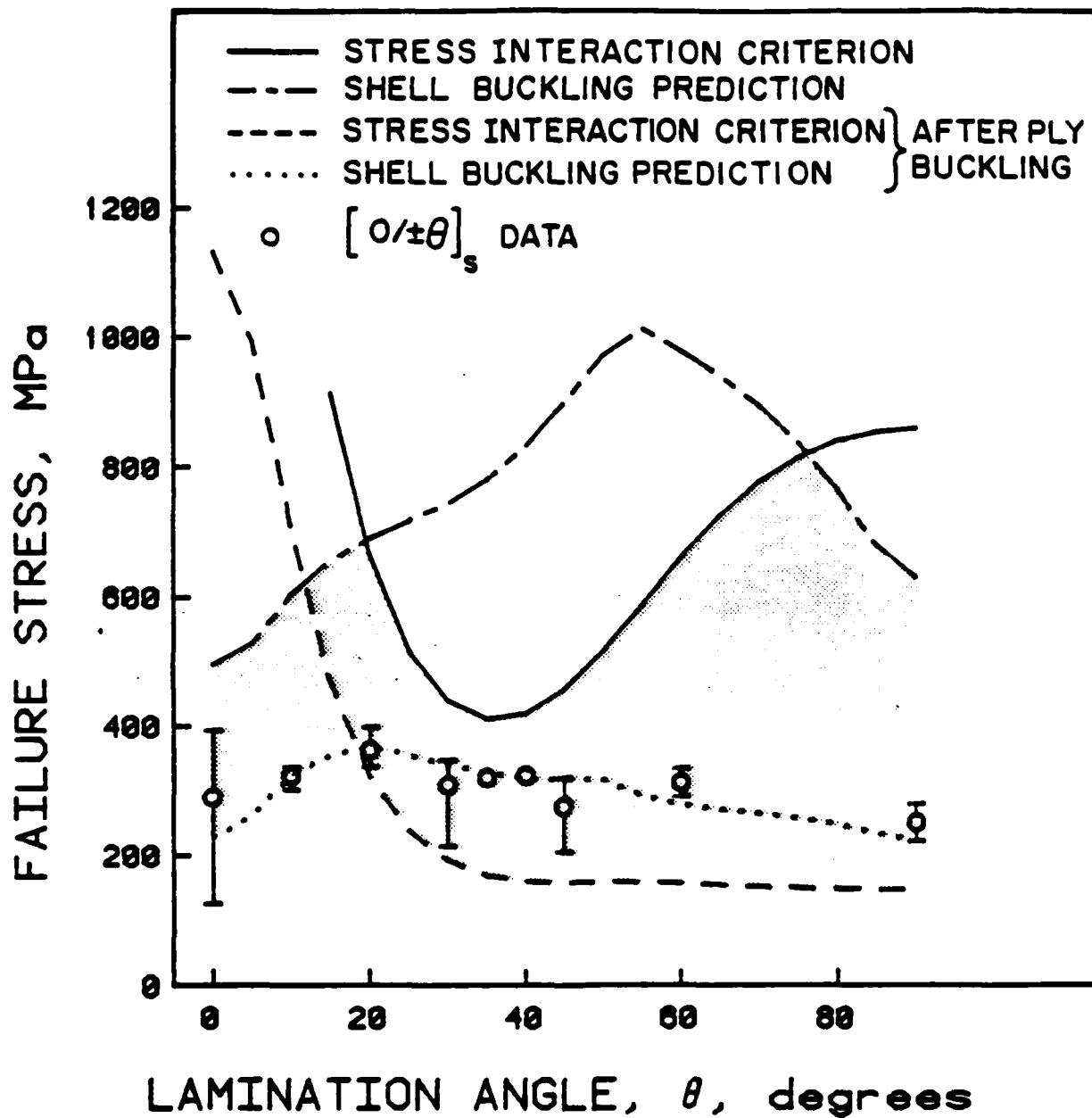


Figure 38

Experimental failure stresses and theoretical correlations (and feasible region) for  $[0/\pm\theta]_s$  tube specimens.

the failure types. The valid failure types of the tubes can be grouped into four categories. The first two failure types involve in-plane fracture as the predominant mode. The first type is fracture which was predominantly perpendicular to the applied load. The second type shows cracks which run in the matrix parallel to the fibers in the top  $\theta$  ply and thus fracture fibers along this same crack angle in the associated  $-\theta$  and  $0^\circ$  plies. Two types of failure involve local instabilities as the predominant mode. The third type had shell buckling in part of or totally around the circumference of the tube. The fourth type, otherwise denoted as ply buckling, was observed when individual plies delaminated and buckled away from the remaining intact plies. A fifth type of failure was observed as well. It involved damage to the end of the tube such as brooming and thus is not valid. The failure stress and failure types are given in Table 15. The failure types are numbered according to the key: 1) in-plane fracture, 2) in-plane splitting, 3) shell buckling, and 4) ply buckling.

It is this fourth type of failure, which is not accounted for by any of the previous predictions, that can explain the apparent discrepancy between the experimental data and predictions. This failure type involved the outermost ply to buckle and delaminate away from the remaining "intact" plies and occurred prior to and at final failure of some specimens.

A model was proposed to incorporate this phenomenon of ply or sublamine buckling. The laminate is modeled as a series of plates constrained by elastic springs, that is the interply

Table 15 Experimental failure stresses and modes for  $[\pm\theta/0]_s$  and  $[0/\pm\theta]_s$  tubular specimens under compressive load

$\theta$	$[\pm\theta/0]_s$				$[0/\pm\theta]_s$			
	Number of tests excluded due to end failure	Failure stress, MPa	C.V.	Failure Type(s)	Number of tests excluded due to end failure	Failure stress, MPa	C.V.	Failure Type(s)
10°	1	356	16.8%	3	0	324	4.8%	1,3
20°	1	409	21.6%	1,2,3	0	363	7.2%	3,4
30°	1	285	18.9%	2	0	310	20.5%	1,2,3,4
35°	1	370	a	2	1	321	a	2,4
40°	1	343	a	1,2	0	324	2.0%	2,4
45°	4	207	a	2	1	276	22.4%	1,4
60°	1	165	a	1	0	313	10.1%	1,4
90°	2	b	b	b	0	251	16.2%	1,4

<sup>a</sup> No C.V. reported since only one specimen failed not due to end failure.

<sup>b</sup> No data reported since both specimens failed due to end failure.

matrix layer. The outermost plies, being least constrained, are most likely to buckle. Moreover, initial geometric imperfections, material flaws, and load eccentricities will cause out-of-plane deflections from the onset of loading. When the sublamine buckles, stresses in the interply matrix region rise leading to failure of the matrix and subsequent delamination. Furthermore, when the sublamine buckles, the load is redistributed throughout the laminate, with the "intact" plies carrying more load. This increase in stress can lead to "premature" failure of the entire laminate. The extreme of this model is that the buckled plies carry no load.

If the failure predictions (both in-plane fracture and shell buckling) are performed on the laminate with the outer plies effectively removed, a lower bound to the region where failure might occur due to partial unloading of the outer plies can be found. Shown in Figures 37 and 38 are the data plotted against the "feasible region" based on this ply buckling model. The feasible region at a given lamination angle has an upper bound determined by the lower of the fracture and shell buckling predictions for the intact laminate and has a lower bound determined by the lower of the fracture and shell buckling predictions based on the ply buckling model with the outermost plies, both inner and outer radius, "effectively" removed.

Expected failure types can be deduced from the boundaries of the feasible region and the intersections of the various failure criteria. For all values of lamination angle, the lower boundary of the feasible region for the  $[\pm\theta/0]_s$  specimens is

determined by shell buckling of the remaining intact plies after ply buckling. The upper boundary of the region for these specimens, however, is defined by shell buckling of the entire laminate for  $\theta$  less than approximately  $20^\circ$  at which point the mode changes and the upper boundary is defined by in-plane fracture of the entire laminate. For values of lamination angle between  $30^\circ$  and  $55^\circ$ , the stress interaction criterion indicates that the loss of load-carrying capability due to ply buckling does not degrade (but actually slightly increases) the in-plane fracture strength of the laminate. For large values of  $\theta$ , greater than  $75^\circ$ , shell buckling of the entire laminate again defines the upper boundary.

The experimental failure stresses for the  $[\pm\theta/0]_s$  specimens generally lie within the feasible region as can be seen in Figure 37. Shell buckling was the failure mode for  $\theta$  equal to  $10^\circ$  as predicted. For the  $[\pm 20/0]_s$  specimens, a mixture of failure modes occurs: shell buckling and in-plane fracture (this includes both failure types 1 and 2). The upper bound of the feasible region suggests a transition of failure types should occur in this vicinity. For all larger values of lamination angle,  $30^\circ$ ,  $35^\circ$ ,  $40^\circ$ ,  $45^\circ$ , and  $60^\circ$ , the failure is due to in-plane fracture as suggested by the prediction. The data for the latter two angles,  $45^\circ$  and  $60^\circ$ , lie slightly below the feasible region. This might be attributed to irregularities in the tubes.

The feasible region for the  $[0/\pm\theta]_s$  specimens, as defined in Figure 38, is slightly more complex. In this case, the lower

bound is determined by shell buckling after outer ply buckling only for  $\theta$  less than  $20^\circ$ . For larger values of  $\theta$ , in-plane fracture after the  $0^\circ$  plies have buckled away becomes the lower bound. As in the  $[\pm\theta/0]_s$  case, shell buckling of the entire laminate defines the upper bound for small values of lamination angle ( $\theta$  less than  $20^\circ$ ) and for large values ( $\theta$  greater than  $75^\circ$ ). For all other values of  $\theta$ , in-plane fracture of the entire laminate is the upperbound.

For the  $[0/\pm\theta]_s$  specimens, the experimental failure stresses fall within the feasible region and very near the lower boundary. All specimens exhibited ply buckling except for the  $[0/\pm10]_s$  specimens where a mixture of shell buckling and in-plane fracture occurred. For  $\theta$  equal to  $20^\circ$ , shell buckling occurred after ply buckling as predicted. Several failure types occurred in the  $[0/\pm30]_s$  specimens. This is in the vicinity of the transition of failure types in the feasible region. For all larger values of lamination angle,  $35^\circ$ ,  $40^\circ$ ,  $45^\circ$ ,  $60^\circ$ , and  $90^\circ$ , in-plane failure (either by fracture or splitting) follows ply buckling as predicted using the ply buckling model. This was especially noticable as  $\theta$  increased, with gross delaminations of the outer  $0^\circ$  plies occurring in the  $[0/90_2]_s$  specimens prior to final failure.

This work is reported in detail by Vizzini [25] and Vizzini and Lagace [28]. Typical photographs of the various failure modes are also provided therein. Further research is currently being conducted on this subject. Uniaxial sandwich column specimens (see section 3.1) are being used instead of tubes in

order to isolate in-plane failure and ply buckling from shell buckling.

### 3. LONGEVITY (FATIGUE)

The work at TELAC on the longevity of composite materials has been directed toward the study of damage modes and the accumulation of damage with repeated loading. The terminology "fatigue" and its connotations of S-N curves are not readily applicable to composites and thus, as suggested by Mar [29], the word "longevity" is purposefully used instead of "fatigue". The work to date has examined the growth of damage around notches under cyclic load. A notch is any macroscopic flaw purposefully introduced into the laminates. In these studies, the notch types considered have been holes and slits. Both tension-tension and compression-compression cycling have been investigated.

#### 3.1 The Effect Of Ply Thickness on Longitudinal Splitting and Delamination in Graphite/Epoxy under Compressive Cyclic Load

Previous work at TELAC and by other investigators has shown that a predominant mode of damage which occurs under cyclic load, but especially when this is in the compressive regime, is interply failure known as delamination. The previous work conducted at TELAC [1,30,31] concentrated on notched [ $\pm 45/0$ ]<sub>s</sub> graphite/epoxy specimens loaded in compression-compression cycling. These investigators reported delamination as an important damage mode, but also noted that the damage patterns varied with the applied loading and the notch size.

It is well known that the cause of delamination is the stresses which arise between the plies of a laminate. These stresses are known as interlaminar stresses. As described in sections 2.2 and 2.5, the thickness of a ply will have an effect on the magnitude of the interlaminar stresses in a laminate and thus can (again, see section 2.5) change the failure stress of a laminate. It would therefore seem logical that the "effective ply thickness" will also have an effect on the development of delamination damage under cyclic loading.

Thus, the main thrust of the current investigation is to examine the effect which ply thickness has on the development and propagation of damage (with an eye towards delamination) in composite laminates subjected to compression-compression cyclic loading. The impact of ply thickness on the residual tensile strength of these damaged laminates is also investigated.

The  $[\pm 45/0]_s$  family of laminates was again chosen for investigation due to the facts mentioned previously and also due to the fact that other authors have observed differing damage modes for this type of laminate. Investigators (e.g. [32]) who have looked at a slight variation of this stacking sequence, that is  $[0/\pm 45]_s$ , have observed axial cracks, known as splits, develop from the notch and then subsequent delamination. This splitting is similar to that observed in pure unidirectional specimens as reported in last year's report [1,33]. These authors (e.g. [32]) have also observed that the residual tensile strength increases after this damage occurs. Therefore, this investigation also looks into the tensile residual strength

of the specimens after they have been damaged by exposure to cyclic compressive load, and the effect that ply thickness has on this residual strength via the damage which is incurred.

The "effective ply thickness" of the  $[\pm 45_n/0_n]_s$  laminates was varied from 0.134 mm to 0.268 mm to 0.402 mm by varying  $n$  from 1 to 2 to 3 in the same manner described in section 2.5 and illustrated in Figure 19. Both static tests and compressive tests were conducted on the three laminates. Static tests were performed in order to experimentally obtain longitudinal modulus and the fracture stress in order to ascertain whether the effective ply thickness has an effect on the static compressive fracture. Each of the three laminates were cycled at three maximum stress levels at a stress ratio of 10. The stress levels varied for the three different laminates and were, in part, dependent upon results obtained from previous tests. A total of 56 specimens were tested in this program, 21 in static compression and 35 under compression-compression cyclic loading. The entire test matrix is shown in Table 16. All face sheets had a 6.35 mm hole drilled in their center.

The specimen configuration used in testing is especially important in compression. The specimen and any associated supporting structure must minimize stresses due to specimen bending but not restrict failure modes of the material from developing due to local constraints. A number of jigs have been developed and used with varying success (e.g. [1]). In this program, it was necessary to not only load the specimen in compression but also to closely monitor damage development

Table 16 Experimental test program for compression-compression cyclic loading of notched  $[\pm 45_n/0_n]_s$  graphite/epoxy specimens

TEST TYPE	PEAK COMPRESSIVE STRESS, MPa	LAMINATES <sup>a</sup>		
		$[\pm 45/0]_s$	$[\pm 45_2/0_2]_s$	$[\pm 45_3/0_3]_s$
MONOTONIC TO FAILURE	FAILURE STRESS	$9^b$	8	5
CYCLIC <sup>c</sup>	320	2	-	-
CYCLIC	287	12	8	-
CYCLIC	265	-	4	1
CYCLIC	253	2	-	-
CYCLIC	243	-	2	1
CYCLIC	221	-	-	3

<sup>a</sup> ALL SPECIMENS HAVE 6.35 mm DIAMETER HOLES.

<sup>b</sup> NUMBER INDICATES NUMBER OF SPECIMENS TESTED.

<sup>c</sup> ALL CYCLIC TESTS ARE COMPRESSION-COMPRESSION WITH A STRESS RATIO  $(\sigma_{\min}/\sigma_{\max})$  OF 10 RUN AT 7 HZ.

around the hole. Thus, any antibuckling jig would need to leave the areas around the hole free for nondestructive inspection. The cylindrical specimen discussed in section 2.9 did not yield satisfactory results, so another specimen had to be sought. Thin composite laminates, such as those investigated herein, have been successfully tested using a sandwich beam under four-point bending [34]. However, this bending introduces local stress concentrations in the material and also is not conducive to certain types of nondestructive investigation techniques (such as the moire method).

For this work, the basic sandwich specimen was adopted but was tested as an axial column. A schematic of the specimen is shown in Figure 39. The specimen consists of two 50 mm face sheets of AS1/3501-6 graphite/epoxy of the same laminate configuration.

The graphite/epoxy face sheets were made in the standard way including the drilling of 6.35 mm diameter holes. These completed graphite/epoxy face sheets were bonded onto a honeycomb support structure using film adhesive FM-123-2 (from American Cyanamid). This process was conducted in an autoclave at 0.24 MPa and 107°C for two hours. The core consisted of two different types of aluminum honeycomb. The central part of the core in the test section had a low density ( $72 \text{ kg/m}^3$ ) aluminum honeycomb while the end section, 90 mm in length, had a high density ( $354 \text{ kg/m}^3$ ) aluminum honeycomb. These three individual pieces of honeycomb were bonded end-to-end with a room temperature cure epoxy before final bonding of the

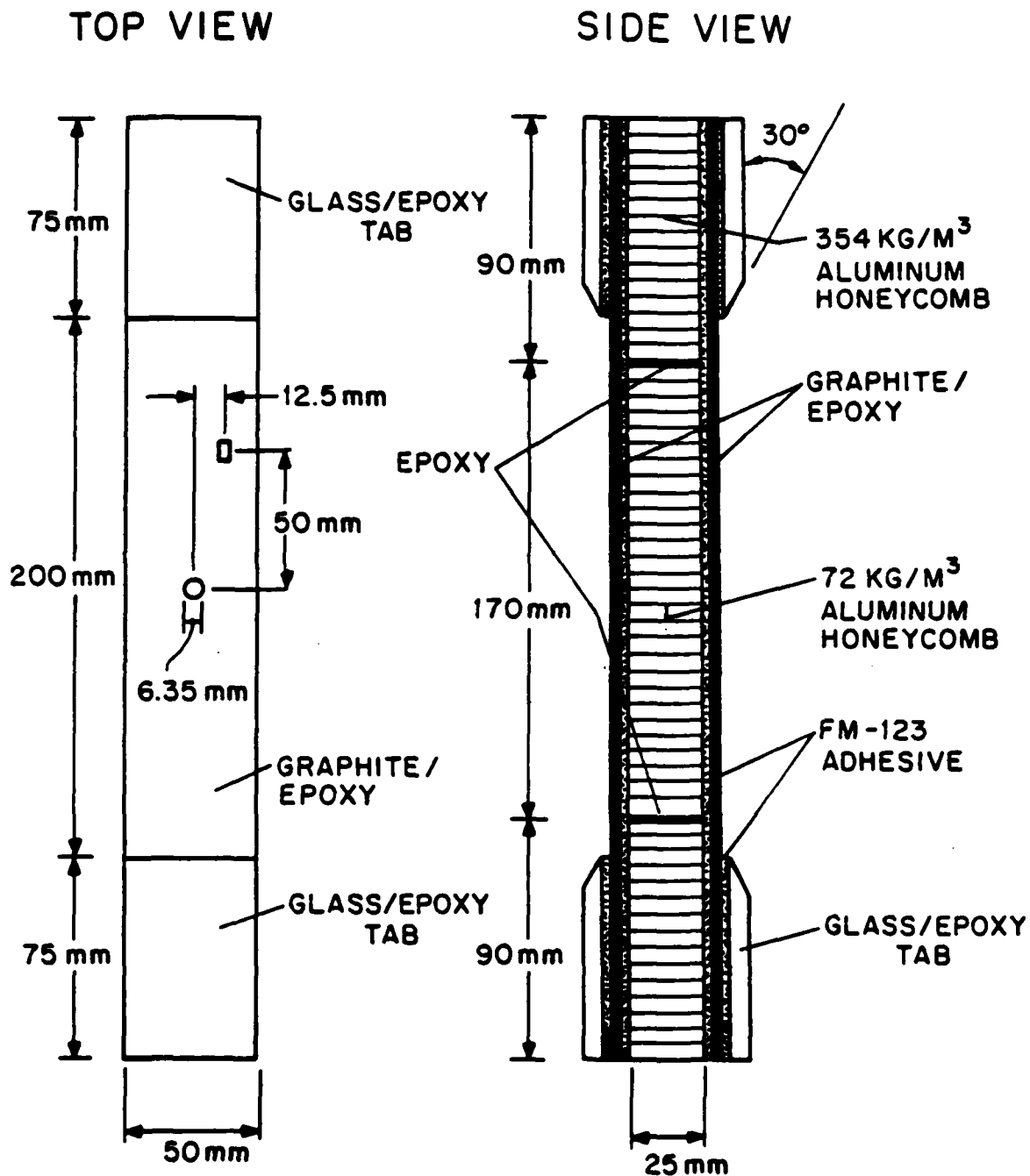


Figure 39

Physical characteristics of the sandwich specimen.

graphite/epoxy face sheets. The high density aluminum honeycomb was chosen for the ends so that there was sufficient support to prevent crushing of the core when the specimens were gripped by the hydraulic grips of the testing machine. The low density honeycomb was chosen for the test section so as to provide minimal restriction of the face sheets. A secondary bond was performed to place glass/epoxy loading tabs at the ends of the specimen just as is done for the standard tensile specimen (see section 2.1). The plies were of the same  $0^{\circ}/90^{\circ}$  construction with the same thickness ratio maintained. The loading tabs were 75 mm in length which is slightly less than the area of high density honeycomb. This is done to minimize the local rotation and stress concentration which would occur if the low to high density honeycomb interface coincided with the tab end. Longitudinal strain gages were bonded onto all specimens which were tested in static compression to obtain data for determining longitudinal modulus.

A test program was conducted by Nolet [35] to check the validity of this specimen. Further work is currently being conducted at TELAC to quantify the behavior of this specimen with the goal of proposing this specimen as a standard for compression testing.

All testing was accomplished on an MTS 810 Material Test System with the aid of hydraulic grips. The static specimens were loaded at a constant stroke rate of 0.33 mm/minute yielding an approximate strain rate of 1800 microstrain/minute. Cyclic testing was accomplished under load control with sinusoidal

loading at a frequency of 7 Hz. A constant stress ratio of 10 (minimum stress/maximum stress) was used for all tests.

Delamination growth was monitored during each cyclic test using one of two nondestructive inspection (NDI) methods on both sides of the test specimen. This yielded two sets of data for each specimen tested. The two NDI methods used are out-of-plane moire interferometry and pulse-echo ultrasound.

Moire out-of-plane interferometry has been successfully used to detect damage in graphite/epoxy laminates under compression-compression loading [36]. A similar setup to that used in Reference 36 was utilized here. This setup allowed detection of an out-of-plane displacement of 0.25 mm. Moire photographs were taken automatically at a present frequency of 5000 cycles without halting the test. However, the delaminations tended to grow quickly once initiated. When the growth rate of the delamination exceeded approximately 10 mm per 5000 cycles, the frequency of picture taking was increased. This damage size is defined as the maximum linear distance of the damage area in any direction.

The moire interferometry was used for all the cyclic tests of the  $[\pm 45/0]_s$  specimens and the first five tests of the  $[\pm 45_2/0_2]_s$  specimens. In these latter five tests, it was discovered that the out-of-plane deformation was insufficient to be detected by the moire setup although a delamination did exist. This is due to the delaminated region being thicker than in the previous laminate and the local buckling causing a smaller out-of-plane deformation. For the remainder of these

specimens and all of the  $[\pm 45_3/0_3]_s$  laminates, delamination was monitored using the pulse-echo ultrasound technique. This inspection was accomplished with a Nova-Scope 2000 Digital Pulse-Echo Ultrasonic Thickness Gage. The tests were stopped at 50 to 5000 cycle intervals to allow for manual inspection of the two face sheets. The frequency of inspection was chosen to ensure that the damage would not grow more than 10 mm in any direction between inspection intervals. Prior to the onset of delamination, the laminate was inspected at least every 1000 cycles. A ruler was used to measure the length of the delamination as indicated by the ultrasonic technique, in terms of the maximum straight-line distance from the hole edge to the edge of the delamination as illustrated in Figure 40.

All cyclic tests were stopped when either failure occurred or damage grew to a size at which it was felt that failure would occur before the next inspection cycle. It was desirable to prevent failure of damaged cyclic specimens so that tensile residual strength tests could be run.

The average compressive longitudinal modulus and fracture stresses for the static compressive tests are presented in Table 17. The measured longitudinal modulus agrees with the predicted modulus of 57.7 GPa using Classical Laminated Plate Theory and the basic ply data of Table 3. Additionally, a typical stress-strain plot is in Figure 41 which illustrates some softening near the test end (approximately a 10% reduction in tangent modulus). The most important result of the static tests is that the fracture stress is clearly independent of ply

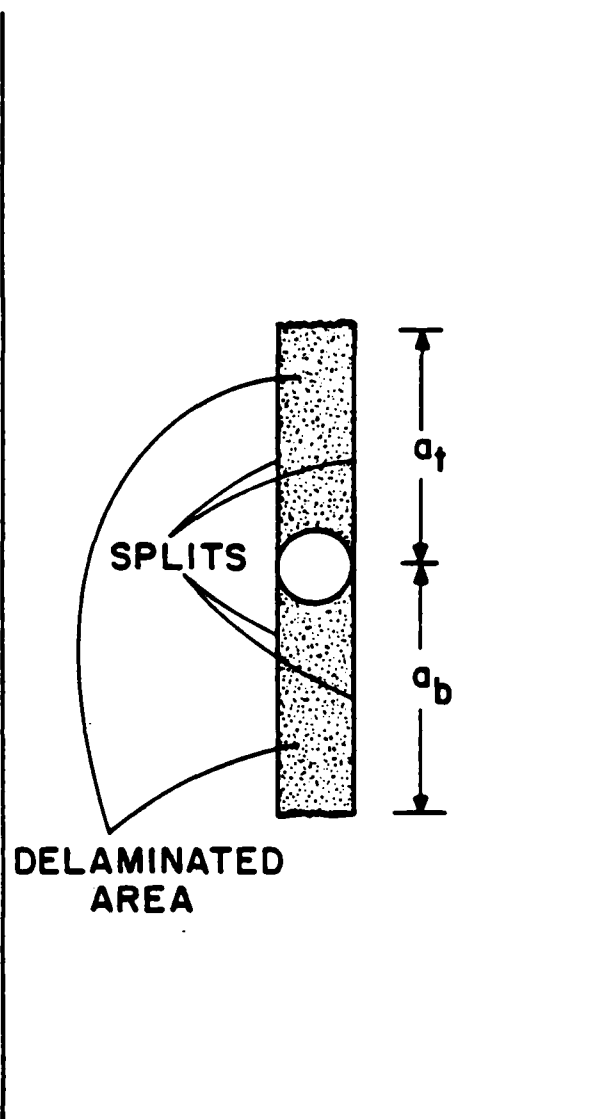


Figure 40      Definition of longitudinal delamination length.

Table 17      Results of compressive monotonic to failure tests of  $[\pm 45_n/0_n]_s$  graphite/epoxy specimens

LAMINATE	LONGITUDINAL MODULI		FRACTURE STRESSES	
	$E_L$ , GPa	C.V.	$\sigma_F$ , MPa	C.V.
$[\pm 45/0]_s$	56.3	4.4%	423	9.1%
$[\pm 45_2/0_2]_s$	57.4	4.1%	421	7.7%
$[\pm 45_3/0_3]_s$	57.0	5.8%	429	8.4%

<sup>a</sup> ALL SPECIMENS HAVE 6.35 mm DIAMETER HOLES.

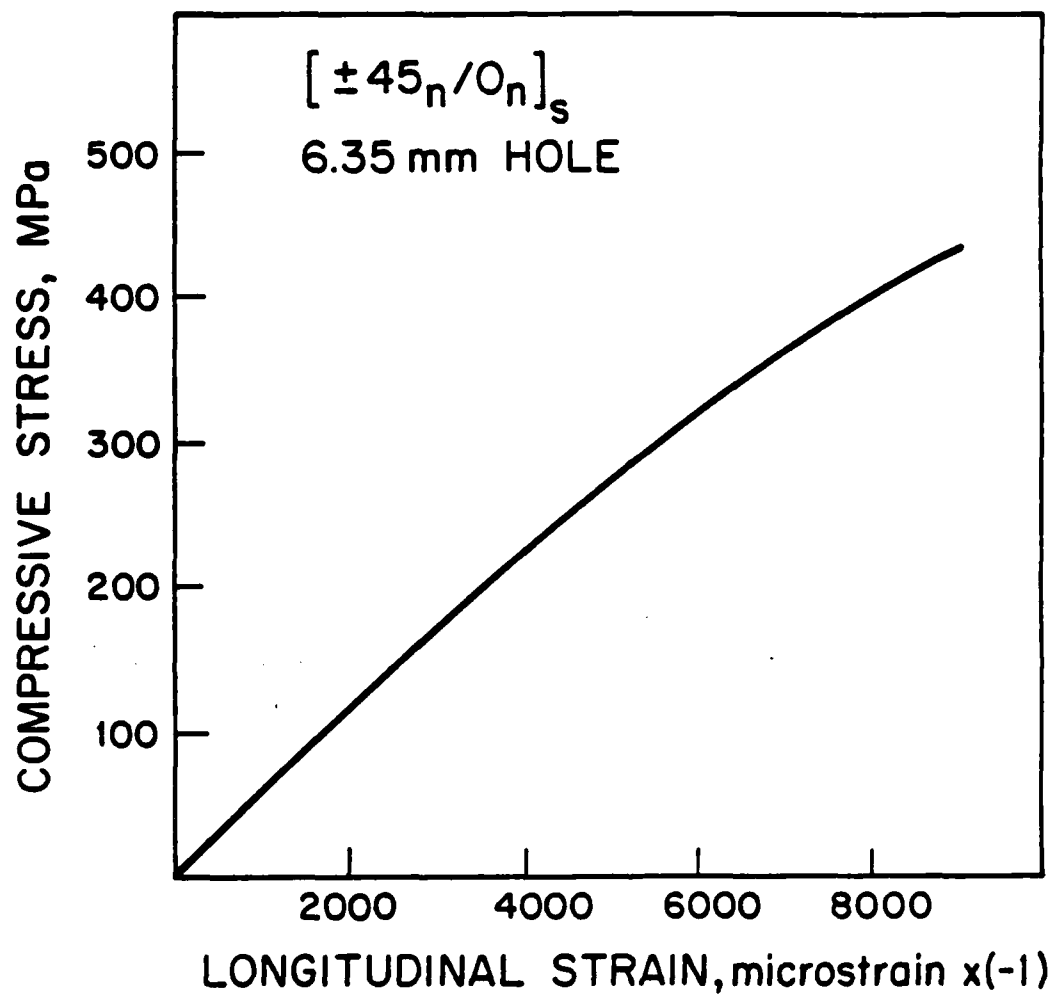


Figure 41 Typical compressive stress-strain behavior of  $[\pm 45_n/0_n]_s$  laminate with a 6.35 mm hole.

thickness. This indicates that the static compressive fracture is not a result of interlaminar stresses but is an in-plane phenomenon. This is confirmed by observations of the postmortem failure mode which shows a relatively "clean" fracture through the hole nearly perpendicular to the applied load. It is important to point out that the failure stress reported for these specimens is actually the failure stress of the weaker of the two face sheets of the specimen. When one face sheet fails, this induces gross bending resulting in failure of the remaining graphite/epoxy face. The average fracture stress will thus be slightly lower than if tests were conducted on the individual face sheets since the higher fracture stress of the stronger face sheet will not be attained.

Three distinct damage modes were observed in the cyclic tests. The first type of damage occurred only in the  $[\pm 45/0]_s$  laminates at generally high stress levels. This damage mode is characterized by rapid growth perpendicular to the load direction which caused failure of the specimen within only a few cycles and was difficult to record through the moire setup since the damage grew to failure in only a few cycles and failure generally occurred nearly simultaneously with damage initiation.

The second type of damage again only occurred in the  $[\pm 45/0]_s$  laminates. This damage mode is the same as that observed by Fanucci and Mar [31,36]. Delaminations formed along the edge of the hole at one or more locations and grew in a radial fashion away from the hole. This delamination growth was slow at first but as the size of the delamination increased, the

growth became more rapid. Seven of the  $[\pm 45/0]_s$  specimens showed this type of damage. Sectioning of the delaminated area and observation under a microscope at 50X magnification showed massive damage with delamination at all ply interfaces as well as transverse cracks throughout the thickness. However, these transverse cracks were not visible near the delamination front indicating that it is delamination which is the first damage which occurs and propagates.

The remaining  $[\pm 45/0]_s$  and all of the  $[\pm 45_2/0_2]_s$  and  $[\pm 45_3/0_3]_s$  specimens exhibited the third type of damage growth which extended along the longitudinal axis of the laminate parallel to the applied load. It is important to note that the width of this damage is the same as the diameter of the hole as the damage grew along two lines defined by the longitudinal lines tangent to the edges of the hole as illustrated in Figure 40. Microscopic inspection of sections of these specimens showed two symmetric delaminations at the  $-45^\circ/0^\circ$  interfaces. This delamination is centered in the laminate and is 6.35 mm in width as is the hole in the laminate. The delamination is bounded by two matrix splits located in the  $0^\circ$  plies at either end of the delamination.

The total length of the longitudinal delamination,  $2a$ , is characterized by the sum of the lengths of the two branches, one above the hole,  $a_t$ , and the other below the hole,  $a_b$ , as shown in Figure 40. This length was plotted versus the logarithm of the number of applied load cycles for all the specimens which exhibited this type of damage. It was observed in these cases

that this relation was nearly linear as illustrated in the typical experimental plot of Figure 42.

Daken and Mar [33,37] have shown that the growth of splits from a notch in unidirectional composites under tension-tension cyclic load can be correlated by an equation of the form:

$$2a = -A + \log(N) \quad (3.1)$$

where  $N$  is the number of applied load cycles,  $2a$  is the total delamination length, and  $A$  and  $B$  are constants to be determined. Daken and Mar originally used a natural logarithm correlation, but it seems more consistent to use a base 10 logarithm since it is more convenient to plot the data on a scale based on base 10 logarithms.

Linear regressions were performed on the longitudinal delamination growth data for each graphite/epoxy face sheet in order to determine the values of the parameters  $A$  and  $B$ . Two important parameters can be obtained once the constants  $A$  and  $B$  are determined. The cycles at which the damage initiates,  $N_0$ , can be determined from equation 3.1 by setting  $2a$  equal to zero and solving for the cycle  $N$ . In addition, the initial rate of damage propagagation can be determined by differentiating equation 3.1 and using the damage initiation cycle and thus obtaining the initial damage propagation rate. The average results for these calculations are listed in Table 18.

These results, as well as the representative data of Figure 42, show that the damage is controlled by the split growth in

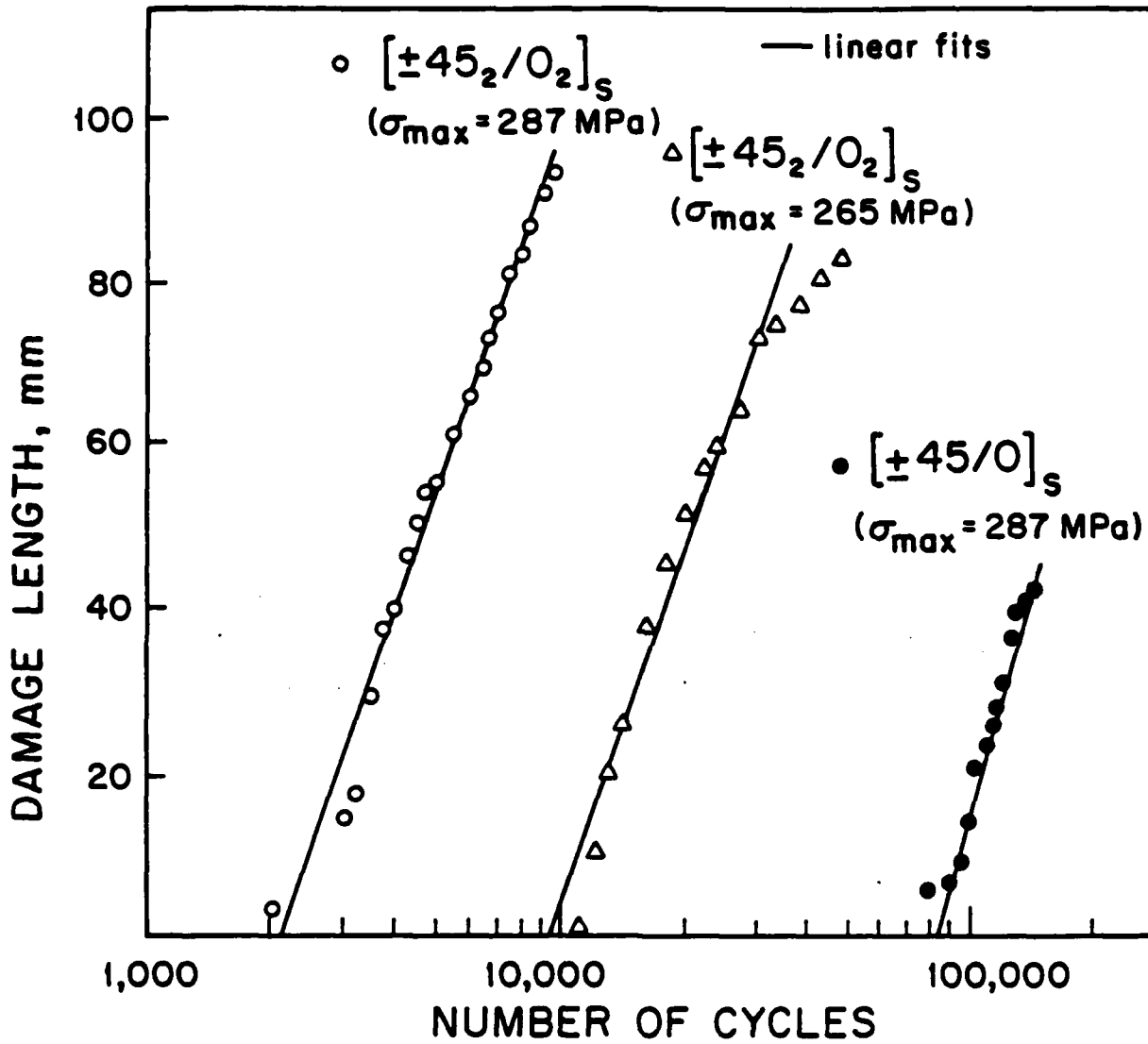


Figure 42

Typical plots of longitudinal delamination length versus logarithm of the number of applied load cycles.

Table 18 Average results of linear regressions for longitudinal delamination growth parameters for  $[\pm 45_n/0_n]_s$  graphite/epoxy specimens

LAMINATE	PEAK COMPRESSIVE STRESS, MPa	$N_0$ , CYCLES	C.V.	$(\frac{da}{dn})_0$ , MM/CYCLES
$[\pm 45/0]_s$	287	131,000	61%	$5.7 \times 10^{-4}$
$[\pm 45_2/0_2]_s$	287	2,900	49%	$1.0 \times 10^{-2}$
	265	5,300	51%	$7.1 \times 10^{-3}$
	243	19,500	76%	$1.8 \times 10^{-3}$
$[\pm 45_3/0_3]_s$	265	a		
	243	790	14%	$2.4 \times 10^{-2}$
	221	8,200	57%	$2.9 \times 10^{-3}$

<sup>a</sup> DAMAGE GREW FROM END TO END OF SPECIMEN BEFORE SECOND INSPECTION CYCLE

the  $0^\circ$  plies followed by delamination of the  $-45^\circ/0^\circ$  interface. The results also show that the initiation of this type of damage occurs considerably earlier for increased stress levels. The effective ply thickness has an even more dramatic effect on both the cycles to initiation and initial damage growth rate. A twofold increase in the effective ply thickness causes approximately a fortyfold decrease in the number of cycles to damage initiation. This twofold increase causes a twentyfold increase in the initial delamination growth rate.

A simple model can be devised to qualitatively explain this third damage type. Once the longitudinal splits develop, load is transferred from the area between the  $0^\circ$  plies into the neighboring  $-45^\circ$  plies by interlaminar shear stresses. The parts of the  $0^\circ$  plies which have delaminated can no longer carry any load and the delamination front grows. This model, shown in Figure 43, renders itself to a shear lag analysis to qualitatively determine the interlaminar shear stress in the matrix interlayer between plies,  $\sigma_{xz}$ . This was performed by Nolet [35] and shows that the interlaminar shear stress increases as the effective ply thickness increases. This supports the proposed model and the observed quicker propagation of delamination for the thicker specimens.

A simple experiment was run to support the proposed mechanism of longitudinal delamination growth after splitting occurs. A  $[\pm 45]_s$  laminate and a  $[\pm 45_2]_s$  laminate were cured along with two  $[0]$  and  $[0_2]$  laminates. Five 350 mm by 50 mm coupons were cut from each laminate and 6.35 mm holes drilled in

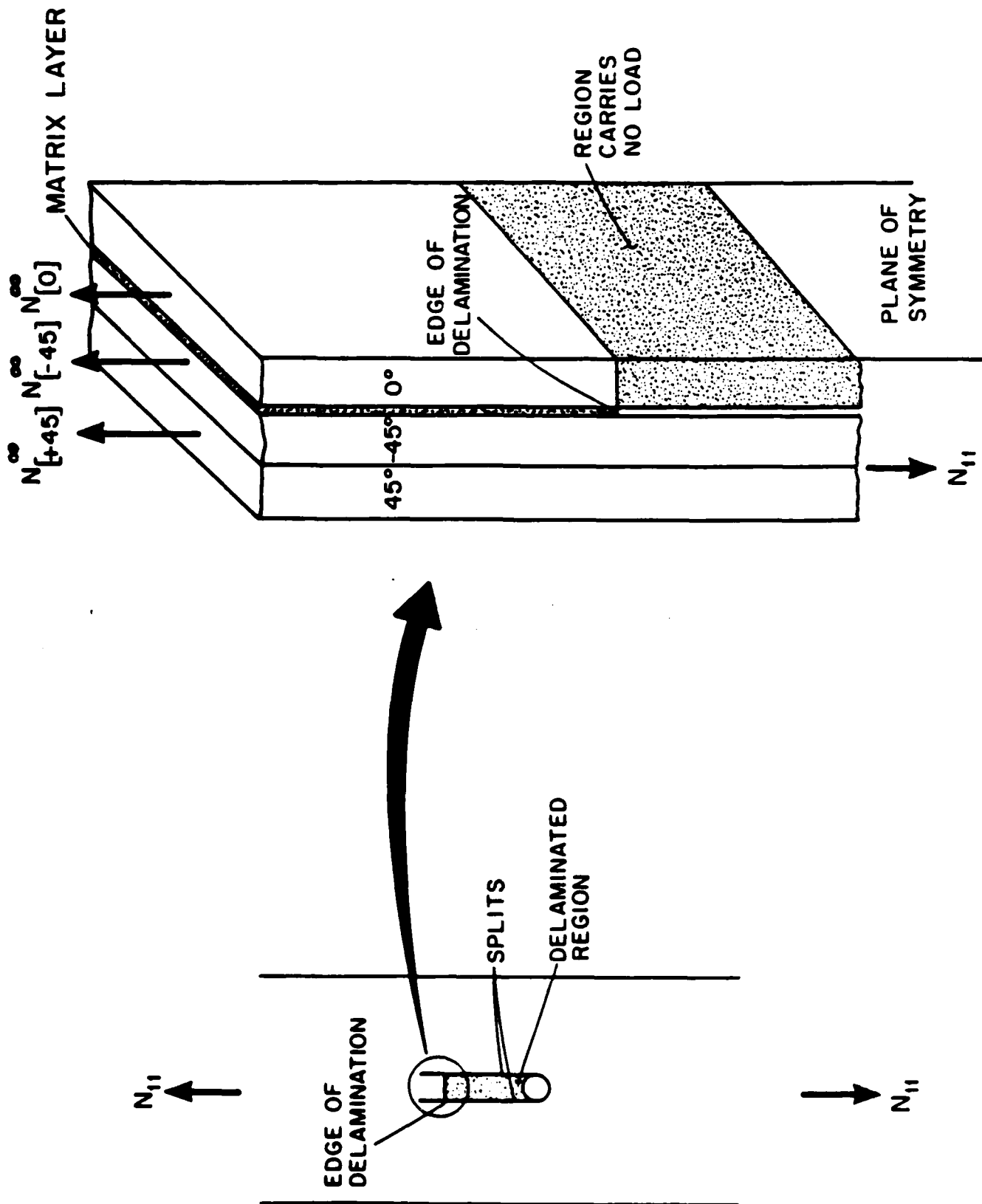


Figure 43

Schematic model of the progression of damage via longitudinal delamination.

the center of each coupon. A razor blade was used to cut two 50 mm long  $0^\circ$  splits at the hole edge in the cured unidirectional laminates. These unidirectional coupons were then bonded with a room-temperature cure epoxy to the  $\pm 45^\circ$  coupons resulting in specimens of  $[0_2//\pm 45]_s$  and  $[0//\pm 45]_s$  configurations where the double slash,  $//$ , represents the room temperature epoxy bondline. Loading tabs were bonded onto each end of the coupon resulting in the specimen depicted in Figure 44.

These specimens were tested in static tension with the tests halted at 900 Newton increments to allow for inspection of the coupon via the ultrasonic technique. Each specimen exhibited delamination growth at the  $0^\circ/45^\circ$  interface between the splits in the  $0^\circ$  plies. The delamination initiated at a significantly lower stress level of 88 MPa in the  $[0_2//\pm 45]_s$  coupons that the stress level of 132 MPa in the  $[0//\pm 45]_s$  coupons. Similarly constructed laminates without the premade splits were cycled in tension-tension. Splits originated at the edges of the hole and propagated longitudinally along with subsequent delamination.

The fact that the same damage occurs under tension indicates that it is not prompted by local buckling or peel stresses, but by shear stresses. The static tests also clearly demonstrate that longitudinal delamination occurs as a result of interlaminar shear failure of the ply interface between the  $0^\circ$  ply and the neighboring angled ply in the regions between splits in the  $0^\circ$  ply.

The shear lag analysis also shows that the relative elastic

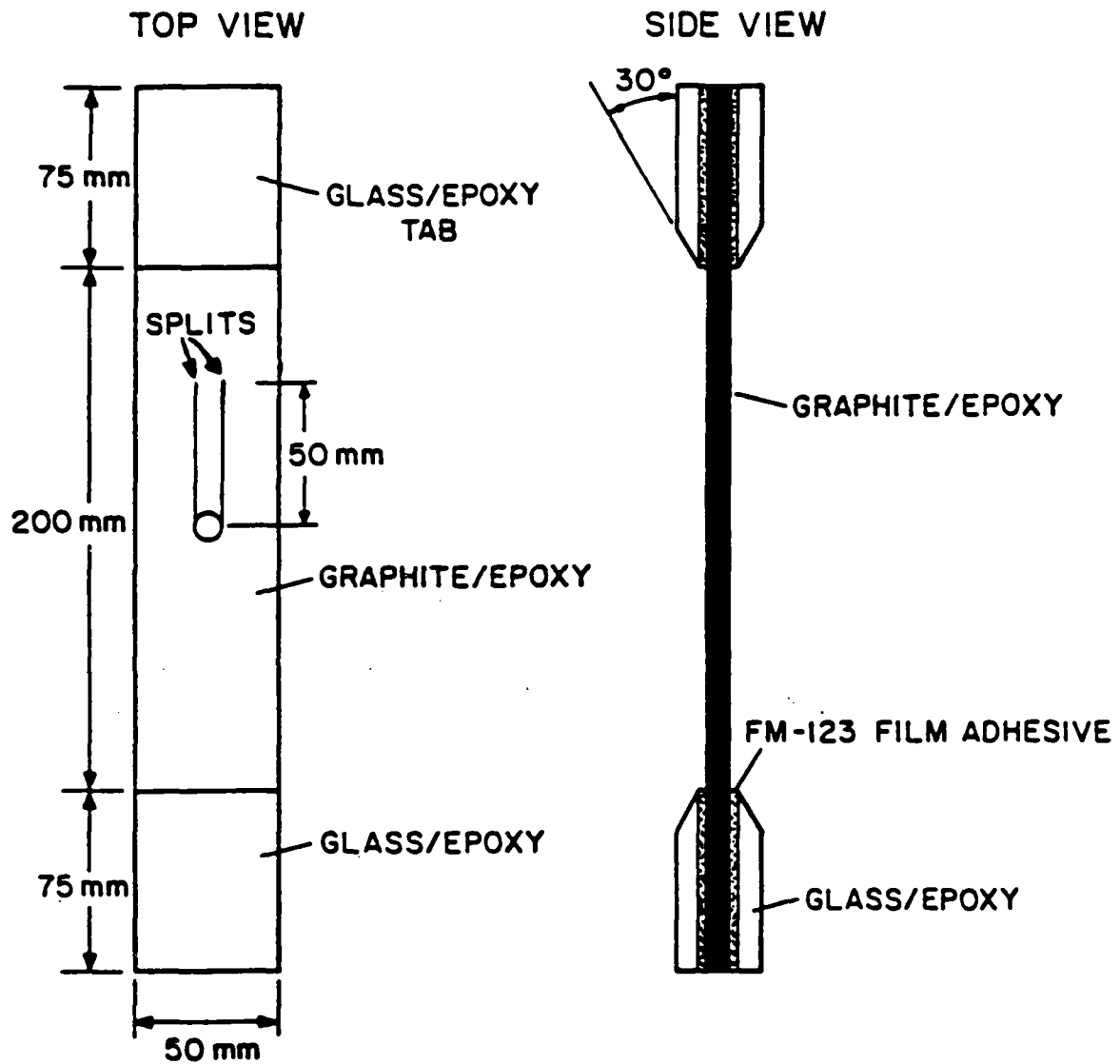


Figure 44 Physical characteristics of the special tensile coupon specimen with precut splits.

constants of the plies are important in determining the value of the shear stress at the ply interface. The elastic constraint of the neighboring plies is also important in determining when splitting will occur. Flaggs and Kural [20] have shown that the "in-situ" strength depends upon the thickness of the ply layer. The elastic constraint of the neighboring angled plies induces stresses in the  $0^\circ$  plies which may help to restrict splitting. As the  $0^\circ$  layer becomes thicker, this constraint effect becomes less important and thus splitting is more likely to occur at lower applied loads.

For the  $[\pm 45/0]_s$  laminates, the elastic constraint of the neighboring plies may be enough to prevent splitting from occurring in the  $0^\circ$  layer and thus the other type of delamination damage eventually occurs. However, once initiated, this type of damage propagates much faster. This type of damage promotes a peel stress due to localized buckling which has a Mode I type component. Wilkins et. al. [38] suggest that Mode I type damage propagation is much quicker than Mode II type damage propagation. This would explain why the splitting and delamination damage grows much more slowly than the radial type damage. The development of splitting alters the stress distribution at the edge of the hole which apparently prevents the peel stress induced delamination from occurring thus increasing the life of the specimen.

Residual strength tests were conducted on the graphite/epoxy face sheets of the sandwich specimens which survived the cyclic loading and were not sectioned for

microscopic inspection. The graphite/epoxy face sheets were debonded from the honeycomb at 150°C for ten minutes at which point the face sheets were easily peeled away from the honeycomb. These face sheets then had four glass/epoxy loading tabs bonded onto them resulting in the standard tensile specimen of Figure 4. A total of 46 of these specimens was tested monotonically to failure in tension using the same procedure outlined for the static compression tests. The results are summarized in Table 19. Six  $[\pm 45/0]_s$  coupon specimens were also manufactured and tested in static tension without being cycled to obtain the undamaged fracture stress of a coupon with a 6.35 mm diameter hole which is 417 MPa.

The results for the  $[\pm 45/0]_s$  laminates are delineated by the damage type found on that particular face sheet. The specimens with transverse or radial delamination show a slight increase in tensile fracture stress over the uncycled value. However, the specimens with longitudinal delamination have a considerable, on the order of 50%, increase in residual tensile strength. This trend holds true for the  $[\pm 45_2/0_2]_s$  and  $[\pm 45_3/0_3]_s$  specimens which all had longitudinal delamination. These results indicate that the longitudinal damage causes a stress redistribution around the hole such that the 0° plies no longer see the effect of the notch. The small strip of 0° ply between the splits which has delaminated also is no longer load-carrying. The residual strength is very near the unnotched strength of a  $[\pm 45/0]_s$  laminate in tension reported by Lagace [21]. Postmortem observation of the failed specimen shows that

Table 19 Average results of residual tensile strength tests for  $[\pm 45_n/0_n]_s$  graphite/epoxy specimens

LAMINATE	DAMAGE TYPE	NUMBER OF SPECIMENS	LONGITUDINAL MODULI		TENSILE STRENGTH	
			$E_L$ , GPa	C.V.	$\sigma_F$ , MPa	C.V.
$[\pm 45/0]_s$	NDD <sup>a</sup>	6	59.3	6.2%	543	3.1%
	RD <sup>b</sup>	4	60.6	5.2%	496	17%
	LD <sup>c</sup>	5	57.0	5.3%	643	8.3%
$[\pm 45_2/0_2]_s$	LD	21	54.9	10.3%	674	9.0%
$[\pm 45_3/0_3]_s$	LD	10	54.8	9.5%	605	9.8%

<sup>a</sup> NO DETECTED DAMAGE

<sup>b</sup> RAIDAL DELAMINATION

<sup>c</sup> LONGITUDINAL DELAMINATION

a strip of 0° ply above the laminate does not carry load as it remains intact after fracture while the remaining 0° fibers fractured across the width of the specimen.

By this longitudinal delamination, the laminate has become nearly notch-insensitive to longitudinal tensile load. It is important to point out, however, that other load types were not investigated and this damage may cause a degradation in residual strength for loadings such as shear, transverse compression and the like. Further experimentation is warranted.

Lagace and Nolet discuss these experiments, results, analyses, and conclusions in depth in References 35 and 39. The work has shown that splitting occurs in multidirectional laminates under cyclic load. This indicates that tension-tension loading will also create this damage in multidirectional laminates as has been observed in unidirectional laminates. A program to investigate this aspect is currently underway and is described in the next section.

### 3.2 Splitting Damage in Multidirectional Laminates under Tension-Tension Cyclic Loading

The work reported in the previous section showed the importance of splitting and subsequent delamination under cyclic loading. The work also showed that similar damage will develop under tension-tension cyclic load.

A program is being undertaken to look at these phenomenon under tension-tension cyclic load. The laminate chosen for

investigation is a  $[0/\pm 45]_s$  laminate. This is a stacking sequence variation on the laminate studied in the previous investigation (see section 3.1). By placing the  $0^\circ$  plies on the outside, the ability to detect and measure the splitting damage in the  $0^\circ$  plies will be enhanced.

The study will be both experimental and analytical. At the present time, the experimental portion is partially-defined while the analytical work is still under consideration. The experiments will use the standard TELAC tensile specimen of Figure 4 with several different hole diameters: 3.175 mm, 6.35 mm, 9.525 mm, and 12.7 mm. Cyclic tests will be conducted at various stress levels to look at the dependence of damage development on the notch size and the stress level.

As a prelude to the cyclic testing, static tests will be conducted on two laminates:  $[45_{24}]$  and  $[0/\pm 45]_s$  with the four various hole sizes. The latter laminate will be tested in order to develop the baseline fracture static tensile fracture stresses. There does exist data on the  $[0/\pm 45]_s$  laminate under these conditions [6,21], but this data is several years old and there is evidence that the properties of the AS1/3501-6 graphite/epoxy has "crept up" over that time period necessitating new tests to establish the baseline.

The tests on the  $[45_{24}]$  laminates are complete. These tests were conducted to obtain their fracture stress which would indicate the stress at which splitting would originate in the  $+45^\circ$  or  $-45^\circ$  plies of the  $[0/\pm 45]_s$  laminate. Unfortunately, the data from these tests has a very large amount of scatter as can

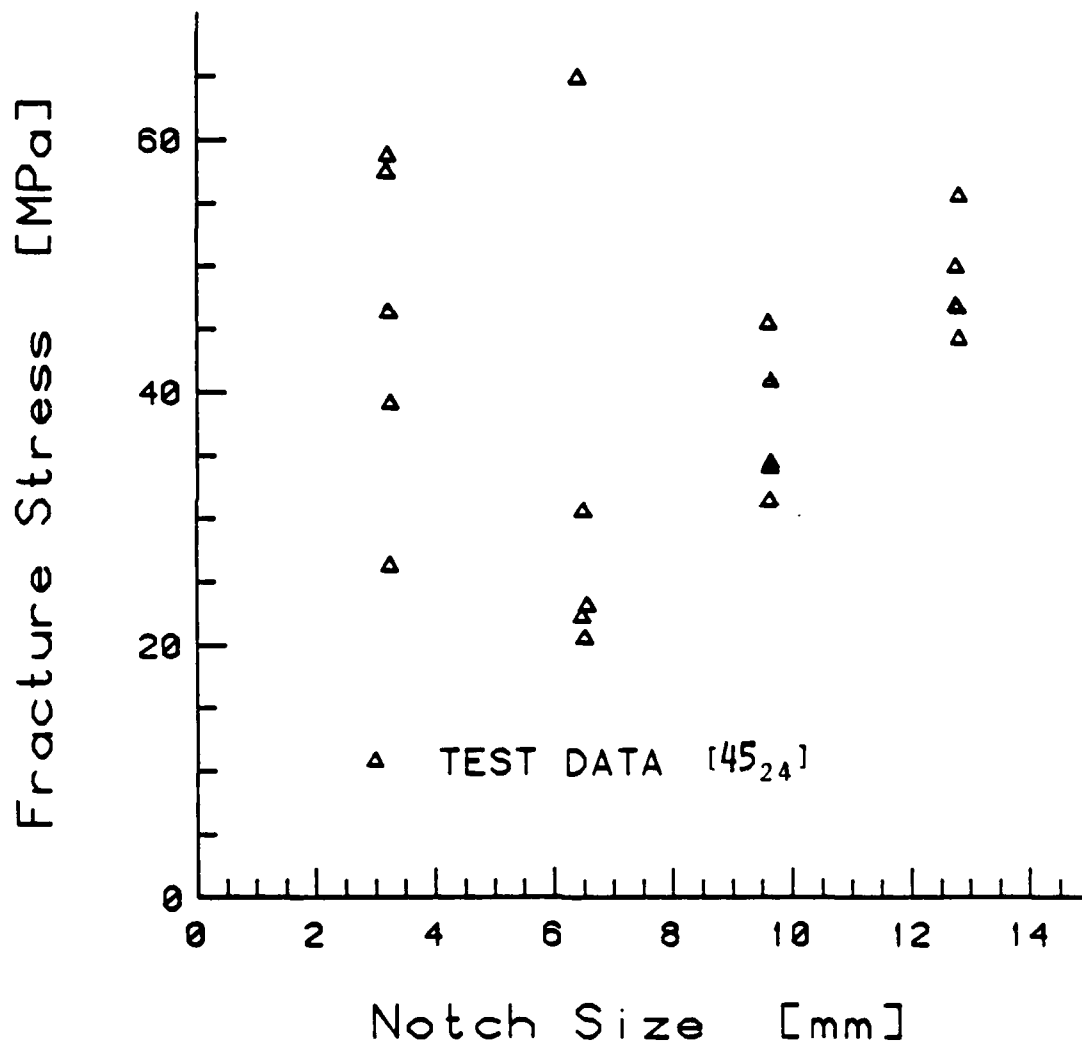


Figure 45 Experimental fracture stress versus notch size for the [45<sub>24</sub>] specimens with holes.

be seen in Figure 45, and does not yield any useful information. Previous work on a  $[45_8]$  laminate [6] had shown this scatter to exist, but it was attributed to the lack of sensitivity of the testing machine. Thus the thickness of the current specimen was tripled in order to increase the fracture loads. However, this was not successful in eliminating the scatter.

At the current time, the static tests on the  $[0/\pm 45]_s$  specimens are underway. Preliminary results do show increased properties, in the form of fracture stress, over the data reported by Lagace [6,21]. Manufacture of the specimens for the cyclic tests is nearing completion and testing should begin in the near future.

#### 4. DYNAMICS AND AEROELASTICITY

Research continued into the vibrations and aeroelasticity of composite wing structures, where advantage can be taken of the inherent mechanical coupling of an anisotropic layup to improve the vibration, flutter, and divergence properties of aircraft wings. The work during this period dealt mainly with determining the vibration and frequency characteristics of composite built-up wings.

##### 4.1 Vibrations and Deflections of Built-Up Graphite/Epoxy Wings

An experimental and analytical investigation was performed to look at the natural frequencies, vibration modes, and static deflections of symmetric but unbalanced built-up wings.

A five mode Rayleigh-Ritz formulation was used to derive the equations of motion, employing flexibility and mass matrices which included the effects of internal stiffeners, spar-web shear, and sectional wing box properties. The analysis followed that previously developed for solid laminate plate wings [40], and included the root warping restraint and chordwise flexibility.

Three sets of rectangular, cantilevered built-up wings were constructed and tested. The wings were 305 mm by 76 mm and were constructed with aluminum spars and ribs and, generally, graphite/epoxy cover sheets as illustrated in Figure 46. Two of

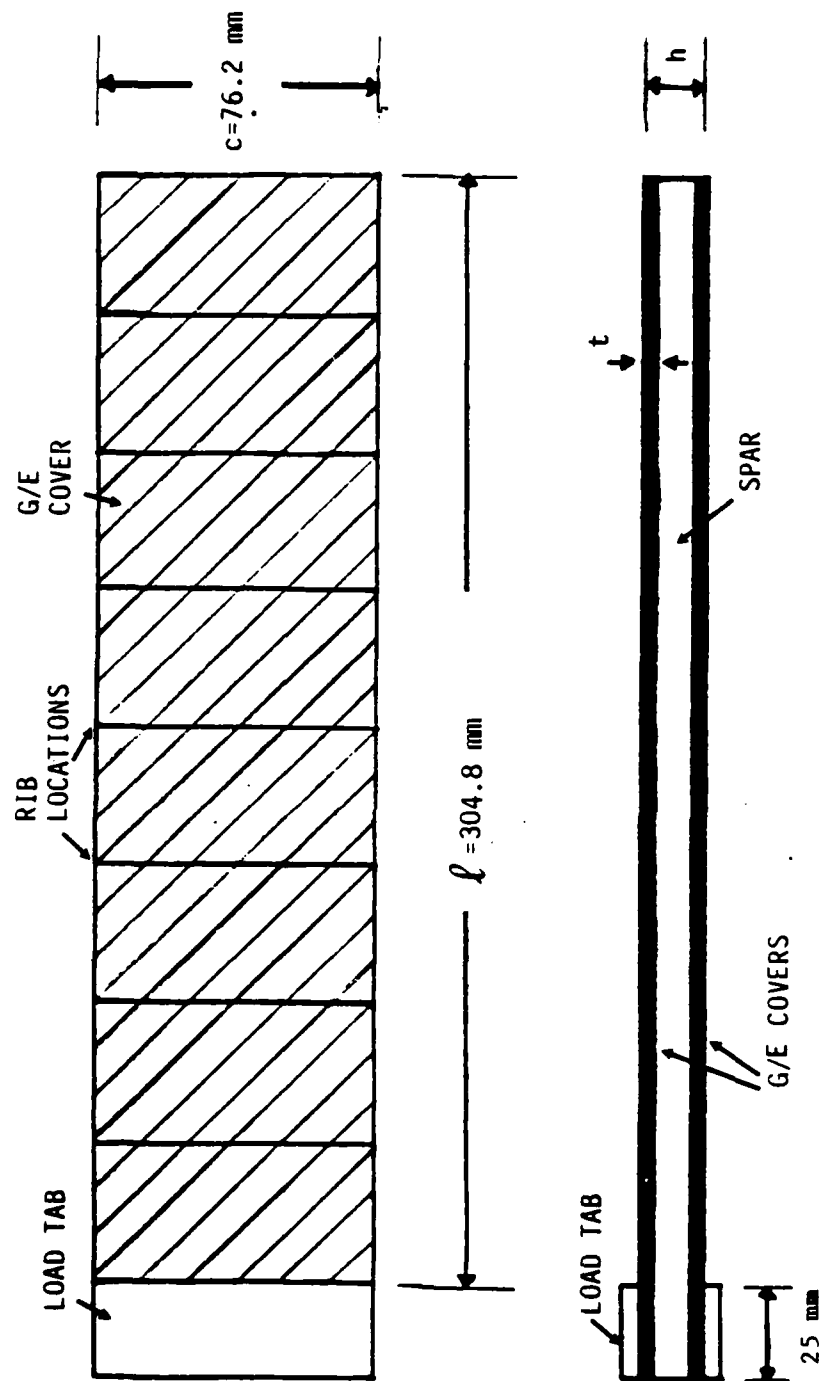


Figure 46 Characteristics of the wing box specimen.

the sets were composed of wings with cover sheets of  $[15_n]$ ,  $[30_n]$ , and  $[45_n]$  laminates. Of these two sets, one set had a 1.59 mm box depth and used two-ply laminates ( $n$  equal to 2), while the other set had a 3.18 mm box depth and used four-ply laminates ( $n$  equal to 4). All laminates were manufactured with AS1/3501-6 graphite/epoxy using the standard techniques described in section 2.1. The cured laminates were shaped to the required cover size. These wings, due to their off-axis construction, exhibit bending-torsion coupling.

The third set of built-up wings was composed of four different wings which did not exhibit bending-torsion coupling. The covers of these wings were either aluminum sheet (0.813 mm thick on a 3.18 mm deep box) or unidirectional graphite/epoxy. A  $[0_2]$  laminate was used as a cover for a box with a depth of 1.59 mm, while a  $[0_4]$  laminate was used for a 3.18 mm deep box. These wings served as a baseline reference.

All wings were constructed by bonding the 2024-T3 aluminum ribs and spars to the covers with EPOXY-PATCH room temperature curing epoxy. This was done so as to avoid thermal stresses and strains. A 25 mm long load tab was placed at the root of each wing in order to provide a good clamped boundary condition.

Vibration and static tests were conducted on all wings to determine their dynamic and displacement characteristics. The static tests were conducted in order to obtain the flexibility influence coefficients for wing tip response under pure force and pure moment. Loads were applied and deflections measured using the same basic setup as that used by Landsberger [41].

Typical results of static tests, showing force and moment versus centerline deflection at the tip and relative angle of twist, are shown in Figure 47 for the wings with  $[30_2]$  covers. The experimental data fell on the lines predicted by the Rayleigh-Ritz analysis.

The vibration tests were conducted by clamping each wing vertically in a vise. A small (6.35 mm square) piece of magnetic steel shim stock was affixed to each wing with double-stick tape and a miniature shaker consisting of a solenoid with a ferromagnetic core was used to provide excitation in the form of an oscillating magnetic field. This setup worked very well as a noncontact shaker. An accelerometer was mounted on the wing to obtain measurements.

The natural frequencies were determined using this setup. These are reported in Table 20 along with predicted frequencies from the Rayleigh-Ritz analysis. To obtain a visual picture of the corresponding mode shapes, the wing was cantilevered horizontally. At each natural frequency, small amounts of soap powder were sprinkled on the vibrating wing. The soap particles gravitated toward and came to rest on the node lines giving visual representation of these node lines as shown for the  $[30_4]$  cover wing in Figure 48. A compilation of node lines measured for the third mode of the  $[0_4]$  wings, determined in this manner, is shown in Figure 49.

Generally, the theoretical Rayleigh-Ritz analysis predicted the static flexibilities and three lowest natural frequencies of the low thickness-to-chord ratio wings reasonably well, except

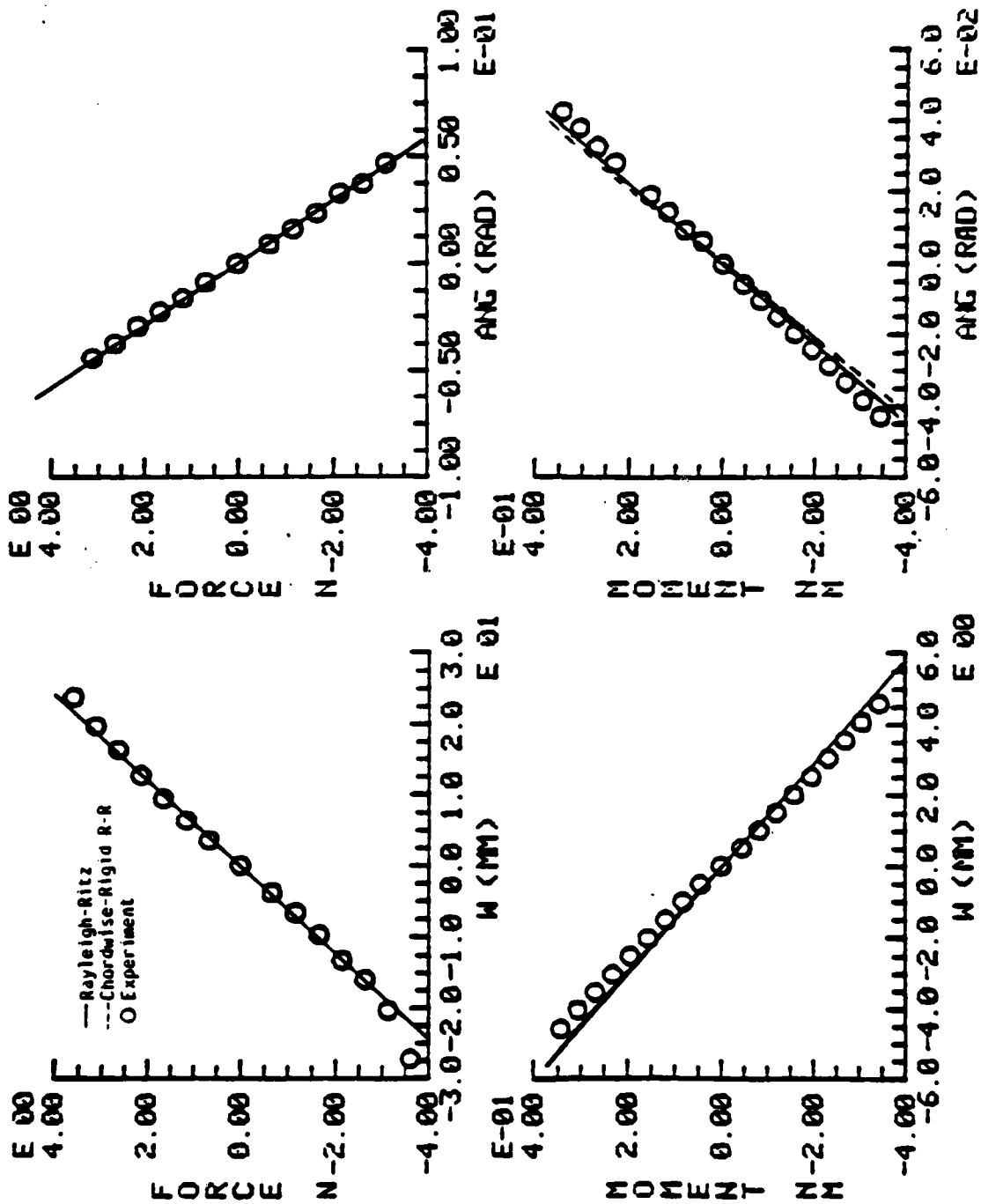


Figure 47 Typical results of static wing deflection tests (for [30<sub>2</sub>] wing).

Table 20      Experimental and analytical natural frequencies  
for the  $[\theta_2]$  and  $[\theta_4]$  wing sets

WING	$\omega_1$ (HZ)			$\omega_2$ (HZ)			$\omega_3$ (HZ)		
	EXP	RR	CR	EXP	RR	CR	EXP	RR	CR
$[0_2]$	28.9	28.9	29.0	106.7	99.9	99.9	163.2	181.3	181.5
$[15_2]$	23.1	22.6	22.6	114.4	114.4	115.3	146.1	150.3	151.0
$[30_2]$	16.5	16.6	16.7	103.1	109.8	109.8	149.2	144.2	156.7
$[45_2]$	13.4	13.0	13.1	84.8	86.7	87.0	133.1	135.0	164.7
$[0_4]$	62.1	62.2	62.2	206.2	207.2	207.2	315.1	388.8	389.7
$[15_4]$	50.6	50.2	50.3	229.0	250.7	253.1	310.9	334.9	336.6
$[30_4]$	36.7	35.3	35.6	208.8	235.7	235.7	312.9	311.7	342.7
$[45_4]$	28.6	27.1	27.3	171.3	182.6	183.3	278.5	289.6	361.7

EXP = Experiment

RR = 5-mode Rayleigh-Ritz analysis

CR = Chordwise-Rigid 4-mode RR analysis

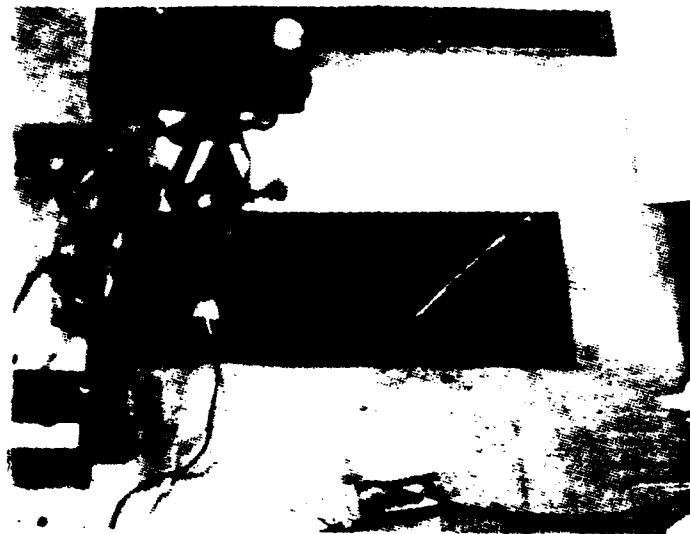


Figure 48

Photographs showing soap method to determine natural modes of graphite/epoxy built-up wings:  
(top)  $[30_4]$  wing in mode 2, 2nd bending;  
(bottom)  $[30_4]$  wing in mode 3, 1st torsion.

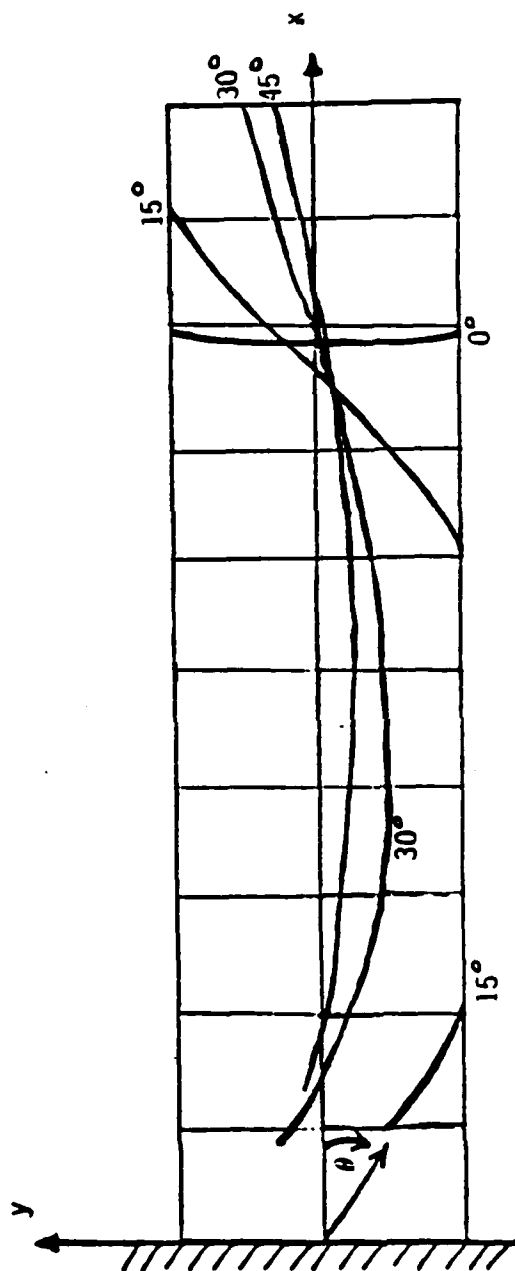


Figure 49 Experimentally-determined node lines for third mode of  $[\theta_4]$  wings. xx

that more modes were needed to converge the torsional flexibility. The analysis also showed the need to include chordwise bending, torsional warping restraint, internal stiffening, and spar shear for these built-up wings. The analyses seemed to support the use of a somewhat lower modulus of elasticity as obtained from plate flexural tests rather than the standard extensional modulus from tensile tests [42].

This investigation served to provide some theoretical and experimental results which illustrate clearly the behavior of built-up wing box beams with varying cover ply orientation and thus varying amounts of bending-torsion coupling. The work is more fully described by Gronet in Reference 43.

#### 4.2 Miscellaneous

In addition to the work mentioned here on vibration and frequency behavior of wings, some additional work was done reviewing previous results on the aeroelastic flutter and divergence of forward swept wings. These were written up and presented at the AIAA/ASME/ASCE/AHS 25th Structures, Structural Dynamics, and Materials Conference held in Palm Springs, California in May of 1984. See Reference 44.

# REFERENCES

1. Lagace, P.A., Mar, J.W., and Dugundji, J., "Fracture, Longevity (Fatigue), Dynamics, and Aeroelasticity of Composite Structures", Report for period January 1982 to December 1982 for Air Force Office of Scientific Research, AFOSR-84-0001TR, June, 1983.
2. ASTM Standard D 3039-76, Annual Book of ASTM Standards, Section 15, American Society for Testing and Materials, 1983, pp. 162-167.
3. Lagace, P.A., and Brewer, John C., TELAC Manufacturing Course Class Notes, Edition 0-2, TELAC Report 81-14, Massachusetts Institute of Technology, September, 1981.
4. Chisholm, J., and Chin, D., "Stress-Strain and Fracture Data for some Unnotched Graphite/Epoxy Laminates", TELAC Report 83-14, Massachusetts Institute of Technology, September, 1983.
5. Tsai, S.W., and Wu, E.M., "A Generalized Theory of Strength for Anisotropic Materials", Journal of Composite Materials, Vol. 5, 1971, pp. 58-80.
6. Lagace, P.A., "Static Tensile Fracture of Graphite/Epoxy", TELAC Report 82-4, Massachusetts Institute of Technology, April, 1982.
7. TEBAS Users' Guide, Edition 1, TELAC Report 84-14-1, April, 1984.
8. Lagace, P.A., "Nonlinear Stress-Strain Behavior of Graphite/Epoxy Laminates", Proceedings of the AIAA/ASME/ASCE/AHS 25th Structures, Structural Dynamics and Materials Conference, Palm Springs, California, May, 1984, pp. 63-73.
9. Chisholm, J., and Chin, D., "Effects of Loading into the Nonlinear Region of  $[0]_2$ ,  $[\pm 25]_s$ ,  $[\pm 40]_s$ ,  $[\pm 50]_s$ , and  $[\pm 55]_s$  Graphite/Epoxy Laminates", TELAC Report 83-15, Massachusetts Institute of Technology, September, 1983.
10. Lagace, P.A., "Delamination Fracture under Tensile Loading", Proceedings of the Sixth Conference on Fibrous Composites in Structural Design, AMMRC-MS-83-2, Army Materials and Mechanics Research Center, November, 1983, pp. IX 53-70.
11. Oplinger, D., Parker, B.S., Foley, G., and Jamoth, R., "Comparison of Tension Specimen Designs for Static and Fatigue Testing of Composite Materials", presented at the ASTM 2nd U.S.-Japan Symposium on Composite Materials,

Hampton, Va, June, 1983.

12. Brewer, J.C., and Weems, D.B. "Comparison of Tapered and Straight-Edged Graphite/Epoxy Coupons, II", TELAC Report 83-13, Massachusetts Institute of Technology, September, 1983.
13. Kassapoglou, C., "Interlaminar Stresses at Straight Free Edges of Composite Laminates", TELAC Report 84-18, Massachusetts Institute of Technology, October, 1984.
14. Brewer, J.C., "The Effect of Ply Thickness on Delamination of Advanced Composites", TELAC Report 84-20, Massachusetts Institute of Technology, July, 1984.
15. Mar, J.W., and Lin, K.Y., "Fracture of Boron/Aluminum Composites with Discontinuities", Journal of Composite Materials, Vol. 11, 1977, pp. 405-421.
16. Mar, J.W. and Lin, K.Y., "Fracture Mechanics Correlation for Tensile Failure of Filamentary Composites with Holes", Journal of Aircraft, Vol. 14, 1977, pp. 703-714.
17. Fenner, D.N., "Stress Singularities in Composite Materials with an Arbitrarily Oriented Crack Meeting an Interface", International Journal of Fracture, Vol. 12, 1975, pp. 705-721.
18. Nuismer, R.J., and Whitney, J.M., "Uniaxial Failure of Composite Laminates Containing Stress Concentrations", Fracture Mechanics of Composites, ASTM STP 593, American Society for Testing and Materials, 1975, pp. 117-142.
19. Whitney, J.M., and Nuismer, R.J., "Stress Fracture Criteria for Laminated Composites Containing Stress Concentrations", Journal of Composite Materials, Vol. 8, 1974, pp. 253-265.
20. Flaggs, D.L., and Kural, M.H., "Experimental Determination of the In-Situ Transverse Lamina Strength in Graphite/Epoxy Laminates", Journal of Composite Materials, Vol. 16, 1982, pp. 103-115.
21. Lagace, P.A., "Notch Sensitivity and Stacking Sequence of Laminated Composites", to appear in Composite Materials: Testing and Design (Seventh Conference), ASTM STP 893, American Society for Testing and Materials.
22. Archard, K., and Park, H., "Tensile Fracture of Laminates with Two Sets of Angled Plies", TELAC Report 83-20, Massachusetts Institute of Technology, December, 1983.
23. Chang, Y.P., and deLuis, J., "Determination of the Mechanical Properties of Graphite/Epoxy Prepreg Composite",

TELAC Report 82-6, Massachusetts Institute of Technology, May, 1982.

24. Chang, Y.P., Archard, K., and Brewer, J.C., "Tensile Properties of Unnotched and Notched Graphite/Epoxy Fabric Composites", TELAC Report 83-7, Massachusetts Institute of Technology, May, 1983.
25. Vizzini, A.J., "Instabilities and Failure of Graphite/Epoxy Tubes in Compression", TELAC Report 83-8, Massachusetts Institute of Technology, June, 1983.
26. Whitney, J.M., and Sun, C.T., "Buckling of Composite Cylindrical Characterization Specimens", Journal of Composite Materials, Vol. 9, April, 1975, pp. 138-148.
27. Khot, N.S., "Buckling and Postbuckling Behavior of Composite Cylindrical Shells under Axial Compression", AIAA Journal, Vol. 8, February, 1970, pp. 229-235.
28. Vizzini, A.J., and Lagace, P.A., "The Role of Ply Buckling in the Compressive Failure of Graphite/Epoxy Tubes", AIAA Paper No. 84-0963-CP, Proceedings of the AIAA/ASME/ASCE/AHS 25th Structures, Structural Dynamics and Materials Conference, Palm Springs, California, May, 1984, pp. 342-350.
29. Mar, J.W., "Fracture, Longevity, and Damage Tolerance of Graphite/Epoxy Filamentary Composite Materials", Journal of Aircraft, Vol. 21, January, 1984.
30. Graves, M.J., "The Effects of Compression-Compression Fatigue on Balanced Graphite/Epoxy Laminates with Holes", TELAC Report 79-1, Massachusetts Institute of Technology, February, 1979.
31. Fanucci, J.P., "Damage Initiation and Propagation during Compressive Fatigue of Flawed Graphite/Epoxy Composites", TELAC Report 81-10, Massachusetts Institute of Technology, June, 1981.
32. Kulkarni, S.V., McLaughlin, P.V., Jr., Pipes, R.B., and Rosen, B.W., "Fatigue of Notched Fiber Composite Laminates: Analytical and Experimental Evaluation", Composite Materials: Testing and Design (Fourth Conference), ASTM STP 617, American Society for Testing and Materials, 1977, pp. 70-92.
33. Daken, M.H.M.H., "Splitting Initiation and Propagation in Flawed Unidirectional Graphite/Epoxy Composites under Tension-Tension Cyclic Loading", TELAC Report 83-6, Massachusetts Institute of Technology, February, 1983.

34. Shuart, M.J., "An Evaluation of the Sandwich Beam Compression Test Method for Composites", Test Methods and Design Allowables for Fibrous Composites, ASTM STP 734, American Society for Testing and Materials, 1984, pp. 152-165.
35. Nolet, S.C., "The Effect of Ply Thickness on the Initiation and Growth of Delamination in Graphite/Epoxy Laminates with Holes under Compressive Cyclic Loading", TELAC Report 84-1, Massachusetts Institute of Technology, January, 1984.
36. Fanucci, J.P., and Mar, J.W., "Fatigue Damage Detection in Thin Composite Laminates Using Out-of-Plane Moire Interferometry", Journal of Composite Materials, Vol. 16, March, 1982, pp. 94-102.
37. Daken, H.H., and Mar, J.W., "Splitting Initiation and Propagation in Notched Unidirectional Graphite/Epoxy Composites Under Tension-Tension Cyclic Loading", Composite Structures, Vol. 4, 1985, pp. 111-133.
38. Wilkins, D.J., Eisenmann, J.R., Camin, R.A., Margolis, W.S., and Benson, R.A., "Characterizing Delamination Growth in Graphite/Epoxy", Damage in Composite Materials, ASTM STP 775, American Society for Testing and Materials, 1980, pp. 168-183.
39. Lagace, P.A., and Nolet, S.C., "The Effect of Ply Thickness on Longitudinal Splitting and Delamination in Graphite/Epoxy under Compressive Cyclic Load", to appear in Composite Materials: Fatigue and Fracture, ASTM STP 907, American Society for Testing and Materials.
40. Hollowell, S.J., and Dugundji, J., "Aeroelastic Flutter and Divergence of Stiffness Coupled Graphite/Epoxy Cantilevered Plates", Journal of Aircraft, Vol. 21, January, 1984, pp. 69-76.
41. Landsberger, B.J., "Aeroelastic Properties of Straight and Forward Swept Graphite/Epoxy Wings", TELAC Report 83-4, Massachusetts Institute of Technology, February, 1983.
42. Turner, M.D., "Comparison of Static and Dynamic Test Methods for Determining the Stiffness Properties of Graphite/Epoxy Laminates", TELAC Report 79-7, Massachusetts Institute of Technology, June, 1979.
43. Gronet, M.S., "Vibration and Deflections of Built-up Graphite/Epoxy Wings with Bending-Torsion Coupling", TELAC Report 83-17, Massachusetts Institute of Technology, October, 1983.
44. Landsberger, B.J., and Dugundji, J., "Aeroelastic Behavior

of Unswept and Forward Swept Cantilever Graphite/Epoxy Wings", AIAA Paper No. 84-0903, Proceedings of the AIAA/ASME/ASCE/AHS 25th Structures, Structural Dynamics, and Materials Conference, Part 2, Palm Springs, California, May, 1984, pp. 589-598.

APPENDIX ALIST OF REPORTS GENERATED UNDER CONTRACT

The following is a list of the reports which have been generated under this contract effort. Most of these were referenced in the main body of the report and are contained in the Reference section. However, they are again listed here for convenience:

- TELAC-83-7 Chang, Ya-Pei, Archard, Karen, and Brewer, John, "Tensile Properties of Unnotched and Notched Graphite/Epoxy Fabric Composites", May, 1983.
- TELAC-83-8 Vizzini, Anthony J., "Instabilities and Failure of Graphite/Epoxy Tubes in Compression", S.M. Thesis, June, 1983.
- TELAC-83-13 Brewer, John C., and Weems, Douglas B., "Comparison of Tapered and Straight-Edged Graphite/Epoxy Coupons, II", September, 1983.
- TELAC-83-14 Chisholm, John, and Chin, David, "Stress-Strain and Fracture Data for some Unnotched Graphite/Epoxy Laminates", September, 1983.
- TELAC-83-15 Chisholm, John, and Chin, David, "Effects of Loading into the Nonlinear Region of  $[0]_2$ ,  $[\pm 25]_s$ ,  $[\pm 40]_s$ ,  $[\pm 50]_s$ , and  $[\pm 55]_s$  Graphite/Epoxy Laminates", September, 1983.
- TLEAC-83-17 Gronet, Marc S., "Vibration and Deflections of Built-up Graphite/Epoxy Wings with Bending-Torsion Coupling", S.M. Thesis, October, 1983.
- TELAC-83-20 Archard, Karen, and Park HaeSim, "Tensile Fracture of Laminates with Two Sets of Angled Plies", December, 1983.
- TELAC-83-22 Mar, James W., "Fracture, Longevity, and Damage Tolerance of Graphite/Epoxy Filamentary Composite Materials", Proceedings of the AIAA/ASME/ASCE/AHS 24th Structures, Structural Dynamics and Materials Conference, Lake Tahoe, Nevada, May, 1984. (Also available in Journal of Aircraft, Vol. 21, January, 1984.)

- TELAC-84-1 Nolet, Stephen C., "The Effect of Ply Thickness on the Initiation and Growth of Delamination in Graphite/Epoxy Laminates with Holes under Compressive Cyclic Loading", S.M. Thesis, January, 1984.
- TELAC-84-6 Vizzini, Anthony J., and Lagace, Paul A., "The Role of Ply Buckling in the Compressive Failure of Graphite/Epoxy Tubes", Proceedings of the AIAA/ASME/ASCE/AHS 25th Structures, Structural Dynamics and Materials Conference, Palm Springs, California, May, 1984, pp. 342-350. (to appear in AIAA Journal.)
- TELAC-84-7 Lagace, Paul A., "Nonlinear Stress-Strain Behavior of Graphite/Epoxy Laminates", Proceedings of the AIAA/ASME/ASCE/AHS 25th Structures, Structural Dynamics and Materials Conference, Palm Springs, California, May, 1984, pp. 63-73. (to appear in AIAA Journal.)
- TELAC-84-8 Lansberger, Brian J., and Dugundji, John, "Aeroelastic Behavior of Straight and Forward Swept Graphite/Epoxy Wings", Proceedings of the AIAA/ASME/ASCE/AHS 25th Structures, Structural Dynamics and Materials Conference, Part II, Palm Springs, California, May, 1984, pp. 589-598. (to appear in AIAA Journal.)
- TELAC-84-9 Lagace, Paul A., "Notch Sensitivity and Stacking Sequence of Laminated Composites", to appear in Composite Materials: Testing and Design (Seventh Conference), ASTM STP 893, American Society for Testing and Materials.
- TELAC-84-19 Lagace, Paul A., and Nolet, Stephen C., "The Effect of Ply Thickness on Longitudinal Splitting and Delamination in Graphite/Epoxy under Compressive Cyclic Load", to appear in Composite Materials: Fatigue and Fracture, ASTM STP 907, American Society for Testing and Materials.
- TELAC-84-20 Brewer, John C., "The Effect of Ply Thickness on Delamination of Advanced Composites", July, 1984.
- TELAC-84-23 Daken, H.H., and Mar, J.W., "Splitting Initiation and Propagation in Notched Unidirectional Graphite/Epoxy Composites Under Tension-Tension Cyclic Loading", to appear in Composite Structures.

APPENDIX BPERSONNEL

The following personnel have been associated with the present program during the past year:

Staff

Prof. James W. Mar (Laboratory Head)  
Prof. John Dugundji  
Asst. Prof. Paul Lagace  
Prof. Theodore Pian  
Mr. Albert Supple

Graduate Students

John Brewer  
Hatem Daken (Egyptian government)  
Marc Gronet  
Captain Robert Hinger (USAF)  
Stephen Nolet  
Anthony Vizzini

Undergraduate Students  
(part time, varying lengths of time)

Seifu Alemayehu  
Karen Archard  
Keith Ashelin  
John Brewer  
Scott Causbie  
Ya-Pei Chang

David Chin  
John Chisholm  
Robert Dare  
Javier deLuis  
Kari Egerton

Rich Maurer  
HaeSim Park  
David Trop  
Doug Weems  
Chris Winters

END

12-86

DTIC